Princeton University
Universitat Politècnica de Catalunya

Degree in Mathematics - Degree in Engineering Physics

Bachelor's Degree Thesis

String method for the study of nucleation events in multicomponent liquid mixtures

Josep Bataller i Umbert

Supervisor (Princeton): Andrej Košmrlj

Supervisor (UPC): Marino Arroyo

June 2021

I would like to thank Andrej Košmrlj, Sheng Mao and Mikko Haataja for their support, interest and patience throughout all these months. They have always showed genuine interest in the project, and they have provided the necessary guidelines I needed in every moment. I would especially like to thank Andrej for giving me the opportunity to collaborate with him, despite the circumstances on which this project has been developed.

I would also like to thank Marino Arroyo for putting me in contact with Andrej and for his help during all the project.

Finally, I would like to thank the CFIS institution for giving me the opportunity to do this project, despite the complications derived from the covid-19 pandemic, and for all their support during these months.

Abstract

Nucleation is a very common process by which phase separation takes place in multicomponent liquid mixtures. Phase field models are usually applied to study phase separation, but they are insufficient to study nucleation events, since these transitions are thermally activated and require overcoming an energy barrier. To overcome this difficulty, we combined phase field models with the string method, a numerical scheme capable of finding transition pathways and critical states, to study nucleation in binary and ternary systems. Our model is able to capture homogeneous and heterogeneous nucleation both in binary and ternary systems. We validate our approach by comparing it with classical nucleation theory, valid in a sharp interface limit, and further examine and discuss the discrepancies between these two approaches. In the future this model can be applied to study more complex configurations, some of which are interesting from a biological point of view because they simulate protein separation in the intracellular fluid.

Resum

La nucleació és un procés molt comú pel qual la separació de fases es dóna en sistemes líquids multicomponents. Els models de camps de fase són habitualment emprats per estudiar la separació de fases, però són insuficients per estudiar els processos de nucleació, degut a què aquestes transicions són activades tèrmicament i requereixen superar una barrera d'energia. Per superar aquesta dificultat, hem combinat els models de camps de fase amb el "string method" (mètode de la corda), un esquema numèric capaç de trobar camins de transició i estats crítics, per estudiar la nucleació en sistemes binaris i ternaris. El nostre model és capaç de capturar la nucleació homogènia i heterogènia tant en sistemes binaris com ternaris. Validem la nostra aproximació comparant-la amb la teoria de nucleació clàssica, vàlida en el límit de interfases abruptes, i examinen i discutim les discrepàncies entre aquestes dues aproximacions. En el futur aquest model pot ser emprat per estudiar configuracions més complexes, algunes de les quals són interessants des d'un punt de vista de la biologia perquè simulen la separació de proteïnes en el fluid intracel·lular.

Resumen

La nucleación es un proceso muy común por el cual la separación de fases se da en sistemas líquidos multicomponentes. Los modelos de campos de fase son habitualmente empleados para estudiar la separación de fases, pero son insuficientes para estudiar los procesos de nucleación, debido a que estas transiciones son activadas térmicamente y requieren superar una barrera de energía. Para superar esta dificultad, hemos combinado los modelos de campos de fase con el "string method" (método de la cuerda), un esquema numérico capaz de hallar caminos de transición y estados críticos, para estudiar la nucleación en sistemas binarios y ternarios. Nuestro modelo es capaz de capturar la nucleación homogénea y heterogénea tanto en sistemas binarios como ternarios. Validamos nuestra aproximación comparándola con la teoría de nucleación clásica, válida en el límite de interfases abruptas, y examinamos y discutimos las discrepancias entre estas dos aproximaciones. En el futuro este modelo puede ser empleado para estudiar configuraciones más complejas, algunas de las cuales son interesantes desde un punto de vista de la biología porque simulan la separación de proteínas en el fluido intracelular.

Keywords
string method, phase field models, multicomponent liquid mixtures, classical nucleation theory, finite differences, IMEX methods

MSC2020: 65M06

Contents

1. Introduction

Multicomponent systems are a fundamental part of biology and industry. While systems with two and three components (binary and ternary mixtures) have been widely studied and are well-understood, there is a lot of exploration to be made for systems with more than three components. These systems are very common in biology. For example, the intracellular fluid, which is formed by many droplets containing proteins, constitutes a system with a high number of components where phase separation plays a key role [1–5]. Phase separation is a phenomenon that has been studied for a very long time, from the second half of the XIXth century, back in the days of J. W. Gibbs [6].

The number of coexisting phases for systems with N_c components was studied by Mao et. al. in the article in [7]. They developed a new model consisting on taking the convex hull of the free energy landscape and dividing the convex hull in several regions, each of which presents a different number of coexisting phases. This algorithm can be easily checked for binary and ternary systems, but it applies to systems with an arbitrary number of components. In particular, this method was used to determine the number of coexisting phases for systems with 4 and 5 components under different conditions.

Although this treatment can predict the number of coexisting phases, it cannot take into account the equilibrium microstructure of each of them. The topology of the coexisting phases can be determined from the surface energies using a graph algorithm developed by Mao et. al. in [8]. Another way to determine the morphology of the coexisting phases is via the phase filed methodology. The phase field method is an approach used to reproduce the evolution of material systems. It has been successfully used to reproduce many phenomena, such as solidification, spinodal decomposition and many others [9]. If combined with the treatment by Cahn and Hilliard to study conservative systems, this method can be used to study phase separation [10].

Material systems with several phases are idealized as containing bulk regions (phases) separated by sharp interfaces. From a mathematical point of view this is quite complex to model because of the abrupt change in concentration at sharp interfaces. In contrast, the phase field methodology considers diffuse interfaces, where order parameters vary smoothly from one phase to the other across interfaces. Interfaces can be considered arbitrarily small, and when the sharp interface limit applies (the width of the interface is small enough compared to the size of the bulk regions) interfaces can be approximated as being sharp.

When studying phase separation, the results obtained by phase field theory and the ones from the energy density convexification algorithm developed by Mao et. al. [7] present a very good agreement in most of the cases. However, for some specific conditions, phase field theory does not reproduce correctly the number of coexisting phases predicted by the convexification algorithm. In such cases phase separation does not take place via spinodal decomposition. Instead, nucleation is the process by which the final equilibrium configuration is achieved. The problem comes from the phase field theory, which, in the way it was implemented by Mao et. al. in [7], only reproduces spinodal decomposition. To reproduce nucleation events stochastic thermal effects should be taken into account into the phase field methodology. However, this approximation is insufficient to study nucleation because the dynamics of these methods proceeds by waiting very long periods of time until the system experiences a transition. Hence, these cases must be studied apart using some other techniques which can simulate this mechanism in a reasonable time.

From a numerical point of view, the problem of computing energy barriers and transition pathways can be very difficult, especially for high-dimensional systems. Many numerical schemes have been developed to do so [11], like the Nudge Elastic Band method (NEB) or the string method. In this thesis we try to apply the string method to reproduce nucleation in multicomponent systems. This algorithm has been proven to

be very useful when computing transition pathways and energy barriers for a variety of complex dynamical systems [12–14].

The goal of this thesis is to determine whether the string method can be applied to study nucleation events, and apply it to binary and ternary systems to compare the results to classical nucleation theory. To do so we apply the string method to study configurations where spinodal decomposition does not happen, and phase separation takes place via nucleation. Once we find the transition paths, we compute the energy barriers and some other relevant parameters and compare these results to classical nucleation theory. To compare numerical results to the classical ones, only binary and ternary mixtures are studied in the thesis. Homogeneous nucleation is the only possible type of nucleation in binary mixtures, apart from nucleation at mould walls. For homogeneous nucleation, we compute energy barriers and critical radii under several conditions and compare them to the values predicted by classical nucleation theory. For ternary mixtures heterogeneous nucleation at interfaces can also take place. Hence, we determine energy barriers both for homogeneous and heterogeneous nucleation and determine whether they relate as in classical nucleation theory.

1.1 Related work

Much research has been done related to nucleation and the string method. Our work is partially based on this research, although we take a deeper look at the comparison between the string method and classical nucleation theory, and we try to expand it to more complex systems.

In the first place, phase field methods and classical nucleation theory were compared by Wu et. al. in [15]. In this article, phase separation in binary mixtures was studied in many configurations, some of which considered nucleation of several droplets at a time. However, the string method was not applied in that case. Results were found to be consistent with classical nucleation theory in some circumstances (in particular close to the binodal line, but close to the spinodal line results did not agree with classical nucleation theory).

The string method has been used to study many phase transition events, including nucleation. It was used by Li et. al. in [16] to study nucleation in diblock copolymers, although they focused on computing nucleation rates, which is a more complicated problem than what we consider in this thesis. It was also used to study nucleation in binary mixtures by Philippe et. al. in [14], although they did not focus on the comparison with classical nucleation theory. Zhang used the string method in [13] to study the nucleation of one-dimensional stochastic Cahn-Hilliard dynamics, using a very similar formalism to the one we used in this thesis, although in our thesis we expanded it to ternary systems. Philippe also studied homogeneous nucleation in ternary mixtures in [17], although restricted to the one dimensional case. Backofen used the string method in [12] to study nucleation of crystals on rigid substrates, and Zhang used the string method in [11] to study nucleation of solids.

In most of the previous articles the string method was only applied to binary mixtures, but applying the string method to ternary mixtures has not been studied in detail. Moreover, much research has yet to be done in heterogeneous nucleation events, which are the leading process in many real situations where phase separation takes place via nucleation. In most of the articles, classical nucleation was compared to simulations only qualitatively. However, in this thesis, we perform a quantitative comparison between the string method and classical nucleation theory.

Finally, one of the challenges in this thesis consists of relating physical properties of the system, like interface energies, to parameters from our model. This issue has attracted considerable interest recently, and many investigations has been done in that line [18–20]. Davis found some interesting results in his

thesis [10], where he used the phase field model to study microstructural evolution in fuel cell technology. In this thesis, he was able to develop a methodology to determine the model parameters from some physical properties of the systems he was modelling. Part of his derivation, along with the numerical scheme proposed by Zhang et. al. in [11], serves as the basis for our model.

1.2 Structure of the thesis

To determine the validity of the string method for the study of nucleation events the thesis is divided in four sections. The general structure of the thesis is:

- First of all, we make a detailed explanation of the **string method** and its numerical implementation. A classical example is also provided to discuss the behaviour of this method.
- In the next section, **classical nucleation theory** concepts which are used in the rest of the thesis are explained. Some derivations are performed as well, related to the comparison between energy barriers in different configurations. In particular, a concept called **shape factor** is defined and computed in two different configurations: nucleation on a mould wall and nucleation at an interface. The main three concepts commented on in this section are **homogeneous nucleation, heterogeneous nucleation** and **spinodal decomposition**.
- Next, we proceed to study nucleation in **binary mixtures**. First of all, we make a detailed explanation of how phase field models work and how to implement the string method. We also comment which is the relation between model parameters and physical constants. We then proceed to apply this methodology to study homogeneous nucleation under several conditions. First of all, we study phase separation in one dimension, to study the general behaviour of the method, as well as possible problems which may arise in more dimensions. Secondly, nucleation in two dimensions is studied both for cartesian coordinates on a square domain and polar coordinates in a circular domain. There are two goals in this section. The first one is to determine whether reduced dynamics in the radial component are effective to determine relevant magnitudes in nucleation, which are **energy barriers** and **critical radii**. The second one is to determine the validity of the results from simulations in cartesian coordinates, since this is the case we consider for ternary mixtures. Finally, nucleation in three dimensions is studied and compared to classical nucleation theory.
- Finally, nucleation for **ternary mixtures** is studied. In the first place, the phase field method is adapted to systems with three components. Then, the method is applied to study phase separation in one dimension, to determine possible problems which may arise in two dimensions. Then a discussion on the **contact angles** at triple junctions is performed, and finally, heterogeneous nucleation is compared to homogeneous nucleation in several configurations, via some magnitudes like the shape factor.

All the programs in this thesis have been developed using the programming language Python, alongside some usual libraries (NumPy, SciPy and Matplotlib). All codes are available under reasonable request.

2. The string method

A very common problem in complex dynamical systems is computing transition pathways, transition rates and free energy barriers for rare events. Although these events take place very sporadically they are of crucial importance in most of these systems. These systems usually have very large time scales associated with these transitions, due to the fact that thermal fluctuations are very small compared to the energy barriers. Hence, the dynamics consist of waiting very long periods until a fluctuation is big enough to bring one state above these barriers, and then the system switches to another state abruptly. In practice, these transitions cannot be studied by waiting such long periods of time, and alternative methods must be developed to determine transition pathways.

From a numerical point of view, the problem of computing energy barriers and transition pathways can be very difficult, especially for high-dimensional systems. Several numerical schemes exist to study these transition pathways [11]. These methods can be classified as surface walking methods, which focus on finding the saddle point of the energy landscape along the transition pathway, and methods that focus on finding the whole minimum free energy path. In the first case we have the gentlest ascent method or the dimer method, among others [21–24]. In the second case, some numerical schemes are the Nudged Elastic Band Method (NEB) and the string method [25–27].

In this thesis, we will focus on one of these methods, the (zero-temperature) string method, which was first proposed by Weinan E, Weiqing Ren, and Eric Vanden-Eijnden [27]. This method consists of evolving a string following an algorithm that guarantees that it evolves to the most probable transition path, as well as maintaining a particular parametrization for the string.

This method has been proven to be very useful when studying transition pathways in many systems [12–14]. It can also be generalized to the finite temperature string method, which is useful to study conformational changes arising in activated processes. In this modified method the potential forces are replaced by some constrained thermodynamic averaged forces, although the numerical scheme is practically the same [28]. The aim of the thesis is to determine whether the zero-temperature string method can give us information about the energy barriers, critical nucleus size and shapes, etc. when studying nucleation events.

2.1 Numerical implementation

The string method allows us to compute the most probable transition pathway between two metastable states, which we will name A and B. An initial string is considered connecting two states A and B. A **string** is a chain of states, which are usually referred to as images, which follow a certain parametrization. The initial string is parametrized using some intrinsic parametrization, such as arc length or energy-weighted arc length. We will use parametrization by arc length in this explanation, as this is the one we have used in the rest of the thesis. The main advantage of the energy-weighted arc length parametrization over a simple arc length parametrization is the fact that the first one concentrates more images near the saddle point of the free energy landscape, which is usually the state we are more interested in in computing. This allows us to determine this state with higher precision. However, for our purposes, the simple arc length parametrization will be enough.

Consider now that our system is modelled by the following equation:

$$\gamma \dot{q} = -\nabla V(q) + \xi(t) \tag{1}$$

where γ is the friction coefficient, $\xi(t)$ is a white noise with zero mean, $\langle \xi_j(t)\xi_k(0)\rangle = 2\gamma k_B T \delta_{jk}\delta(t)$. γ is a factor related to the dynamics of the system, but it does not affect the transition pathway we want to compute. We assume that $V(q)$ has at least two local minima, which are the metastable states A and B mentioned before. It can be proven that this system will also have at least one saddle point. Our goal is to find the **Minimum Free Energy Pathway** (MFEP) connecting these two states. By definition, a MFEP is a smooth curve, $\varphi^*(q)$, connecting two metastable states. This curve satisfies the following condition:

$$(\nabla V(q))^{\perp}(\varphi^*) = 0 \tag{2}$$

In this equation, $(\nabla V(q))^{\perp}(\varphi^*)$ is the component of $\nabla V(q)$ orthogonal to $\varphi^*(q)$. That is, all along the string the tangent vector to the curve is parallel to $\nabla V(q)$ at each image. These pathways happen to be the most likely transition pathways connecting two metastable states, since the probability of deviating from them decreases exponentially. They are usually referred to as the most probable transition pathways connecting the two states for this reason.

One way to obtain the desired path is to evolve the string using the following scheme:

- First, the string is evolved using gradient descent dynamics. Hence, the string is evolved via the following equation: $\dot{\varphi} = -[\nabla V(q)]^{\perp}$. For convenience, we have normalized the time over gamma ($t \to t/\gamma$). Observe that, if φ is a MFEP, it is an equilibrium state of this ODE. Alternatively we can also evolve the string using $\dot{\varphi} = -[\nabla V(q)]$, since the reparametrization step already takes into consideration that the final string satisfies Eq. 2. This expression is even simpler than the first one, and more accurate from a numerical point of view [29].

- Secondly, we impose that the string is parametrized by arc length, something which is lost in the previous step. To do so, we reparametrize the string by linearly interpolating the images so that they are equally spaced along the string.

This method has some advantages to other similar methods. The first one is that we do not need to know a priori the metastable states at the ends of the string to which we want to converge, but instead they are computed on the fly. It is enough to initialize the ends of the string in the basin of attraction of each state (which is usually quite simple if we know roughly the state to which we want to converge). The first step guarantees that these images evolve to a metastable state of the system, and the reparametrization does not affect the ending images of the string. Another advantage is that we can easily change the number of images along the string, even in the middle of the process, by simply linearly interpolating the current string. Moreover, the number of images in the string does not affect the convergence of the method (the convergence of the method, and hence the possible values for the time step and mesh size, are determined by the ODE to be solved, but the number of images along the string is independent of the ODE solver). Finally, we can impose different parametrizations in the string method, something which other methods, like the NEB method, lack. Moreover, it is quite straightforward to impose parametrization by arc length, which is the most simple case, and in may cases it is sufficient.

Finally, some more modifications can be considered to make the method more efficient. One of them is that the string does not need to be reparametrized at each iteration. Instead, it can be reparametrized every n_s iteration. The main advantage is that the method becomes faster if a large value of n_s is considered, something we are concerned about. However, taking very large values of n_s may pose a problem in precision, so an intermediate value must be considered.

2.2 Example: The Mueller potential

To illustrate the method we consider an example in which we have a system under a Mueller potential. The Mueller potential is a two dimensional potential given by the following expression:

$$V(x,y) = \sum_{k=1}^{4} A_k e^{a_k(x-x_k^0)^2 + b_k(x-x_k^0)(y-y_k^0) + c_k(y-y_k^0)^2} \tag{3}$$

with:

$$\begin{aligned} A &= (-200, -100, -170, 15) & c &= (-10, -10, -6.5, 0.7) \\ a &= (-1, -1, -6.5, 0.7) & x0 &= (1, 0, -0.5, -1) \\ b &= (0, 0, 11, 0.6) & y0 &= (0, 0.5, 1.5, 1) \end{aligned}$$

This potential has three minima and two saddle points. Our goal is to find the minimum free energy path connecting two of these minima, as well as finding (at least) one of the saddle points. The Mueller potential is a classical example in literature to find transition paths in these kind of systems [30].

To find the MFEP, we consider the domain $[-1.5, 1.2]x[-0.2, 2]$ (all the minima and saddle points lie in this region). The time step of the method is usually determined by the ODE solver we use. In our case we use an explicit algorithm (forward Euler method), and the time step we take is $h = 10^{-4}$ (usually explicit methods are not good enough for stiff equations, in which case very small time steps have to be considered for the method to converge. As an alternative implicit or Runge-Kutta methods must be used and larger time steps can be taken).

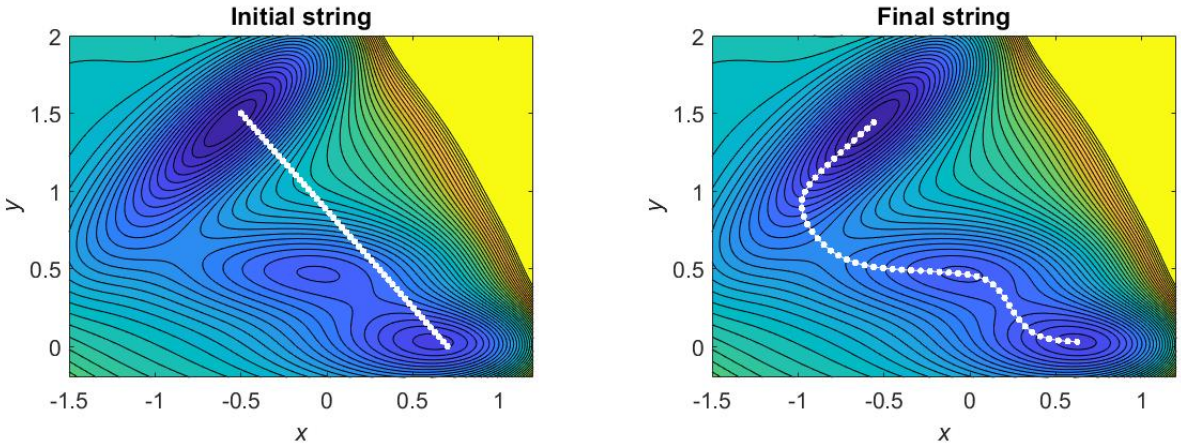

Figure 1: String evolution using the string method under the Mueller potential.

The fist step is to define the initial string. This step can be quite tricky for complicated systems, since the two ends have to be within the basin of attraction of the minima of the potential. If we plot graphically the contour plot of the potential we can qualitatively determine the two minima which we want to connect (see Fig. 1) and initialize the string so that the ending images are near the metastable states. In particular, we choose as our initial string a straight line connecting the states $A_0 = (-0.5, 1.5)$ and $B_0 = (0.7, 0)$, and we take $m = 50$ images along the string.

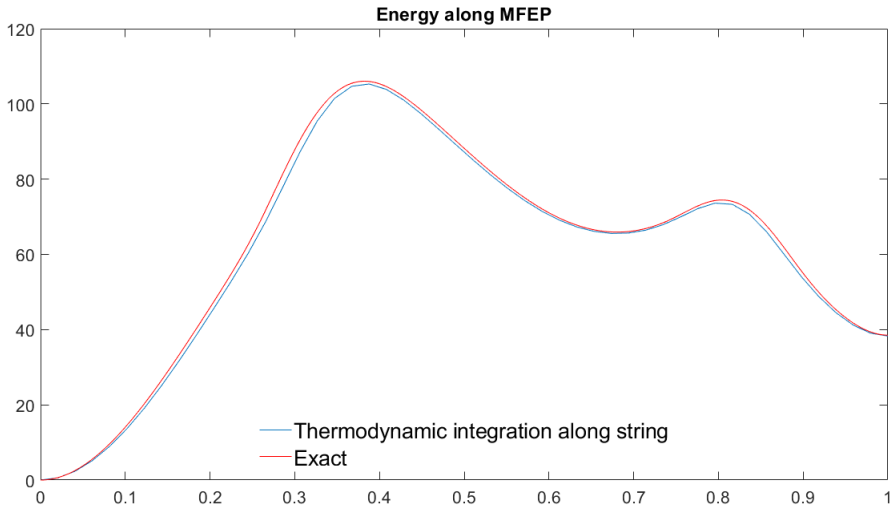

Figure 2: Comparison between exact energy along the string and energy computed by thermodynamic integration.

Secondly, we iterate the method. Since we can compute the gradient of the potential energy analytically and we use an explicit scheme the method is straightforward (otherwise some implicit equation would have to be solved an additional numerical errors would appear). We define the error as the ℓ_2 norm of the difference between consecutive iterations (divided by the number of images in the string for normalization), and consider a tolerance of $tol = 10^{-7}$. The method converges after 277 iterations to the final string plotted in Fig. 1,

To verify that we have converged to the MFEP connecting the two minima we can compute the potential energy along the string in two different ways.

The first one is simply computing the energy at each image of the string using the exact expression for the potential energy (Eq. 3), which gives us the exact value of the energy along the string. This system has no numerical error, since we have the analytical expression for the potential energy at each point.

The second way to compute the potential energy by thermodynamic integration along the string. It consists of integrating the component of ∇V tangent to the string at each image. This second expression should also give the value of the energy at each image because the string after convergence is a MFEP. Hence, the orthogonal component of ∇V along the string is 0, so all the contribution is in the tangent direction. This second way has some numerical error because the string is not exactly the MFEP, but instead it is an approximation. Moreover, since we are computing the integration numerically there is another source of error, coming from taking a finite number of images along the string. However, this second way should approximate the exact value of the energy along the string.

Both energy curves are plotted in Fig. 2. We can see that both curves are very close to each other. We can measure the relative error as the ℓ_2 norm of the difference between the integrated energy in the tangential direction and the exact one, divided by the ℓ_2 norm of the exact energy along the string. At the end of the method the error is $e = 0.019206$.

A more detailed analysis on the variations and improvements of this method is provided during the thesis. Some of them are changing the number of images on the fly and reparametrizing the string every certain number of iterations.

3. Classical nucleation theory

In material science, nucleation is a very common phenomenon which does not only take place in multicomponent liquid mixtures, but also metals and alloys. For instance, in these two last cases it is the responsible of solidification and melting. These phenomena take place between crystallographic and non-crystallographic states. These transformations are crucial in many applications in industry and engineering, and there are still many aspects which are not fully understood, due to the complexity of the process. It also takes place when a liquid is cooled bellow its melting point. One may expect that in this case the liquid starts to solidify spontaneously. However, a more detailed view into the process shows that this is not the case. From a thermodynamical point of view, the solid phase starts to form in small droplets, and these droplets begin to grow until they occupy all the volume, giving rise to the solid phase. These droplets (which are usually called nuclei) are unstable until they reach a certain critical nucleus size. They can form inside the liquid phase, a process called **homogeneous nucleation**, or in the interfaces or near the walls or impurities of the material, a process called **heterogeneous nucleation**. All along the thesis we will refer to droplets and nuclei indistinctly, since they refer to the same concept.

In this chapter, we discuss both types of nucleation from a thermodynamical point of view. This treatment is usually referred to as Classical Nucleation Theory (CNT) [31], and we will refer to it all along the thesis, since our goal is to compare the results from the string method with the expressions given by CNT. Moreover, a third process by which phase separation can take place is briefly commented, which is **spinodal decomposition**.

3.1 Homogeneous nucleation

When a liquid is cooled bellow its melting point, T_M, a driving force for solidification appears, $\Delta G = G_L - G_S$. This is caused by a balance between enthalpy and entropy of each phase, such that bellow the melting point the solid phase has a lower free energy and hence it is the most stable phase. However, the solid phase does not form homogeneously all over the liquid phase immediately. Instead, small droplets of solid particles start to form inside the liquid phase, and then they grow until they occupy the whole volume of the material system.

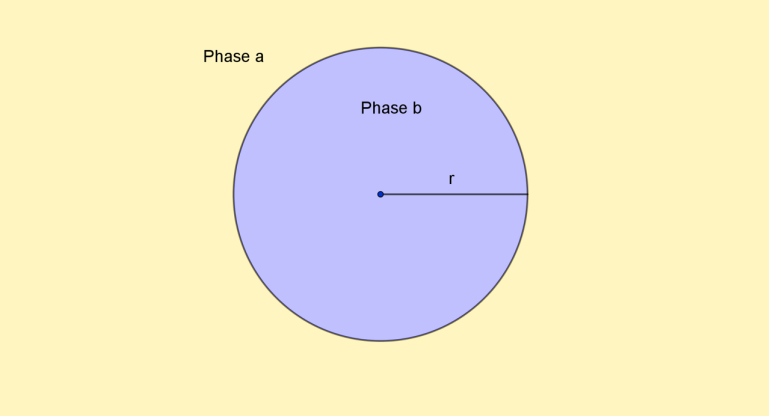

Figure 3: Homogeneous nucleation of a spherical droplet of radius r.

Let's consider a region in space which contains a liquid with volume V, and free energy G_1. If this liquid

is at temperature ΔT bellow T_M, some particles may cluster together to form a small sphere of solid, which we call a **nucleus**. In this case the free energy of the system will be:

$$G_2 = V_S G_V^S + V_L G_V^L + A_{SL}\gamma_{SL} \tag{4}$$

where V_S is the volume of the solid sphere, V_L the volume of the liquid, A_{SL} is the solid/liquid interface area, G_S and G_L are the free energies per unit volume of solid and liquid, respectively, and γ_{SL} is the solid/liquid interface free energy. The free energy at the initial state is $G_1 = (V_S + V_L)G_V^L$. The difference in free energy is then:

$$\Delta G_{hom} = G_2 - G_1 = -V_S \Delta G_V + A_{SL}\gamma_{SL} \tag{5}$$

where $\Delta G_V = G_V^S - G_V^L$. That is, there is a negative term because the solid phase has a lower free energy than the liquid phase, but there is also a positive term due to the creation of an interface between both phases. It can be shown that, for a given volume, the shape which minimizes the surface, and hence the interface free energy, is a sphere. Hence, if we assume that the nucleus has spherical shape with radius r, then the previous expression can also be written as:

$$\Delta G_{hom} = -\frac{4}{3}\pi r^3 \Delta G_V + 4\pi r^2 \gamma_{SL} \tag{6}$$

From the previous expression one can deduce that ΔG_{hom} is negative for large values of r and positive for r close to zero. More precisely, the previous expression has a minimum at $r = 0$ and a maximum, which is the critical radius that we are looking for, at:

$$r^* = \frac{2\gamma_{SL}}{\Delta G_V} \tag{7}$$

$$\Delta G^*_{hom} = \Delta G_{hom}(r^*) = \frac{16\pi(\gamma_{SL})^3}{3(\Delta G_V)^2} \tag{8}$$

This maximum acts as an energy barrier which does not allow the nucleus to grow. When the nucleus forms it has to grow up to a size which is greater than r^*, otherwise thermodynamical forces coming from the derivatives of the free energy will make it dilute again inside the liquid phase. The previous relations (Eqs. 6, 7 and 8) will be used to compare heterogeneous nucleation to homogeneous nucleation.

If we also use the expression $\Delta G_V = L_V \frac{\Delta T}{T_M}$, where L_V is the latent heat of fusion per unit volume, and $\Delta T = T_M - T$ is the difference between the temperature of the droplet and the melting temperature, then we can rewrite the previous expressions as: $r^* = \frac{2\gamma_{SL} T_M}{L_V}\frac{1}{\Delta T}$ and $\Delta G^*_{hom} = \frac{16\pi(\gamma_{SL})^3 T_M^2}{3(L_V)^2}\frac{1}{(\Delta T)^2}$. Hence, if we increase the undercooling, the energy barrier decreases and it shifts to smaller r values. That is, if we decrease the temperature far bellow the melting temperature this phenomenon of growing nuclei will not be noticeable, since almost all nuclei will end up reaching the critical radius value and growing until they occupy the whole volume. This is the reason why, if we decrease the temperature far bellow the melting temperature, the liquid will solidify spontaneously, so that we can only have a liquid bellow its melting temperature for relatively small undercoolings. This maximum variations can vary depending on the material, and in some cases we can have very large deviations (for example, under suitable conditions, liquid nickel can be undercooled 250K bellow its melting temperature, which is 1728K, without solidifying). In practice, however, we would never be able to undercool a liquid that far beyond the melting temperature because heterogeneous nucleation would take place.

The same results can be derived in two dimensions following the same procedure. In that case the increase in free energy is given by:

$$\Delta G_{hom} = -4\pi r^2 \Delta G_V + 2\pi r \gamma_{SL} \tag{9}$$

The values for the critical nucleus and the energy barrier, which are the values which maximize the previous expression, are:

$$r^* = \frac{\gamma_{SL}}{2\Delta G_V} \tag{10}$$

$$\Delta G^*_{hom} = \frac{\pi \gamma^2_{SL}}{2\Delta G_V} \tag{11}$$

3.2 Heterogeneous nucleation

Heterogeneous nucleation is a very common phenomenon and it is usually the one responsible for liquids to solidify because it takes place at smaller undercoolings than homogeneous nucleation. Unlike homogeneous nucleation, heterogeneous nucleation only takes place at crevices in mould walls, near impurities in the material or at interfaces between two phases.

From the expressions for the critical radius and energy barrier in homogeneous nucleation we can deduce that one way to reduce these values for small undercoolings (ΔT) would be reducing the value of the interface energy, γ_{SL}. This can be achieved if the embryo forms in contact with a mould wall or at an interface.

The derivation of the increase in free energy can be reproduced both in two dimensions and in three dimensions. In our simulations we will study nucleation in two dimensional domains, so we are mostly interested in computing this quantity in these configurations. However, the results in all cases are provided.

It can be checked that, both for nuclei forming in contact with a mould wall and at interfaces, the increase in free energy has the same expression as the homogeneous case (Eqs. 6 and 9) multiplied by a factor which only depends on the contact angles at triple junctions. This factor is called the **shape factor**, and it measures the quantity by which heterogeneous nucleation is more favorable than homogeneous nucleation. The complete derivation of the expressions of the shape factors can be found in appendix A.

We call $\Delta G^{2d}_{hom}(r)$ the expression for the increase in free energy in two dimensions for a droplet of radius r (see Eq. 9). Then, the increase in free energy in two dimensions is given, for nucleation at a mould wall (see Fig. 4) by:

$$\Delta G^{2d}_{het}(r, \theta) = \Delta G^{2d}_{hom}(r) S_1(\theta) \tag{12}$$

$$S_1(\theta) = \frac{\theta - \sin\theta\cos\theta}{\pi} \tag{13}$$

For nucleation at an interface the forming droplet consists on two circular caps, with radii r_1 and r_2 and contact angles θ and ϕ (see Fig. 4 for the definition of the parameters). The expression for the shape factor is:

$$\Delta G^{2d}_{het}(r_1, \theta, \phi) = \Delta G^{2d}_{hom}(r_1) S_2(\theta, \phi) \tag{14}$$

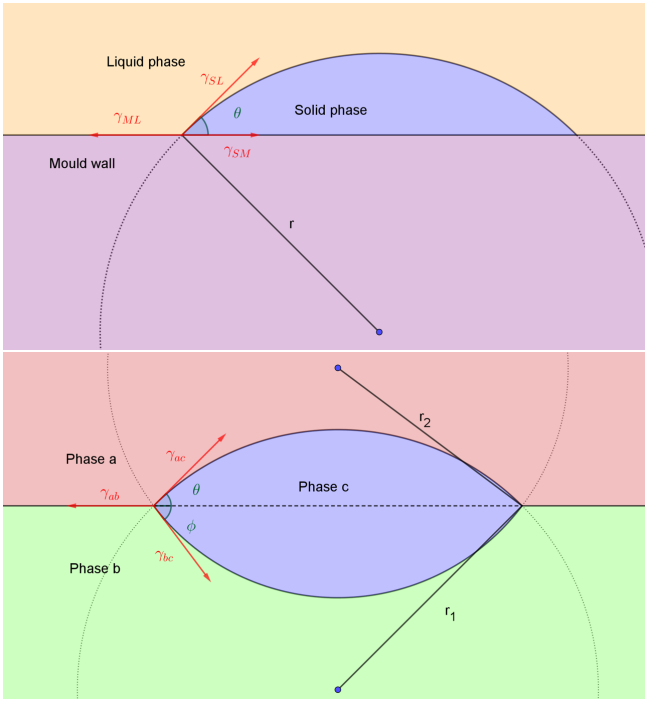

Figure 4: Heterogeneous nucleation in two different configurations. Upper figure: droplet in contact with a mould wall. Lower figure: droplet forming at an interface between two phases.

$$S_2(\theta,\phi) = \frac{\theta + \phi\frac{\sin^2\theta}{\sin^2\phi} - \frac{\sin\theta}{\sin\phi}\sin(\theta+\phi)}{\pi} \tag{15}$$

In three dimensions we have very similar expressions, but the relation for the shape factors change. The two configurations are the same as in two dimensions, and we can use the same notation (see Fig. 4 thinking of spherical caps on planar interfaces. If we call $\Delta G^{3d}_{hom}(r)$ the expression for the increase in free energy in three dimensions for a droplet of radius r (see Eq. 6), for nucleation at a mould wall we have the following expressions:

$$\Delta G^{3d}_{het}(r,\theta) = \Delta G^{3d}_{hom}(r) S_1(\theta) \tag{16}$$

$$S_1(\theta) = \frac{(2+cos\theta)(1-cos\theta)^2}{4} \tag{17}$$

For nucleation at an interface we have:

$$\Delta G^{3d}_{het}(r_1,\theta,\phi) = \Delta G^{3d}_{hom}(r_1) S_2(\theta,\phi) \tag{18}$$

$$S_2(\theta,\phi) = \frac{(2+\cos\theta)(1-\cos\theta)^2}{4} + \frac{(2+\cos\phi)(1-\cos\phi)\sin^3\theta}{4(1+\cos\phi)\sin\phi} \tag{19}$$

Observe that, with these expressions, we can also express the value of the critical radius and the energy barrier in terms of the corresponding values in homogeneous nucleation. If we name $S(\theta,\phi)$ the shape factor

in each case (that is, $S(\theta,\phi) = S_1(\theta)$ for nucleation at a mould wall and $S(\theta,\phi) = S_2(\theta,\phi)$ for nucleation at an interface), these relations are:

$$r^*_{het} = r^*_{hom} \tag{20}$$

$$\Delta G^*_{het} = \Delta G^*_{hom} S(\theta,\phi) \tag{21}$$

The factor $S(\theta,\phi)$ is always smaller than one, so the energy barrier for heterogeneous nucleation is always smaller than for homogeneous nucleation. For instance, if we look at $S_1(\theta)$ for the two dimensional case (see Fig. 5), for a value of the contact angle of $\theta = 10°$, $S_1(\theta) \approx 10^{-4}$, so that the barrier to heterogeneous nucleation is ten thousand times smaller than in the homogeneous case. This is the reason why, in practice, heterogeneous nucleation is the leading process for solidification to start, and homogeneous nucleation is usually not present. Significantly small values of $S_1(\theta)$ are obtained for several angles, including $\theta = 30°$ ($S_1(\theta) = 0.02$), and even for $\theta = 90°$ we get $S_1(\theta) = 0.5$.

It is interesting to notice that we can also recover the mould wall case from nucleation at interfaces if we consider ϕ close to 0 (this model fails to reproduce the values $\theta = 0$ and $\phi = 0$, but we can consider one of them to be very small). In that case, if the expression of $S_2(\theta,\phi)$ is rewritten in the limit $\phi = 0$, we get: $S_2(\theta,\phi) \to S_1(\theta)$, both in two dimensions and in three dimensions. When one of the angles is 0° (corresponding to the total wetting case), the nucleus should be modeled in a different way.

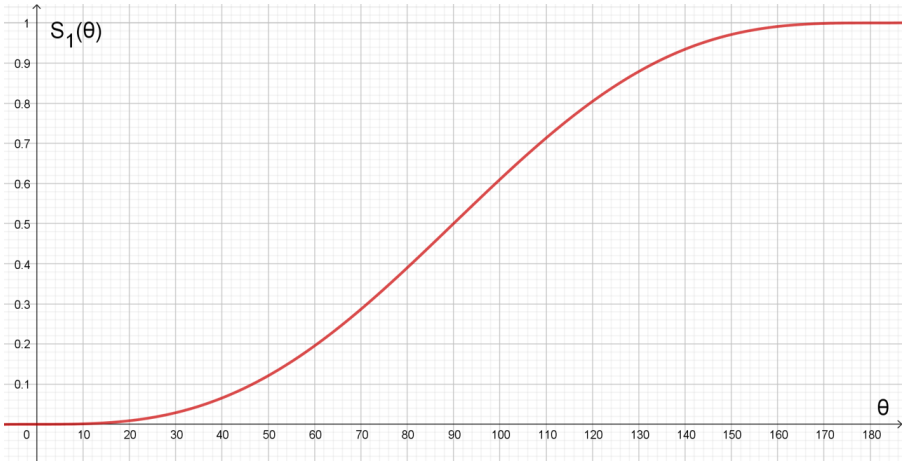

Figure 5: $S_1(\theta)$ in the two dimensional case, θ in degrees.

In this thesis, we will study homogeneous nucleation and heterogeneous nucleation at interfaces, but we will not consider nucleation on mould walls. However, we have seen that nucleation on the mould wall case is recovered from nucleation at interfaces in the limit where one of the interface energies is very small.

3.3 Spinodal decomposition

There are some phase transformations which do not present energy barriers to nucleation, and therefore they are spontaneous processes. One of them is spinodal decomposition [31].

Consider the phase diagram of an alloy which has a miscibility gap (see Fig. 6). The alloy, which initially is at temperature T_1 and has a volume fraction X_0 (state α in Fig. 6, outside the miscibility gap),

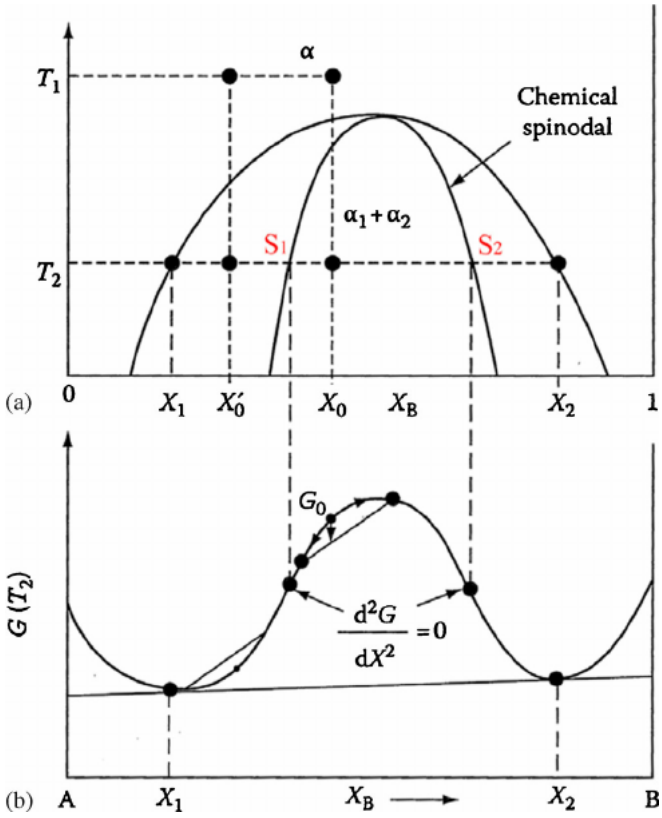

Figure 6: Upper figure: phase diagram of an alloy which presents a miscibility gap. Lower figure: free energy density of the same alloy at temperature T_2. Image taken from [31] (page 309).

is quenched to a temperature T_2, so that it enters the miscibility gap. At this temperature the alloy has a free energy G_0. However, since the free energy curve at that point has negative curvature, this new state is unstable because small fluctuations in composition produce a decrease in the free energy. The alloy splits into two distinct phases which end up having specific concentrations which minimize the free energy of the system. We say that the alloy experiences spinodal decomposition. In particular, this happens whenever the free energy curve (or surface if we have a compound with more than two phases) has negative curvature.

At temperature T_2, the alloy lies between the two points in the free energy curve S_1 and S_2, which correspond to the values of the concentration for which the curvature of the free energy is 0. The locus of these two points is known as the chemical spinodal, or to abbreviate the **spinodal**, if there is no confusion. Outside the chemical spinodal small fluctuations in concentration lead to an increase in the free energy, so the states there are metastable. The only way to decrease the free energy in these cases is by a process of nucleation and growth, which has associated an energy barrier. This region is also limited by another curve, the **binodal**. Outside the binodal the two phases cannot coexist, so phase separation cannot take place under any circumstances outside the binodal.

There are some concepts which have not been taken into account in this discussion, which are coherency strain effects and interface energy effects. Although during the initial states of spinodal decomposition the interfaces are very diffuse, there is still an interface energy increase. This interface energy is directly linked to the gradient of the concentration at the interface. That's why it is also called gradient energy. There is a contribution due to coherency strain energy, if the sizes of the atoms making up the solid solution are

different. These two terms add up to the total free energy of the alloy. This defines a new concept, which is known as the **coherent spinodal**. The coherent spinodal is the region where spinodal decomposition takes place taking into account these two effects. It always lies within the chemical spinodal, so its global effect is slightly reducing the spinodal region.

Spinodal decomposition is a very common process which does not only take place in alloys with a stable miscibility gap in their phase diagram. It can also happen in systems in which GP zones form, among others.

In this thesis, we are interested in these regions, since they are the regions were phase separation takes place spontaneously and no energy barriers are present. Determining whether we are inside the spinodal region is slightly more complex for ternary mixtures, since determining the curvature of the free energy landscape is not direct. This issue will be addressed in Section 5.

4. Nucleation in binary mixtures

The most simple case of nucleation takes place in binary mixtures, since the only process that takes place in that case, if we do not consider nucleation at mould walls, is homogeneous nucleation. In that case, the two components are initially mixed together, but they split into two separate phases of space. This process can be led by spinodal decomposition or by nucleation, depending on the value of the concentration of the components. These two components evolve following the Cahn-Hilliard equation (also known as model B), which can reproduce phase separation. Moreover, Cahn-Hilliard equation preserves the total concentration of the components. Together with the Cahn-Hilliard equation we use the string method to calculate the critical states of nucleation and some related magnitudes, like the energy barrier or the radius of the critical droplets. In terms of solving the PDE, we iterate the Cahn-Hilliard equation following a finite differences approximation, together with an IMEX method for time integration.

4.1 Phase evolution

4.1.1 Phase field models

Modeling material systems with several phases can be a quite challenging problem. From a mathematical perspective, these systems are ideally divided in bulk regions, each of which represents a certain phase, separated by sharp interfaces. The evolution of these phases and the separating interfaces is not an easy problem, since the geometry of each region changes with time. This situation is of special interest in mathematical physics (one example of this is the well-known Stefan's problem [32]). Many models have been presented to study these systems, and their classification is out of the scope of this thesis [10].

In general, there are two types of models, which distinguish in the way they treat interfaces. The first ones are front-tracking approaches to interface motion [33, 34]. In these models, the interface is represented explicitly using a Lagrangian mesh. These methods have the advantage that they can describe sharp interfaces and have a very high resolution and excellent accuracy. However, they are quite complex, especially when one is interested in remeshing the interface. That's the reason why we do not use these methods in this thesis.

The second type of models are the phase field models [10, 35]. These models treat interfaces as being diffuse, and they are described using order parameters. The main advantage of these methods is their robustness, compared to front-tracking methods. The loss of sharp interfaces translates to significant boosts in the simplicity and robustness of the models. However, they have one disadvantage, and it is that the mesh has to be fine enough to resolve the interface (this issue is discussed more in detail along this section).

When studying phase separation using phase field models, order parameters are defined. An **order parameter** is a measure of the structural order that distinguishes between phases. In a system with several components there is usually one order parameter for each of them. An order parameter is a variable, ϕ_i for component i, which takes values from 0 to 1 (or from -1 to 1), being 1 inside phase i and 0 outside. The interfaces vary smoothly between 0 and 1, and they are usually the most complex part to model.

Consider a system with N_c components. We define one order parameter for each of them. Each order parameter is equal to 1 inside the region where the corresponding phase lies, and 0 outside. Hence, order parameters are a measure of the concentration of each component at each point in space. If we think of these order parameters as the percentage of component i at a given point, then the following condition

holds:

$$\sum_{i}^{N_c} \phi_i = 1 \tag{22}$$

If we use this condition we can eliminate one order parameter and express it as a function of the other $N_c - 1$ order parameters. This is especially useful for binary mixtures, since this is the simplest case and in that way we can just study one order parameter, ϕ (the other order parameter is $1 - \phi$).

Classically, two equations were presented to model phase separation [35]. The first one is the Allen-Cahn equation, also known as model A, which has the following expression:

$$\frac{\partial \phi_i}{\partial t} = -L_i \frac{\delta F}{\delta \phi_i} \tag{23}$$

In the above equation, ϕ_i are the order parameters for each phase and L_i are related to the atomic mobilities. The derivative at the right hand side is the functional derivative of the total free energy with respect to ϕ_i, which is also the definition of the chemical potential for phase i, μ_i. This equation is non-conservative, that is, the average value of each order parameter is not conserved.

The second equation is the Cahn-Hilliard equation, also known as model B, which has the following expression:

$$\frac{\partial \phi_i}{\partial t} = \nabla \cdot \left(M_i \nabla \frac{\delta F}{\delta \phi_i} \right) \tag{24}$$

In the above equation, M_i is related to the atomic mobility and the derivative at the right hand side is the functional derivative of the total free energy with respect to the i'th order parameter. In that case the equation is conservative, so that the total concentration is preserved for each component. This is the evolution equation considered in this thesis.

4.1.2 The Cahn-Hilliard equation

One of the advantages of the Cahn-Hilliard equation is that it preserves the total concentration of each of the species. To maintain the conservative property of the equation, it is usually combined with periodic boundary conditions or Neumann boundary conditions. All along the thesis these two boundary conditions are considered. Neumann boundary conditions are considered in one dimension and when polar or spherical coordinates are considered. Periodic boundary conditions are considered in cartesian coordinates in two dimensions, since in that way we can solve the Cahn-Hilliard equation in the Fourier space. Although we consider different boundary conditions, we expect to get similar results in both cases.

For binary mixtures we assume that each of our order parameters takes values in $(-1, 1)$. In that case, Eq. 22 is rewritten as:

$$\sum_{i}^{2} \phi_i = 0 \tag{25}$$

However, although the Cahn-Hilliard equation is conservative, the sum of the values of the order parameters at each point is not kept to 0. That is, the Cahn-Hilliard equation does not assure that Eq. 25 is satisfied at each point in the general case. To fulfill this condition an appropriate choice of the mobilities must be made. Otherwise, one of the order parameters must be computed from the other one. Since we are in a binary mixture, this means that we just need to evolve one order parameter, ϕ, which represents the

concentration of one of the components (the other one is simply $-\phi$). Hence, we only have one equation for one of the components.

The term at the right of the Cahn-Hilliard equation (Eq. 24) is the functional derivative of the total free energy with respect to the order parameter. The free energy is a Ginzburg-Landau type energy functional [13], which has the following expression:

$$F(\phi) = \int_\Omega \left(f_0(\phi) + \frac{W^2}{2} |\nabla \phi|^2 \right) d\Omega \tag{26}$$

where Ω is our domain. The gradient term takes into account the energy due to the interface (sharper interfaces have a greater energy), and the first term is the bulk free energy, which is related to the potential energy. The bulk free energy is often simplified to a double well potential.

We consider that our order parameter takes values in $(-1, 1)$, and it represents the surrounding phase (so the nucleating phase is represented by $-\phi$). Hence, $\phi = 1$ outside the nucleus and $\phi = -1$ inside it. We consider a bulk free energy with the following expression: $f_0(\phi) = A\frac{(\phi^2-1)^2}{4}$, for some constant A which is determined by prescribing the value of the interface energy (see section 4.1.3). The division by 4 is left in the expression to simplify some expressions which appear later. Finally, the constant W takes into account the interaction strength between the two phases, and it is related to the interface width. We could also consider the bulk free energy for a regular solution, but for numerical purposes this simpler double well potential is enough.

If the functional derivative is computed, assumin the mobility coefficient $M = 1$, we obtain the Cahn-Hilliard equation for this free energy functional:

$$\frac{\partial \phi}{\partial t} = \Delta \left(-W^2 \Delta \phi + A(\phi^3 - \phi) \right) \tag{27}$$

Observe that this is a fourth order PDE which also contains nonlinear terms. Hence, the equation will be very stiff and some appropriate numerical method will have to be considered to treat these issues.

4.1.3 Model parameters and physical constants

An important goal in the study of binary mixtures is being able to reproduce the value of physical constants from the simulations. To do so, the model parameters cannot take arbitrary values, but they have to fulfill certain relations with respect to physical constants. Two magnitudes are of special interest: the interface energy and the interface width. To find the relation between model parameters and physical parameters we will use the derivation performed by Ryan Davis in his thesis [10], and we will apply it to our case.

From a physical point of view, the interface energy between two phases, a and b, is the difference in free energy per unit area between the phase at one side of an interface (phase a) and the phase at the other side (phase b), assuming no other phase is present. In our model, the interface energy is obtained by considering two semi-infinite phases separated by an interface, and integrating the free energy of this configuration along an axis orthogonal to the surface. That is, if γ is the interface energy (in the binary case there is only one interface energy, which corresponds to an interface separating the two phases), then:

$$\gamma = \int_{-\infty}^{+\infty} \left(f_0(\phi(x)) + \frac{W^2}{2} |\nabla \phi(x)|^2 \right) dx \tag{28}$$

Observe that the previous expression only works when the bulk free energy is null at the bulk regions

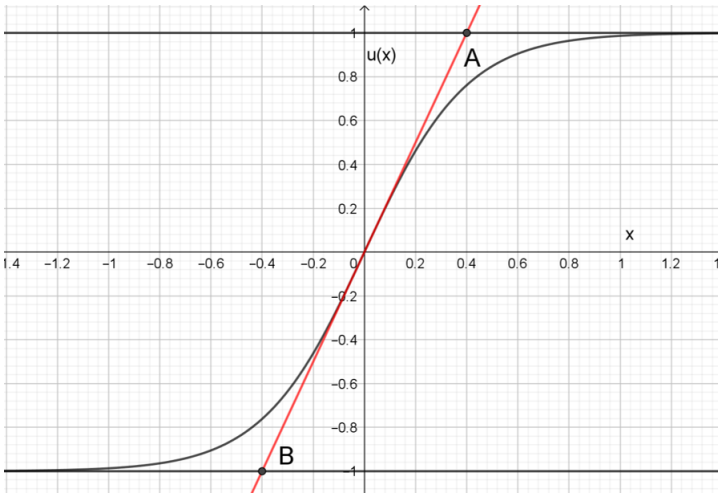

Figure 7: Geometric description of the interface width. In this example the interface width is 0.8.

(when $\phi = \pm 1$, then $f_0(\phi) = 0$), like in the cases we consider in this thesis. Otherwise the term coming from the bulk phases should be subtracted from the computation. The other physical parameter we consider is the interface width, which is a distance related to the width of the interface. It has the following geometric construction (see Fig. 7):

1. We determine the x coordinate where the value of the order parameter is the midpoint of the range of the order parameter. In our case, since ϕ goes from -1 to 1, this point corresponds to $\phi = 0$, which in Fig. 7 corresponds to $x = 0$.
2. The tangent line to the order parameter at the point is drawn.
3. This line takes the maximum and minimum values of ϕ (1 and -1) at A and B, respectively. The interface is then defined as the distance between these two points.

After performing the calculations described above, we get the following analytical expression for the interface width, which is represented by δ:

$$\delta = \frac{2}{|\nabla\phi|_{\phi=0}} \tag{29}$$

The two expressions given by Eqs. 28 and 29 are very complicated to calculate given an arbitrary profile for the order parameter. However, for a stationary state of the Cahn-Hilliard equation, there is a change of variables that allows us to compute these integrals analytically.

A state which is metastable in the free energy landscape (and thus it is stationary for the Cahn-Hilliard equation) minimizes the free energy functional, $\frac{\delta F}{\delta \phi_{eq}} = 0$. On the other hand, the Euler-Lagrange equation determines the profile of the order parameter which minimizes the total free energy of the system (Eq. 26). However, if this integral does not depend explicitly on time (which is the case), then the Euler-Lagrange equation reduces to the Beltrami identity [36]:

$$F - (\nabla\phi)\frac{\partial F}{\partial(\nabla\phi)} = 0 \tag{30}$$

In our case, since $F = f_0(\phi) + \frac{W^2}{2}|\nabla\phi|^2$, the Beltrami identity translates to:

$$f_0(\phi) - \frac{W^2}{2}|\nabla\phi|^2 = 0 \tag{31}$$

This relation, only valid for the equilibrium states of the Cahn-Hilliard equation, allows us to compute the values of the interface energy and interface width analytically, and express it in terms of the model parameters, A and W.

Going back to Eq. 28, using Beltrami's identity and performing a change of variables:

$$\gamma = \int_{-\infty}^{+\infty} 2f_0(\phi)dx = 2\int_{-1}^{1} f_0(\phi)\frac{1}{\nabla\phi}d\phi$$

$$\gamma = 2\int_{-1}^{1} f_0(\phi)\sqrt{\frac{W^2}{2}\frac{1}{f_0(\phi)}}d\phi = \sqrt{2}W\int_{-1}^{1}\sqrt{f_0(\phi)}d\phi = \frac{\sqrt{2A}W}{2}\int_{-1}^{1}(1-\phi^2)d\phi$$

$$\gamma = \frac{2\sqrt{2A}W}{3}$$

Applying Beltrami's identity to Eq. 29 we get:

$$\delta = \frac{2}{\sqrt{\frac{2}{W^2}f_0(\phi)_{\phi=0}}} = \frac{2W}{\sqrt{\frac{A}{2}}}$$

$$\delta = \frac{2\sqrt{2}W}{\sqrt{A}}$$

A change of variables is convenient to simplify a bit these expressions. We define $\lambda = \frac{W}{\sqrt{A}}$, so that $W = \lambda\sqrt{A}$. Then, the previous expressions result in:

$$\gamma = \frac{2\sqrt{2}}{3}A\lambda \tag{32}$$

$$\delta = 2\sqrt{2}\lambda \tag{33}$$

These expressions can be easily inverted, and in that way we can express the model parameters in terms of physical constants. This is an important advantage, because Eqs. 32 and 33 allow us to use physical constants as input parameters in the program. If we do so the expressions which relate the model parameters to physical constants are:

$$\lambda = \frac{\sqrt{2}\delta}{4} \tag{34}$$

$$A = \frac{3\gamma}{\delta} \tag{35}$$

A final observation is that if we write the free energy in Eq. 26 with this change of variables we get the following:

$$F(\phi) = \int_\Omega A\left(\frac{(1-\phi^2)^2}{4} + \frac{\lambda^2}{2}|\nabla\phi|^2\right) d\Omega \tag{36}$$

We see that A is a scale factor in the free energy. This implies that the stationary solutions of the Cahn-Hilliard equation do not depend on the value of A. Instead, A is just a factor which multiplies the total energy. We can, thus, choose whatever value of A we want without changing the final string in the string method. Changing A, however, can change the speed to which we arrive at this solution, since changing A is equivalent to changing the time step. This comes from the Cahn-Hilliard equation: the time derivative is equal to the gradient of the chemical potential (which in turn is equal to the functional derivative of the free energy density). Hence, multiplying the free energy density by a constant factor is equivalent to multiplying the time derivative by a constant factor. However, since the equilibrium concentration profiles are the ones which have a null time derivative, multiplying the time derivative by a constant factor does not alter the equilibrium states. The effect of changing A is changing the speed at which the system reaches the equilibrium state, which in simulations is equivalent to changing the time step, as we will see in future sections. Since changing A keeping λ fixed is equivalent to changing γ keeping δ fixed, we can give the value we want to γ. In particular, for simplicity, we will consider, unless the opposite is said, $\gamma = \frac{\delta}{3}$, so that $A = 1$. The important thing to take into account is to always consider similar values of the interface energy, especially when comparing different simulations with classical nucleation theory.

4.2 One dimensional case

First of all, we study the most simple case, which is nucleation in one dimension for a binary mixture [13]. This case does not have any interest from the physical point of view because nucleation does not occur in one dimension (if the argument explained in Section 3 is reproduced in one dimension, we find that the free energy curve does not present any maximum, so there is no energy barrier to phase separation). However, it is interesting to start with this case because it allows us to study the implementation of the string method and the phase field model and analyze possible difficulties that may appear.

4.2.1 Numerical implementation

First of all, we define some concepts we will refer to all along the thesis related to how the string method works for the Cahn-Hilliard equation. The string consists of a chain of states, which we refer to as images, which is parametrized by arclength under the ℓ_2 norm. For a PDE, like the Cahn-Hilliard equation, each of the states is a profile of the order parameter. That is, we have m profiles along the string, the first of which is the mixed state (a constant concentration profile), and the last of which is the separated state (two bulk regions separated by an interface). We only need to consider an initial string where the initial and final images are within the basin of attraction of these metastable states. For the initial state it is very easy, since the constant concentration profile is already metastable. The final state can be initialized as two separated phases separated by a sharp interface, and the string method will evolve this state to the smooth interface, which is the real metastable state. The intermediate images can be initialized in many ways, although some of them are better than others. This issue is discussed later.

Observe that on the one hand we talk about the initial and final states or images of the string, which are the metastable states. These states correspond to the mixed and separated phases. Hence, they have

a physical meaning, which corresponds to the beginning and the ending of the nucleation process. On the other hand we have the initial string. This initial string is the initial condition we consider for the string method, which is evolved until it converges to the MFEP between the two metastable states. This initial condition does not have any physical meaning, it is only defined in the string method. We can combine both concepts and have an initial state in the initial string, for example. Special care must be taken so as not to confuse these two terms.

In our simulations there are several parameters which we can control. Some of them are related to physical parameters, while some others are related to the numerical implementation.

The physical parameters we can modify act as inputs for our model. They are the interface energy γ, the interface width δ and the mean concentration $\bar{\phi}$, defined as the integral of the concentration profile on the whole domain. We expect this value not to change during time evolution, since the Cahn-Hilliard equation is conservative. Moreover, we define all the images on the string so that they have the same value of the mean concentration (otherwise the transition path found after convergence would have no physical meaning).

The numerical parameters are the number of images along the string m, the number of discretization nodes in the x coordinate N, the time step h and the tolerance for the method to stop tol. The error is defined throughout all the thesis as the ℓ_2 norm of the difference between the current string and the previous one divided by $m \cdot N$, unless we say the opposite. The tolerance is a parameter which serves us as a stopping criterion: if the error becomes smaller than the tolerance, we consider that the method has converged and the string at that iteration is the transition path between the two metastable states.

As for how to evolve the string method, the Cahn-Hilliard equation (Eq. 27) and the free energy take the following form in one dimension:

$$\frac{\partial \phi}{\partial t} = \frac{\partial^2}{\partial x^2}\left(-W^2\frac{\partial^2 \phi}{\partial x^2} + A(\phi^3 - \phi)\right) \tag{37}$$

$$F(\phi) = \int_0^1 \left(f_0(\phi) + \frac{W^2}{2}\left|\frac{\partial \phi}{\partial x}\right|^2\right) dx \tag{38}$$

Eq. 37 is discretized in the spatial coordinate using finite differences. We divide the interval into N intervals of the same length, and we consider the nodes at the center of each interval, naming the node at interval i as x_i, where $i = 0, ..., N-1$. They are separated by a distance of $dx = \frac{1}{N}$, and they are at positions $x_0 = dx/2$, $x_1 = 3dx/2$, ..., $x_{N-1} = 1 - dx/2$. There is actually no need to consider centered nodes in one dimension, but in that way we will avoid some problems in two and three dimensions. The expression ϕ is used to refer to the vector with the following components: $\phi = (\phi_0 = \phi(x_0), ..., \phi_{N-1} = \phi(x_{N-1}))$. To calculate first and second order derivatives at node $i \in (1...., N-2)$ we use the following discretizations [37], which have second order convergence in space:

$$\frac{\partial \phi_i}{\partial x} \approx \frac{\phi_{i+1} - \phi_{i-1}}{2\Delta x} \tag{39}$$

$$\frac{\partial^2 \phi_i}{\partial x^2} \approx \frac{\phi_{i-1} + \phi_{i+1} - 2\phi_i}{\Delta x^2} \tag{40}$$

Two different boundary conditions are considered, periodic boundary conditions and Neumann boundary conditions. In both cases two fictitious nodes are created, ϕ_{-1} and ϕ_N. The value of the function at these nodes depends on the boundary conditions we consider.

- **Periodic boundary conditions:** in this case, we impose: $\phi(0) = \phi(1)$ and $\frac{\partial\phi}{\partial x}(0) = \frac{\partial\phi}{\partial x}(1)$. Both conditions are satisfied if we impose $\phi_{-1} = \phi_{N-1}$ and $\phi_0 = \phi_N$. Using this notation we can express the first and second derivatives of the function ϕ at nodes 0 and $N-1$ using Eqs. 39 and 40. Moreover, we can write both derivatives in matricial form:

$$\frac{\partial\phi}{\partial x} = D\phi \tag{41}$$

$$\frac{\partial^2\phi}{\partial x^2} = L\phi \tag{42}$$

where:

$$D = \frac{N}{2}\begin{pmatrix} 0 & 1 & 0 & 0 & \dots & 0 & 0 & -1 \\ -1 & 0 & 1 & 0 & \dots & 0 & 0 & 0 \\ 0 & -1 & 0 & 1 & \dots & 0 & 0 & 0 \\ \vdots & \vdots & \vdots & \vdots & \ddots & \vdots & \vdots & \vdots \\ 0 & 0 & 0 & 0 & \dots & -1 & 0 & 1 \\ 1 & 0 & 0 & 0 & \dots & 0 & -1 & 0 \end{pmatrix} \tag{43}$$

$$L = N^2\begin{pmatrix} -2 & 1 & 0 & 0 & \dots & 0 & 0 & 1 \\ 1 & -2 & 1 & 0 & \dots & 0 & 0 & 0 \\ 0 & 1 & -2 & 1 & \dots & 0 & 0 & 0 \\ \vdots & \vdots & \vdots & \vdots & \ddots & \vdots & \vdots & \vdots \\ 0 & 0 & 0 & 0 & \dots & 1 & -2 & 1 \\ 1 & 0 & 0 & 0 & \dots & 0 & 1 & -2 \end{pmatrix} \tag{44}$$

- **Neumann boundary conditions:** in this case, we impose: $\frac{\partial\phi}{\partial x}(0) = 0$ and $\frac{\partial\phi}{\partial x}(1) = 0$. Both conditions are satisfied if we impose $\phi_{-1} = \phi_0$ and $\phi_N = \phi_{N-1}$. As in the periodic case, we can express the first and second derivatives of the function ϕ at nodes 0 and $N-1$ using Eq. 39 and (40), and we can write them in matricial form:

$$\frac{\partial\phi}{\partial x} = D\phi \tag{45}$$

$$\frac{\partial^2\phi}{\partial x^2} = L\phi \tag{46}$$

where:

$$D = \frac{N}{2}\begin{pmatrix} -1 & 1 & 0 & 0 & \dots & 0 & 0 & 0 \\ -1 & 0 & 1 & 0 & \dots & 0 & 0 & 0 \\ 0 & -1 & 0 & 1 & \dots & 0 & 0 & 0 \\ \vdots & \vdots & \vdots & \vdots & \ddots & \vdots & \vdots & \vdots \\ 0 & 0 & 0 & 0 & \dots & -1 & 0 & 1 \\ 0 & 0 & 0 & 0 & \dots & 0 & -1 & 1 \end{pmatrix} \tag{47}$$

$$L = N^2\begin{pmatrix} -1 & 1 & 0 & 0 & \dots & 0 & 0 & 0 \\ 1 & -2 & 1 & 0 & \dots & 0 & 0 & 0 \\ 0 & 1 & -2 & 1 & \dots & 0 & 0 & 0 \\ \vdots & \vdots & \vdots & \vdots & \ddots & \vdots & \vdots & \vdots \\ 0 & 0 & 0 & 0 & \dots & 1 & -2 & 1 \\ 0 & 0 & 0 & 0 & \dots & 0 & 1 & -1 \end{pmatrix} \tag{48}$$

Going back to the discretized Cahn-Hilliard equation, in both cases we can write it with the following notation:

$$\frac{\partial \phi}{\partial t} = L(-W^2 L\phi + A(\phi^3 - \phi)) \tag{49}$$

where $\phi^3 = (\phi_0^3, \phi_1^3, ..., \phi_{N-1}^3)$.

There are many options to solve this ODE. The problem with the Cahn-Hilliard equation is that it is both nonlinear and stiff, due to the fourth order derivative term. The second issue can be addressed considering implicit methods, but since the equation is nonlinear they are quite complicated to implement. Two methods are proposed to solve Eq. 49.

The first one is the forward Euler method, or Euler Method for simplicity (EM). This is the most simple numerical method to solve ODEs, and there is no complication in terms of implementation. However, it has the disadvantage that usually very small time steps have to be considered to achieve convergence. If the time step is taken too large then the program diverges. Moreover, this method has linear convergence in time.

The second option is to consider a so called implicit-explicit method (IMEX), or semi-implicit method [37]. This method consists on splitting the equation in an implicit part, which contains the linear terms, and an explicit part, which contains the nonlinear terms. The advantage of this method is that the stiff term, which is the fourth order derivative, is precisely the one that is considered implicit. In that way stiffness issues are much more easily handled. Moreover, the equation can be solved at each iteration explicitly, since the fourth order derivative term is invertible, but the nonlinear term needs not be inverted because it is considered explicit.

Other options to solve the ODE would include Runge-Kutta methods or ODE solvers already implemented in libraries. However, as a first step we consider the two most simple cases, since we are mainly interested in the program to be fast (this is not very important in the one dimensional case, but it will be crucial for two and three dimensions). We will see that especially the IMEX method is already enough for our purposes.

First of all we consider the forward Euler method, which treats all the right hand side of the Cahn-Hilliard equation explicitly. The equation we get after discretizing Eq. 49 in time, using a time step of h, is the following (where ϕ^n is the value of the vector function ϕ at time nh, where $n = 0, 1....$):

$$\phi^{n+1} = \phi^n + hL(-W^2 L\phi^n + A((\phi^n)^3 - \phi^n)) \tag{50}$$

The second solution comes from considering the IMEX method. If the fourth order derivative terms is treated implicitly and inverted, the final expression for ϕ^{n+1} is:

$$\phi^{n+1} = (I + hW^2 L^2)^{-1}(\phi^n + hAL((\phi^n)^3 - \phi^n)) \tag{51}$$

where I is the $N \cdot N$ identity matrix.

These two methods are tested for both boundary conditions. A similar performance is expected in terms of convergence, since both of them have linear convergence in time. However, a smaller time step is expected to be necessary with the forward Euler method for numerical stability.

All the programs used in this thesis, unless we say the opposite, have been coded using Python language. Some standard libraries used throughout the whole thesis are numerical python (NumPy), scientific python (SciPy) and Matplotlib.

4.2.2 Simulations and results

The main goal in these 1d simulations is to check that the method developed until now works well and in accordance to what we expect from classical nucleation theory. Observe that, according to classical nucleation theory, in one dimension there should be no energy barrier to phase separation for any value of the concentration. However, in our model, the bulk free energy density has a negative second derivative for concentrations under $\bar{\phi}^* = \frac{\sqrt{3}}{3} \approx 0.577$, which is the condition for which we enter the spinodal region. Hence, we expect the method to find that there is no barrier to nucleation for concentrations under this limit, but we may find energy barriers for concentrations over the limit concentration. These energy barriers do not have any physical meaning. They appear because classical nucleation theory assumes, in one dimension, that the contribution of interfaces to the energy is a constant and does not depend on the radius of the droplet (in two dimensions, for example, the interface term depends linearly on the radius because the greater the radius of the droplet the greater the length of the interface). However, in simulations interfaces are diffuse, so the contribution of the interface depends on the width of the interface and its position, so it is not a constant term. That's the reason why critical radii should be comparable to the interface width. We want to check, then, that when we are in the spinodal region there is no barrier to nucleation, and that the physical parameters, which will be the inputs, are the ones obtained numerically from the results of the simulations.

An observation before analyzing the results is that, although the Cahn-Hilliard equation does not have an analytical solution in the general case, we can find an analytical stationary solution in the one dimensional case. This solution is obtained by solving the Beltrami identity. This solution extends from $-\infty$ to $+\infty$, but it is also a good solution if we consider Neumann boundary conditions on a finite domain (in our case $(0, 1)$), and we can use it to compare our results. For the details of this solution see appendix B. We use this solution as a way to check that the string converged correctly.

First of all a comparison between the forward Euler method and the implicit-explicit method (which from now on will be referred to as EM and IMEX for simplicity) is done. To do so, the same simulation is performed using each of the methods and the results are compared, as well as the number of iterations the program took to reach the stable string. The string is initialized by considering an initial constant profile of value $\bar{\phi}$ and a final profile consisting of a two phase system, the first of which has a value $\phi = -1$ and the second one $\phi = 1$, separated by a sharp interface. The intermediate images are declared as two phase regions as well, simulating the growth of the nucleus: the transition shifts to the right, and the value of the order parameter is always equal to -1 inside the droplet. The concentration outside the droplet is determined by imposing that the total concentration at each image is the same.

Table 1 shows the results obtained considering Neumann boundary conditions for different values of the mean concentration both for the EM and the IMEX method. $m = 50$ images were considered along the string, the spatial coordinate was discretized in $N = 100$ nodes, values of $\delta = 0.05$ and $\gamma = \delta/3$ were considered and different values of h and tol were considered for each of the methods.

In all cases we get pretty similar results for the energy barriers (the largest difference happens for $\bar{\phi} = 0.60$, but it is because the energy barrier is very small, so more images on the string should be considered to resolve it better). However, there is a crucial difference: the IMEX method is faster than the EM by approximately one order of magnitude. If we check the total CPU time, we see that in all cases the EM ran for approximately 20 times the total CPU time for the IMEX method. We can also observe that the IMEX method can perform more iterations per second than the EM, although the results fluctuate a lot and no definitive conclusions can be derived from it. In principle both methods are comparable in terms of efficiency, since the matrix c in the IMEX method can be computed beforehand and is constant with time,

Mean concentration	Time integration method	Energy barrier	Number of iterations	Total CPU time (seconds)	Iterations per second
0.55	EM	0.00	432039	1649.77	261.88
	IMEX	0.00	18604	57.88	278.01
0.60	EM	$1.33 \cdot 10^{-5}$	357021	1328.15	268.81
	IMEX	$1.09 \cdot 10^{-5}$	18054	57.88	278.01
0.65	EM	$1.59 \cdot 10^{-4}$	277762	969.96	286.36
	IMEX	$1.55 \cdot 10^{-4}$	11919	39.10	298.35
0.70	EM	$5.86 \cdot 10^{-4}$	224842	794.22	283.10
	IMEX	$5.80 \cdot 10^{-4}$	17367	58.21	298.95
0.75	EM	$1.40 \cdot 10^{-3}$	166724	598.49	278.57
	IMEX	$1.40 \cdot 10^{-3}$	8795	29.42	296.28
0.80	EM	$2.76 \cdot 10^{-3}$	126394	486.46	259.82
	IMEX	$2.75 \cdot 10^{-3}$	17842	60.22	321.42

Table 1: Comparison between the Euler method and implicit-explicit method for Neumann boundary conditions.

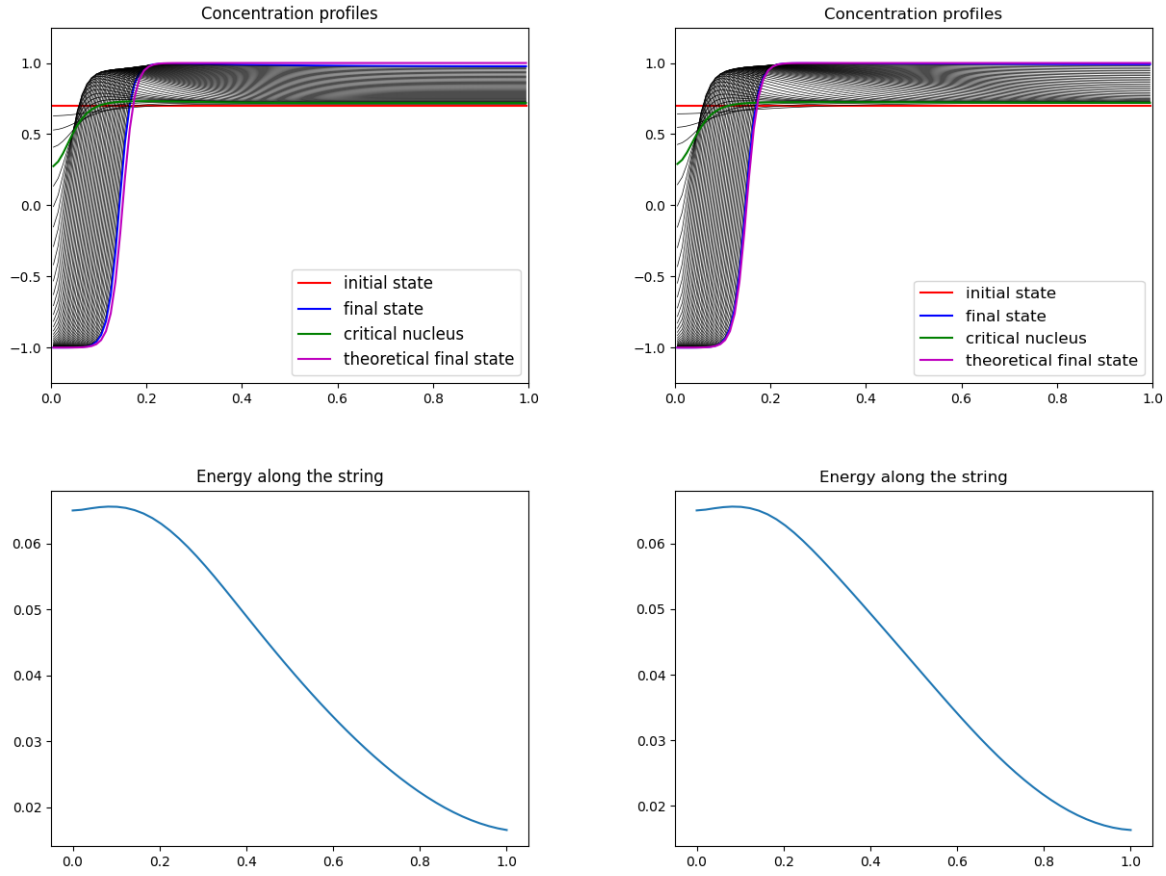

Figure 8: Final string concentration profiles and energy along the string for the two time integration methods and a mean concentration of $\bar{\phi} = 0.70$, for Neumann boundary conditions. Left: EM. Right: IMEX.

so we only compute it at the beginning of the method. Hence, in both cases each iteration consists basically on performing a matrix multiplication.

These results are not very precise due to two factors. The first one is that a time step of $h = 10^{-5}$ was considered for the IMEX method, but for the EM a time step of $h = 10^{-7}$ was taken for the method to converge (as discussed before), since for larger time steps the method diverged. The second one is that the tolerance considered in both cases is different. That is because, since the EM requires a smaller time step, the error at each iteration is always smaller than in the IMEX method. Moreover, the error does not scale linearly with h, so defining the error normalized by h does not solve this issue. Hence, a tolerance was qualitatively chosen such that the final concentration profile was close to the theoretical one (the one coming from solving the Beltrami identity, see appendix B). We chose $tol = 10^{-9}$ for the EM and $tol = 10^{-8}$ for the IMEX method. The final concentration profiles and the energy along the string for a concentration of $\bar{\phi} = 0.70$ are plotted in Fig. 8. In both cases the final states are really similar to the analytical solution of the Cahn-Hilliard equation, although the IMEX is apparently a bit better. We can also check that even when we find a critical nucleus its radius is comparable to the interface width, as expected.

The conclusion is that, since the time step for the EM is smaller, the program needs to run for longer periods of time, so the IMEX method is the best option for computational efficiency. Moreover, the IMEX method is better to treat the stiffness of the problem.

With respect to the spinodal region, Table 1 shows a result which we wanted to check: the string method only finds an energy barrier outside the spinodal region, which is the region with a value of the mean concentration greater than $\bar{\phi}^* = \frac{1}{\sqrt{3}} \approx 0.577$. This is consistent with the fact that for a concentration of $\bar{\phi} = 0.55$ there is no energy barrier. Moreover, the energy barrier is very small for values close to the spinodal, something we already expected, since as we approach the spinodal the energy barrier tends to disappear.

Another important aspect which has to be taken into account when studying convergence is the initial string we choose. Depending on how far away from the final solution our initial string is the program requires a different number of iterations to converge, and sometimes it may not converge at all, if the initial string is poorly chosen. In particular, we are interested in reducing as much as possible the total number of iterations, so the initial string is desired to be close to the final one. This issue will be especially important in higher dimensions.

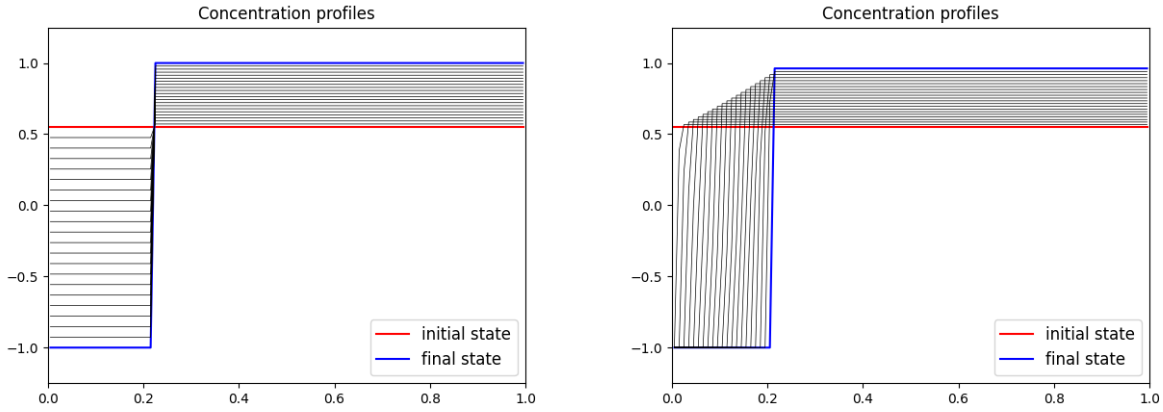

Figure 9: Two possible initial strings. Left: Linear interpolation. Right: The nucleus forms and grows.

In one dimension we already know the shape of the initial and final states at equilibrium, corresponding to the mixed state and separated state, respectively. The problem comes when defining the intermediate

images of the string. One way to do it is by simply linearly interpolating between the initial and the final state (see Fig. 9, left plot). This initialization, although quite simple, is not very realistic from a physical point of view. When a phase nucleates, first of all the nucleus is formed and then it grows. Hence, the second option is to consider that the intermediate images have a sharp interface which shifts from left to right, but in all of them the concentration near $x = 0$ is -1 (see Fig. 9, right plot). The concentration outside the droplet in the second case is fixed imposing that the mean concentration of each profile has a prescribed value ($\bar{\phi}$).

As an example of the problems which can take place for different initial strings consider a concentration profile with $\bar{\phi} = 0.7$, $N = 100$, $m = 50$, $\delta = 0.05$ and a time step of $h = 10^{-6}$ (with a tolerance of $tol = 10^{-8}$). We run the program with the two initial strings described above using the IMEX method (see Fig. 9). In the second case (nucleus forms and grows), the program converges after 22484 iterations, reaching the expected profile according to nucleation theory (formation of the nucleus and growth). However, in the first case (linear interpolation), the program requires 77788 iterations. Moreover, the error starts decreasing, but after over 10000 iterations it starts to oscillate until the string is close enough to the final one. Only then the error starts to decrease monotonously. This is a very important issue to take into account, especially in higher dimensions, because this bad behaviour of the error can imply that we consider that we have reached a solution which actually is not.

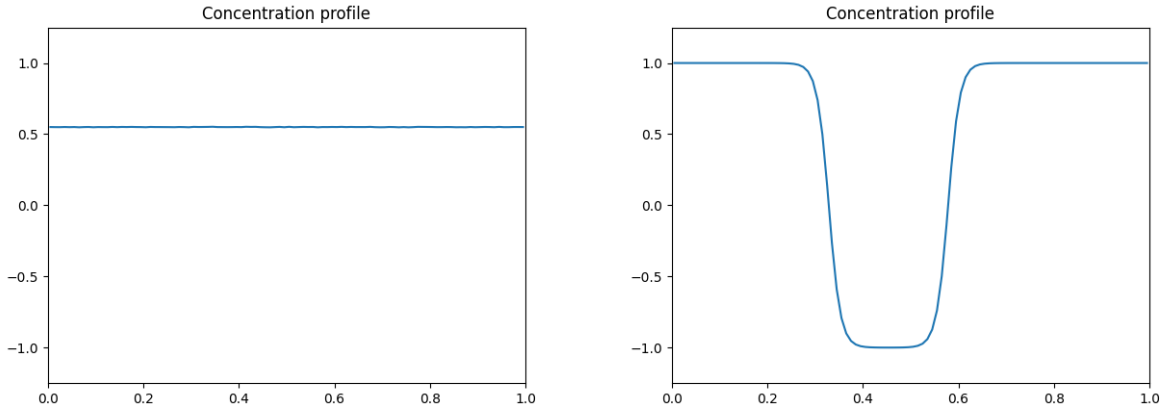

Figure 10: Initial and final concentration profiles when some noise is added to the initial constant concentration profile.

One more test can be performed related to the spinodal region. Since for concentrations bellow $\bar{\phi}^*$ there is no energy barrier, the constant concentration profile is an unstable equilibrium state. That is, if a small perturbation is added to the initial constant profile of the string, the initial state should converge to the separated state instead of the mixed state. This can be checked considering a concentration profile with average concentration $\bar{\phi} = 0.5$, with random gaussian noise with a variance of 10^{-3} added to the initial state. This state was evolved using the Cahn-Hilliard equation (here we do not use the whole string method, since we are only interested in analyzing the behaviour of the initial state). The convergence was quite slow, but we observed that the initial state converged to the separated state. Both the initial and the final states are plotted in Fig. 10. Observe that the final profile has a different shape than in Fig. 8, since phase separation can occur in any part of the domain.

Consider now periodic boundary conditions at both ends. In that case phase separation can take part anywhere in the domain, and we consider that it occurs at $x = 0.5$. Hence, the initial state of the string at

equilibrium has the same shape as in the Neumann boundary case (constant profile), and the final one has a well at $x = 0.5$ with value -1 inside the well and value 1 outside. The intermediate images on the string are initially defined as in the Neumann case: the droplet forms and then it grows, all of them with sharp interfaces which are smoothed by the string method.

With respect to the spinodal region, we expect to observe the same behaviour of the solution as in the Neumann case. We simulate phase separation using both the EM and the IMEX method. Table 2 shows the results we got for several values of the mean concentration. The rest of the parameters were: $m = 50$, $N = 100$, $\delta = 0.05$, $\gamma = \delta/3$ and different values of h and tol for each of the methods.

Mean concentration	Time integration method	Energy barrier	Number of iterations	Total CPU time (seconds)	Iterations per second
0.55	EM	0.00	300471	753.24	297.16
	IMEX	0.00	9490	39.95	308.94
0.60	EM	$4.39 \cdot 10^{-5}$	223830	531.15	320.69
	IMEX	$3.77 \cdot 10^{-5}$	12342	22.64	297.48
0.65	EM	$4.53 \cdot 10^{-4}$	170336	616.26	301.22
	IMEX	$4.40 \cdot 10^{-4}$	6735	32.24	252.70
0.70	EM	$1.51 \cdot 10^{-3}$	185631	652.35	266.00
	IMEX	$1.50 \cdot 10^{-3}$	8147	26.93	347.01
0.75	EM	$3.53 \cdot 10^{-3}$	173526	541.88	266.78
	IMEX	$3.53 \cdot 10^{-3}$	9345	38.99	344.22
0.80	EM	$6.93 \cdot 10^{-3}$	144565	1130.9	265.69
	IMEX	$6.93 \cdot 10^{-3}$	13421	36.17	262.37

Table 2: Comparison between EM and IMEX method for periodic boundary conditions.

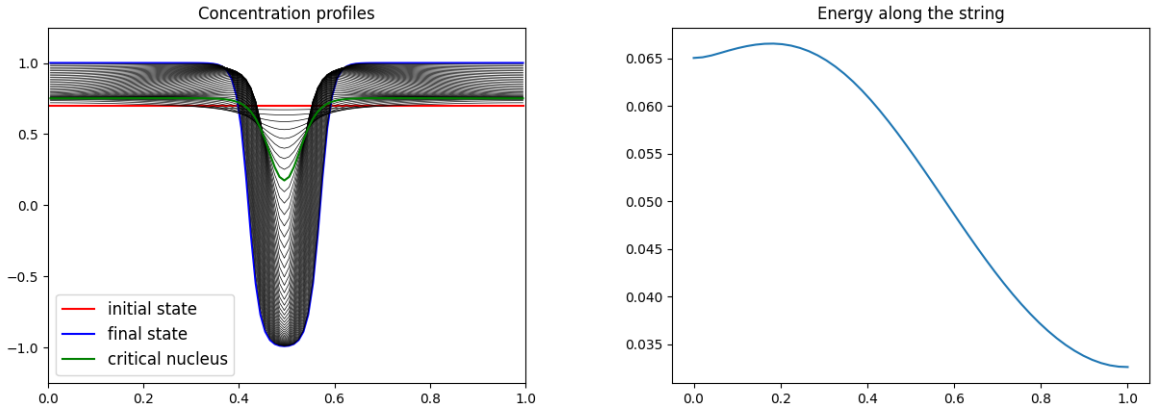

Figure 11: Final string concentration profiles and energy along the string for the two time integration methods and a mean concentration of $\bar{\phi} = 0.70$, for periodic boundary conditions. Left: EM. Right: IMEX.

We get similar results to the Neumann boundary conditions in terms of convergence (same order of magnitude in the number of iterations and the total CPU time). We also observe that the number of iterations per second oscillates a lot, and in some cases the IMEX method performs more iterations per second than the EM, while in some cases it is the opposite. This is not rare, since the CPU time can fluctuate a lot when running the same program several times, but we cannot make any conclusion on whether the IMEX method is less expensive (in terms of the time it requires to perform one iteration).

We also find that bellow the critical value of the concentration $\bar{\phi}^* = \frac{1}{\sqrt{3}}$ we enter the spinodal region and there is no barrier to nucleation, as expected. The final concentration profiles along the string and the

energy along the string for a value of $\bar{\phi} = 0.7$ are plotted in Fig. 11. Hence, the IMEX method performs better than the EM both for Neumann and periodic boundary conditions, as expected.

The conclusions are that the string method performs well when finding transition pathways, from a qualitative point of view. Moreover, the IMEX method is quite efficient to solve the ODEs. Hence, from now on we will only use the IMEX method, since it performs better to iterate the Cahn-Hilliard equation, and it is quite faster than the EM.

4.3 Two dimensional case: Polar coordinates

The two dimensional case is of much more interest than the one dimensional, since classical nucleation theory predicts that critical nuclei appear during phase separation. Hence, we can compare the results we get from simulations with classical results to check with a greater accuracy the behaviour of the string method. The main disadvantage is that in this case we do not have an analytical expression for the solution to the Cahn-Hilliard equation.

Since in binary mixtures nuclei have roughly circular shape we can simplify the problem very much. In particular, we can simply simulate the radial profile of the critical nucleus, working with polar coordinates, since the angular component is expected to be constant. To check that this is true, two types of simulations are performed: one in two dimensions in cartesian coordinates and another one in one dimension using polar coordinates.

In this section, Neumann boundary conditions will be assumed in all the boundary. We have seen that the method performs well in one dimension for both Neumann and periodic boundary conditions, so the first case will be enough to compare to classical nucleation theory.

4.3.1 Numerical implementation

First of all we simulate phase separation in polar coordinates. Our coordinate is the radial component of the nucleus (we assume cylindrical symmetry), and it takes the values $r \in (0, 1)$ (we simulate a circular domain of radius 1). We consider Neumann boundary conditions at both $r = 0$ and $r = 1$ (in the first case, this is a common assumption to avoid problems when computing the Laplacian at $r = 0$).

The expression of the Laplacian of a two dimensional function $\phi(r, \theta)$ in polar coordinates is the following:

$$\Delta\phi = \frac{1}{r}\frac{\partial}{\partial r}\left(r\frac{\partial\phi}{\partial r}\right) + \frac{1}{r^2}\frac{\partial^2\phi}{\partial\theta^2} = \frac{1}{r}\frac{\partial\phi}{\partial r} + \frac{\partial^2\phi}{\partial r^2} + \frac{1}{r^2}\frac{\partial^2\phi}{\partial\theta^2} \tag{52}$$

Since in our case we are assuming we have cylindrical symmetry, the last term is zero because the second derivative with respect to the angle is zero. With this definition of the Laplacian, the Cahn-Hilliard equation in two dimensions (see Eq. 27) is:

$$\frac{\partial\phi}{\partial t} = \Delta\left(-W^2\Delta\phi + A(\phi^3 - \phi)\right) \tag{53}$$

The equation is discretized in the same way as the one dimensional equation, using finite differences. The first order derivative has the same expression as in one dimension and the Laplacian has the following expression:

$$\Delta\phi_i = \frac{1}{r_i}\frac{\partial\phi_i}{\partial r} + \frac{\partial^2\phi_i}{\partial r^2} \approx \frac{1}{r_i}\frac{\phi_{i+1} - \phi_{i-1}}{2dr} + \frac{\phi_{i+1} - 2\phi_i + \phi_{i-1}}{dr^2}$$

However, we must take special care for the $r = 0$ value. In the previous expression, if we take $r = 0$ we have a division by zero, which leads to values tending to infinity near the origin unless Neumann boundary conditions are considered at $r = 0$, in which case we have an indetermination. The simplest way to solve this problem is considering the central node at each interval. That is, instead of considering the spatial discretization nodes $r \in \{r_0 = 0, r_1 = dr, r_2 = 2dr, ..., r_{N-2} = 1 - dr, r_{N-1} = 1\}$, where $dr = 1/(N-1)$, considering $r \in \{r_0 = dr/2, r_1 = 3dr/2...., r_{N-1} = 1 - dr/2\}$. and $dr = 1/N$. In that way we avoid computing the solution at $r = 0$, which is a source of problems.

To impose Neumann boundary conditions we create two artificial nodes, $r_{-1} = -dr/2$ and $r_N = 1+dr/2$. If we want to compute the derivative of a function ϕ at $r = 0$ we use:

$$\frac{\partial \phi}{\partial r}(r = 0) = \frac{\phi(r_0) - \phi(r_{-1})}{dr} = 0$$

Hence, we must impose $\phi_{-1} = \phi_0$, and similarly $\phi_N = \phi_{N-1}$. These are the same expressions we used in one dimension, although in one dimension it is not necessary to consider centered nodes because the Laplacian does not present any problem at $x = 0$. However, for cohesion in the notation, we use the same discretization in both cases.

We can thus write the spatial first order derivative with respect to r and the Laplacian in matricial forms in the same way we did it in one dimension. If we use the same notation, it can be showed that the expressions are:

$$D = \frac{N}{2}\begin{pmatrix} -1 & 1 & 0 & 0 & ... & 0 & 0 & 0 \\ -1 & 0 & 1 & 0 & ... & 0 & 0 & 0 \\ 0 & -1 & 0 & 1 & ... & 0 & 0 & 0 \\ \vdots & \vdots & \vdots & \vdots & \ddots & \vdots & \vdots & \vdots \\ 0 & 0 & 0 & 0 & ... & -1 & 0 & 1 \\ 0 & 0 & 0 & 0 & ... & 0 & -1 & 1 \end{pmatrix} \tag{54}$$

$$L = N^2\begin{pmatrix} -2 & 2 & 0 & 0 & ... & 0 & 0 & 0 \\ 2/3 & -2 & 4/3 & 0 & ... & 0 & 0 & 0 \\ 0 & 4/5 & -2 & 6/5 & ... & 0 & 0 & 0 \\ \vdots & \vdots & \vdots & \vdots & \ddots & \vdots & \vdots & \vdots \\ 0 & 0 & 0 & 0 & ... & \frac{1-2dr}{1-3dr/2} & -2 & \frac{1-dr}{1-3dr/2} \\ 0 & 0 & 0 & 0 & ... & 0 & \frac{1-dr}{1-dr/2} & \frac{-1+dr}{1-dr/2} \end{pmatrix} \tag{55}$$

We can write the Cahn-Hilliard equation discretized in space. Considering $\phi = (\phi_0, \phi_1...., \phi_{N-1})$ the vector solution, the equation has the following expression:

$$\frac{\partial \phi}{\partial t} = L\left(-W^2 L\phi + A(\phi^3 - \phi)\right) \tag{56}$$

To solve the time derivatives we use the IMEX method. As in one dimension the final expression for ϕ^{n+1} is:

$$\phi^{n+1} = (I + hW^2L^2)^{-1}(\phi^n + hAL((\phi^n)^3 - \phi^n)) \tag{57}$$

This expression is the same as in the one dimensional case, but with a different expression for the Laplacian. Moreover, the values of the constants A and $W = \lambda^2 A$ are the same as in one dimension. This

happens because the definition of the interface energy and interface width are the same, they only depend on the energy functional, which is the same in both cases. Hence, the relation between model parameters and physical magnitudes is the same, and we can use the same expressions discussed in Section 4.1.3.

4.3.2 Simulations and results

The first thing we are interested in testing is whether the energy barrier disappears inside the spinodal region or not, as in one dimension. The limit value of the concentration under which we do not expect nucleation to take place is $\bar{\phi}^* = \frac{1}{\sqrt{3}} \approx 0.577$. Table 3 shows the results of simulating phase separation for several values of the mean concentration. The values of the rest of the parameters are: $N = 100$, $m = 50$, $\delta = 0.05$, $\gamma = \delta/3$, $h = 10^{-5}$ and a tolerance of $tol = 10^{-8}$.

Mean concentration	Energy barrier
0.55	0.00
0.56	0.00
0.57	0.00
0.58	0.00
0.59	$2.49 \cdot 10^{-6}$
0.60	$8.41 \cdot 10^{-6}$
0.61	$1.44 \cdot 10^{-5}$
0.62	$2.12 \cdot 10^{-5}$
0.63	$3.06 \cdot 10^{-5}$

Table 3: Energy barrier for different values of the mean concentration

We see that the energy barrier appears for a value of the mean concentration $\bar{\phi} = 0.59$. We expected the energy barrier to appear at $\bar{\phi} = 0.58$, but that's not the case. The reason why this happens is that the energy barrier for $\bar{\phi} = 0.58$ is very small, since the energy barrier tends to zero as we approach the spinodal region. Considering more images on the string or smaller tolerances are possible solutions to get the exact results. However, neglecting this fact, the results are consistent with what we expected. Moreover, the energy barrier increases with the mean concentration, a result also according to classical nucleation theory.

Our next goal is to compare the results from simulations to classical nucleation theory. The first thing we need to consider is under which assumptions phase field dynamics are good approximations of classical nucleation theory. The main problem comes from the diffuse interface approximation of the phase field method. Classical nucleation theory considers interfaces to be sharp, so to get comparable results we must be in this regime. We only get this when the critical nucleus size is much larger than the interface width (a reasonable approximation is that the interface width is around ten times smaller than the critical nucleus radius). However, this poses a problem in implementation, since the interface width is determined by the mesh resolution. If we want to decrease its value to very small values we have to discretize using more nodes, which in turn increases the complexity of the problem quadratically (since we compute matrices of size $N \cdot N$).

There is a second problem. In classical nucleation theory, the order parameter takes a value of -1 inside the critical nucleus and 1 outside. However, experimentally we found that this only happens for very high values of the mean concentration. If the concentration is not high enough the critical nucleus profile does not reach the value -1 at $r = 0$, it only reaches some intermediate value. For example, for a range of values of the mean concentration from $\bar{\phi} = 0.7$ to $\bar{\phi} = 0.85$ and $\delta = 0.05$, $\gamma = \delta/3$, $N = 100$, $m = 50$,

$h = 10^{-5}$ and $tol = 10^{-7}$, we get the concentration profiles in Fig. 12. The minimum value of the critical concentration profile ($r = 0$) is higher than -1 in all cases, so the profile is not the one predicted by classical nucleation theory. Hence, we need to consider very large values of the concentration, to be closer to the binodal. This is an additional problem because for high mean concentrations the final state has a small radius, and so we will need to consider more nodes again to resolve properly the string.

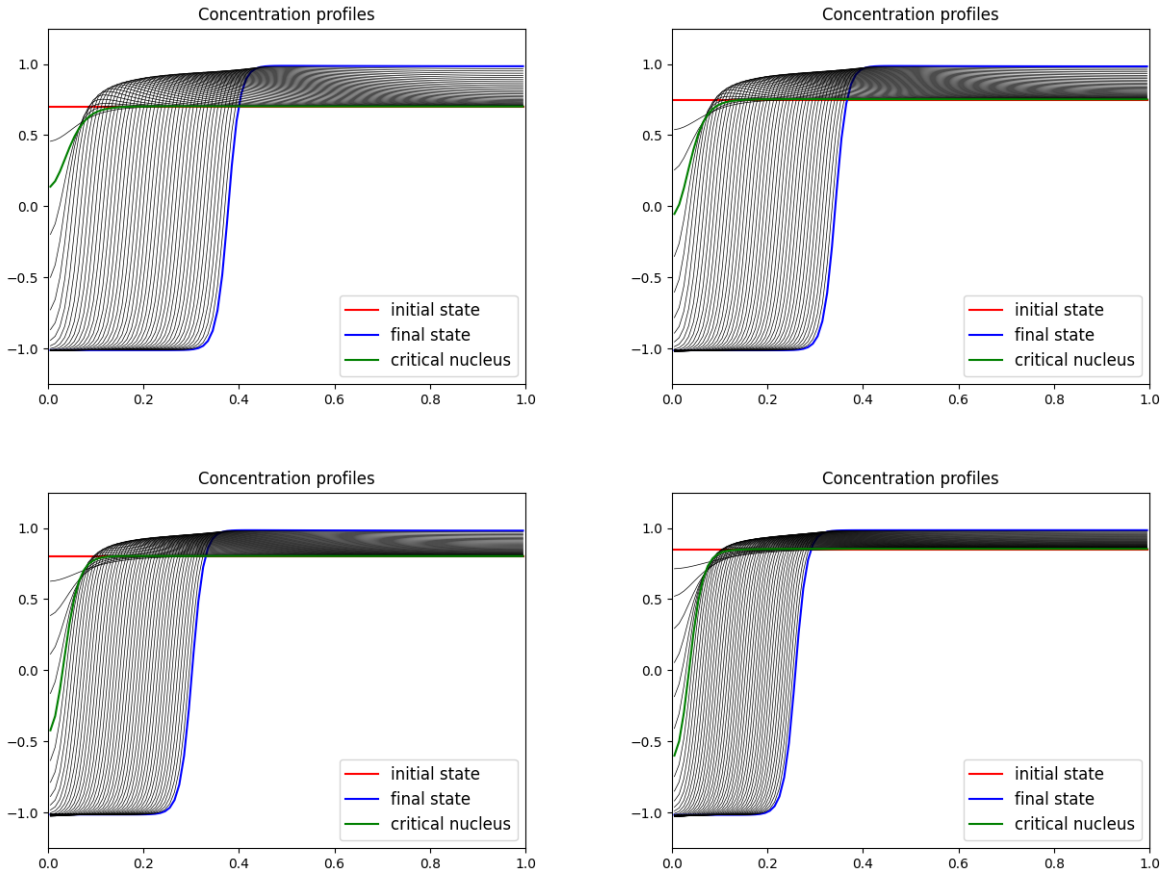

Figure 12: Final string profile for several mean concentrations. Upper left: $\bar{\phi} = 0.7$. Upper right: $\bar{\phi} = 0.75$. Lower left: $\bar{\phi} = 0.8$. Lower right: $\bar{\phi} = 0.85$.

To compute classical nucleation results we use the equations derived in Section 3.1 (Eqs. 7 and 8):

$$r^* = \frac{\gamma_{SL}}{2\Delta G_V}$$

$$\Delta G^*_{hom} = \frac{\pi \gamma^2_{SL}}{2\Delta G_V}$$

In these two expressions, the value of γ_{SL} is known (it is an input for our model), and we just have to determine the relation between ΔG_V and the model parameters. We calculate ΔG_V as the difference in chemical potential between the mixed phase and the separated phase. The definition of the chemical potential is quite ambiguous and still under debate [38]. For our purposes, we define the chemical potential as the functional derivative of the free energy with respect to the mean concentration. With this definition

ΔG_V has the correct dependency on $\bar{\phi}$, as we will see in our results. However, numerical results may not be comparable directly with theoretical results because they will differ by some factor. If we write f_0 as the bulk free energy and f_I as the interface free energy, we get the following expression:

$$\mu = \frac{\delta f}{\delta \phi} = \mu^0 + \mu^I = \frac{\partial f_0}{\partial \phi} - \nabla \cdot \left[\frac{\partial f_I}{\partial (\nabla \phi)} \right] = A(\phi^3 - \phi) - \lambda^2 A \nabla^2 \phi \tag{58}$$

The term ΔG_V is then: $\Delta G_V = \mu_f - \mu_0$, where μ_0 is the chemical potential of the liquid phase (in the mixed state) and μ_f is the chemical potential of the nucleated phase. Since we consider that both the liquid and the nucleated phase are bulk regions with constant concentrations, the gradient term does not contribute to the computation of the chemical potential. Moreover, in the nucleated phase the value of the order parameter is $\phi = -1$, so the chemical potential of this region is null. Hence, the chemical potential difference for a system with mean concentration $\bar{\phi}$ is equal to: $\Delta G_V = A(\bar{\phi} - \bar{\phi}^3)$. Observe that this term evolves linearly with the mean concentration when we are close to the binodal ($\bar{\phi} \to 1$), so we can predict the theoretical dependence of the energy barrier and critical radius with respect to the concentration.

Experimentally we found that the critical nucleus only reaches the -1 value for concentrations above $\bar{\phi} = 0.9$ (although this quantity also depends on the value of the interface width). However, for this value we are still not in the sharp interface approximation. To get to the sharp interface limit we must consider concentrations above $\bar{\phi} = 0.985$, and in these cases consider very small interface widths. We need to decrease the interface width because the critical radius scales with δ. If we go too close to the binodal the critical radius may become so large that it may be larger than the final droplet radius. The way to avoid that is considering small interface widths. More precisely, an interface width of $\delta = 1.5 \cdot 10^{-3}$ was considered, and the mesh was discretized using $N = 2000$ nodes, to have enough resolution (the mesh size must be at least 3 times smaller than the interface width so as to resolve well the interfaces). There is a strong limitation in the possible values of the mean concentration. On one hand, we cannot go bellow the limit $\bar{\phi} = 0.985$, or otherwise the sharp interface approximation is not satisfied. However, for concentrations too close to $\bar{\phi} = 1$ the final droplet radius becomes smaller than the critical radius and the final state end up converging to the mixed state. Table 4 shows the results obtained for a range of values of the mean concentration for which the energy barrier was achieved. The rest of the values of the simulations are $m = 50$, $h = 10^{-7}$ and a constant interface energy of $\gamma = 10^{-2}$. To make the program more efficient, an improvement was added and the string was reparametrized every $n_s = 10$ steps. When the string is reparametrized every n_s steps the error is defined as the difference between the string after reparametrization and the string after the previous reparametrization step. To make the error consistent with the one we had been computing up to now the error is also normalized by n_s (since n_s iterations are performed between the previous string and the current one).

Mean concentration	Critical image	Energy barrier	Critical radius	Theoretical energy barrier	Theoretical critical radius
0.988	7	$2.96 \cdot 10^{-4}$	$1.07 \cdot 10^{-2}$	$3.33 \cdot 10^{-4}$	$1.06 \cdot 10^{-2}$
0.989	8	$3.24 \cdot 10^{-4}$	$1.18 \cdot 10^{-2}$	$3.63 \cdot 10^{-4}$	$1.16 \cdot 10^{-2}$
0.990	9	$3.56 \cdot 10^{-4}$	$1.26 \cdot 10^{-2}$	$3.99 \cdot 10^{-4}$	$1.27 \cdot 10^{-2}$
0.991	10	$3.99 \cdot 10^{-4}$	$1.33 \cdot 10^{-2}$	$4.42 \cdot 10^{-4}$	$1.41 \cdot 10^{-2}$
0.992	13	$4.53 \cdot 10^{-4}$	$1.63 \cdot 10^{-2}$	$4.97 \cdot 10^{-4}$	$1.58 \cdot 10^{-2}$
0.993	16	$5.27 \cdot 10^{-4}$	$1.87 \cdot 10^{-2}$	$5.67 \cdot 10^{-4}$	$1.80 \cdot 10^{-2}$

Table 4: Energy barrier and critical nucleus radius for different values of the mean concentration.

In Table 4 the critical radius was obtained by interpolating the critical nucleus profile to the radial value for which the order parameter is 0. The value of the critical image is the image on the string corresponding

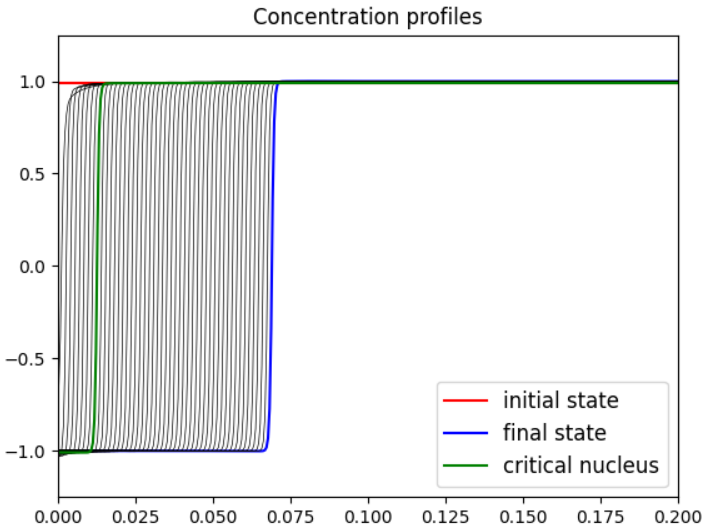

Figure 13: Final string profile for a mean concentration of $\bar{\phi} = 0.99$. The r axis is restricted to $r \in (0, 0.2)$ for a higher resolution.

to the critical state, where a value of 0 indicates the initial state and a value of $m - 1$ corresponds to the final state. Fig. 13 shows the final string profile for a mean concentration of $\bar{\phi} = 0.9$, restricted to the interval $r \in (0, 0.2)$ for a higher resolution.

Observe in the first place that both numerical and theoretical values increase when the mean concentration does, as expected (both values would diverge for $\bar{\phi} \to 1$). Moreover, the numerical values are very close to the theoretical ones, especially for the critical radius. Theoretical results are slightly larger than the numerical ones for energy barriers, and a bit smaller for critical radii. This can be related to the definition of the chemical potential, as we commented before. However, there are some factors which may contribute to these discrepancies.

The first one is that the definition we took when relating the interface energy to the model parameters (see Section 4.1.3) assumed that we had a planar interface separating two bulk regions. However, this is not the situation we have here, since our interfaces are curved. Hence, the real value of the interface energy is slightly different from the one we used as input in our model.

The second source of error is that we are computing the energy barrier as the difference in energy over the whole domain, while classical nucleation theory only considers the energy variation caused by the creation of the droplet. Hence, there is an extra energy term which is added to the energy barrier. Since the initial state and the critical state have roughly the same value of the order parameter outside the nucleus, the energy coming from the surrounding bulk phase should cancel in these two states. This is especially relevant when the critical state is close to the initial one, so in these cases the energy barrier from simulations fits better the theoretical one. This source of error, however, is probably irrelevant because of the high values of $\bar{\phi}$ we are considering.

Related to the previous comment, we can also have problems because we are considering Neumann boundary conditions. Classical nucleation theory assumes infinite domains, so the concentration outside the droplet does not change. Moreover, in principle the droplet should be able to increase indefinitely, since the growth of the nucleus (once reached the critical nucleus) reduces the free energy. However, in our system

the maximum droplet size is fixed by the size of the domain and the total concentration of the nucleating component, something which classical nucleation theory does not take into account.

Finally, discrepancies can also be caused by numerical issues. The most relevant one is that m is not big enough to give the appropriate value of the critical radius and energy barrier (this is discussed in more detail in section 4.4.2). It can also be caused by the fact that we considered too few spatial nodes.

We are also interested in measuring the dependence of the numerical energy barrier and the numerical critical radius with respect to the mean concentration, and observe whether the relation is the same as in classical nucleation theory. We assume that the relation in both cases is of the form $\Delta G^* = K_1(1-\bar{\phi})^{a_1}$ and $r^* = K_2(1-\bar{\phi})^{a_2}$, where K_1, K_2, a_1 and a_2 are constants to be determined (we actually mostly care for the values of a_1 and a_2, since K_1 and K_2 are simply two multiplicative factors). The way to determine these constants is via a log-log plot. If we plot the logarithm of the energy barrier and critical radius with respect to $(1-\bar{\phi})$ we obtain two straight lines, and the slope of these lines are the parameters a_1 and a_2.

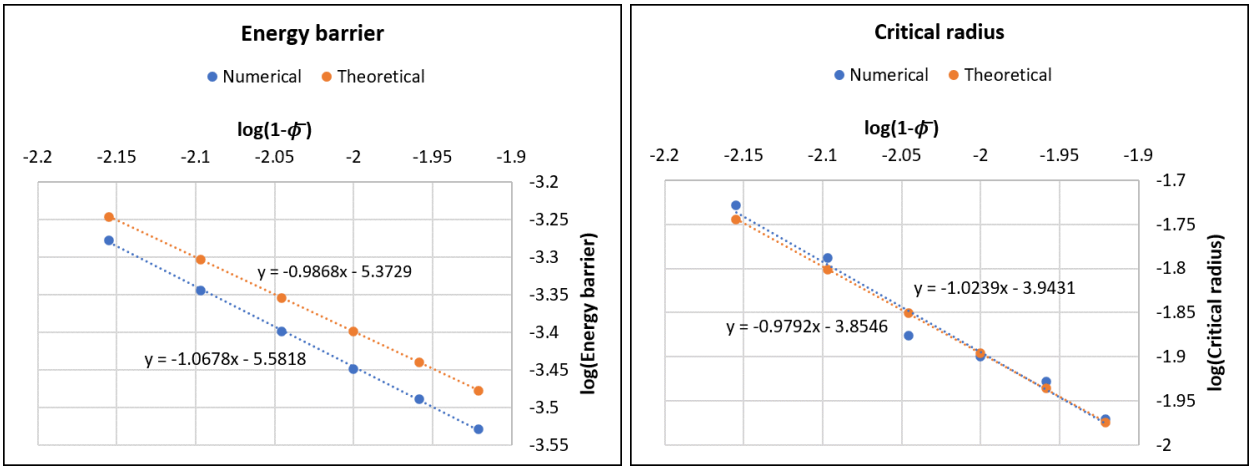

Figure 14: Energy barrier and critical radius comparison between numerical results and theoretical results for several values of the mean concentration.

Fig. 14 shows the comparison between numerical results (the ones obtained from simulations) and theoretical results, computed using classical nucleation theory relations. The numerical energy barrier log-log curve has a slope of $a_1 = -1.0678 \approx -1$, while the theoretical energy barrier goes roughly as $(1-\bar{\phi})^{-1}$, as expected. The critical radius has a slope of $a_2 = -1.0239 \approx -1$, while the theoretical one goes roughly as $(1-\bar{\phi})^{-1}$, as expected. Hence, the numerical results match the theoretical results perfectly. The small mismatches in the slopes of the theoretical curves from the predicted ones (-1 in both cases) are due to the fact that the exact dependence is not $(1-\bar{\phi})^{-1}$ in both cases, since there are higher order terms we have neglected.

It is interesting to note that the same results are obtained even if we are not in the sharp interface limit. A similar study can be performed for mean concentrations ranging from 0.92 to 0.96, for instance, and for larger interface widths ($\delta = 0.02$, around ten time larger). In this case critical nuclei still reach the value -1 near $r = 0$, although the values obtained for the critical radii are in the same order of magnitude as the interface width. Table 5 shows the results obtained with the following parameters: $N = 200$, $m = 50$, $\delta = 0.02$, $\gamma = \delta/3$, $h = 10^{-5}$ and $tol = 10^{-8}$.

We plot these values on a log-log plot in Fig. 15 (in the right plot, the equation $y = -0.9092x - 2.626$ corresponds to the theoretical values, and the equation $y = -1.0867x - 2.8521$ corresponds to the numerical

Mean concentration	Critical image	Energy barrier	Critical radius	Theoretical energy barrier	Theoretical critical radius
0.920	6	$4.16 \cdot 10^{-4}$	$2.25 \cdot 10^{-2}$	$4.94 \cdot 10^{-4}$	$2.36 \cdot 10^{-2}$
0.925	7	$4.47 \cdot 10^{-4}$	$2.51 \cdot 10^{-2}$	$5.23 \cdot 10^{-4}$	$2.50 \cdot 10^{-2}$
0.930	7	$4.82 \cdot 10^{-4}$	$2.42 \cdot 10^{-2}$	$5.56 \cdot 10^{-4}$	$2.65 \cdot 10^{-2}$
0.935	8	$5.22 \cdot 10^{-4}$	$2.64 \cdot 10^{-2}$	$5.94 \cdot 10^{-4}$	$2.83 \cdot 10^{-2}$
0.940	9	$5.70 \cdot 10^{-4}$	$2.83 \cdot 10^{-2}$	$6.38 \cdot 10^{-4}$	$3.05 \cdot 10^{-2}$
0.945	11	$6.25 \cdot 10^{-4}$	$3.29 \cdot 10^{-2}$	$6.91 \cdot 10^{-4}$	$3.30 \cdot 10^{-2}$
0.950	13	$6.92 \cdot 10^{-4}$	$3.65 \cdot 10^{-2}$	$7.54 \cdot 10^{-4}$	$3.60 \cdot 10^{-2}$
0.955	16	$7.78 \cdot 10^{-4}$	$4.17 \cdot 10^{-2}$	$8.31 \cdot 10^{-4}$	$3.97 \cdot 10^{-2}$
0.960	20	$8.92 \cdot 10^{-4}$	$4.73 \cdot 10^{-2}$	$9.28 \cdot 10^{-4}$	$4.43 \cdot 10^{-2}$

Table 5: Energy barrier and critical nucleus radius for different values of the mean concentration.

values). We obtain a very similar behaviour as in the sharp interface limit, although the values of the critical radius have a lot of deviation from the desired behaviour (in Fig. 15, the points at the end of the line deviate significantly from the trend line). However, this is not weird, since we are no longer in the sharp interface limit. What's more, the theoretical values only satisfy that they evolve linearly with respect to $1/(1-\bar{\phi})$ when we are very close to the binodal, but this is no longer the case. That is why even the theoretical values show a slope slightly smaller than -1.

This result is interesting because it states that there is no need to get to the sharp interface limit to get the correct dependence with respect to the concentration. However, when checking the validity of the model in three dimensions, we will still go to the sharp interface limit to assure that this behaviour is general.

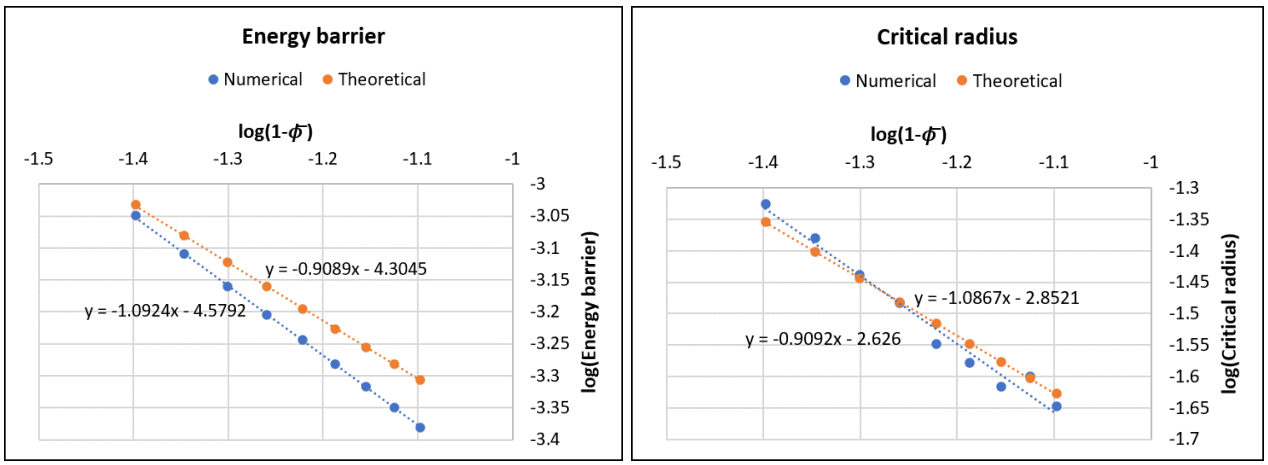

Figure 15: Energy barrier and critical radius comparison between numerical results and theoretical results for several values of the mean concentration.

Finally, simulations showed an interesting aspect of the final string. Fig. 16 shows the value of the order parameter at the center of the nucleus ($r = 0$) for each image on the sting and the value of the nucleus radius. The general behaviour of the nucleus consists on two steps: the nucleus enriches until it reaches the minimum value (-1), keeping its size approximately constant, and then it grows. It is also interesting to notice that the radius of the droplet increases linearly. However, a more accurate view on the concentration profiles along the string shows two things: the final concentration at the center of the nucleus is slightly lower than -1, and the intermediate images on the string reach a value near $r = 0$ lower than the final state, and they end up slightly increasing. This is due to the Gibbs-Thomson effect. This phenomenon is present

when curved interfaces are present (that is why this did not happen in one dimension). It consists on a variation in the chemical potential or vapor pressure when curved interfaces are considered. The positive interface energy provokes that surfaces with high curvature are less favorable, and these droplets show an increased vapor pressure [39]. In our model, this translates to a change in the equilibrium concentration profile, making it reach a smaller value than it would have otherwise.

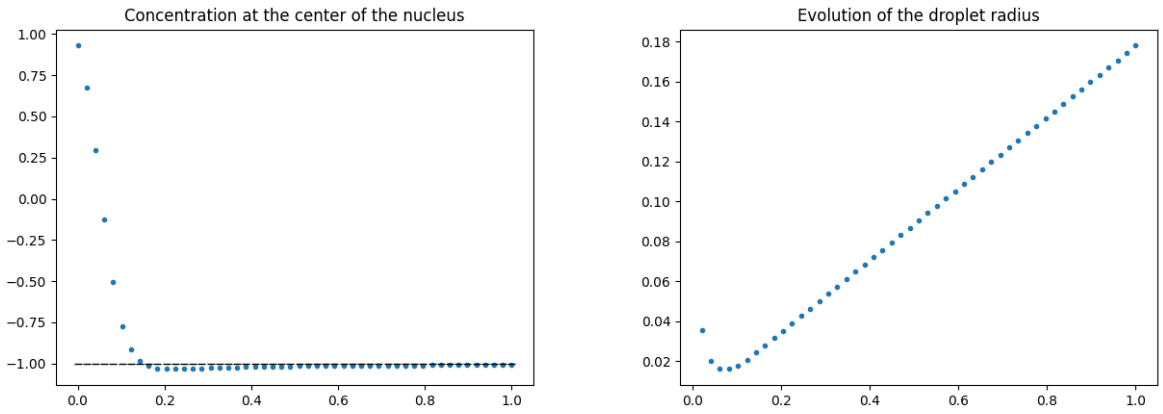

Figure 16: Concentration at the center of the nucleus and droplet radius for $\bar{\phi} = 0.93$.

4.4 Two dimensional case: Cartesian coordinates

The following step is to simulate the two dimensional case in cartesian coordinates. The two spatial directions have to be taken into account, so the problem becomes rather more complex. There are two goals in this case. The first one is to check whether the radial approximation considered in the previous section was correct or not, comparing the results obtained in each case. The second one is that when we study ternary mixtures or mixtures with more than three phases the cylindrical symmetry is broken, so the previous approximation can not be considered (this is discussed in detail in Section 5).

4.4.1 Numerical implementation

First of all we recover the Cahn-Hilliard equation in two dimensions:

$$\frac{\partial \phi}{\partial t} = \Delta \left(-W^2 \Delta \phi + A(\phi^3 - \phi) \right) \tag{59}$$

In this case, our domain will be the square $[0,1] \times [0,1]$, and we will consider circular droplets forming at the center of the square. We discretize the domain in $N \times N$ nodes. This poses a great difficulty, since we have a total of N^2 nodes, so the program will be computationally much more exprensive.

The expression of the Laplacian will be different from the one in polar coordinates. In cartesian coordinates, the general expression for the Laplacian of a function ϕ is $\Delta\phi = \frac{\partial^2 f}{\partial x^2} + \frac{\partial^2 \phi}{\partial y^2}$, which after discretization becomes:

$$\Delta\phi_{i,j} = \frac{\phi_{i+1,j} + \phi_{i-1,j} + \phi_{i,j+1} + \phi_{i,j-1} - 4\phi_{i,j}}{(dx)^2} \tag{60}$$

We considered $\phi_{i,j}$ to be the value of the function at node (i,j), where $i,j \in \{0,1,...,N-1\}$ and $dx = 1/N$. The matrix notation in this case is more complicated, since we have the function discretized on a rectangular grid, so the values are discretized using two indices instead of one (we have a matrix instead of a vector). The way to solve it is to rewrite the discretized function $\phi_{i,j}$ as a vector of N^2 nodes, with the following relation: $\phi_{i,j} = \phi_{i \cdot N+j} = \phi_k$, where $k \in \{0,...,N^2-1\}$. With the previous notation we can write the Laplacian operator in matricial form. More precisely, the matrix of the Laplacian will have size $(N)^2 \times (N)^2 = (N)^4$.

The previous notation poses a serious problem of implementation, since, to resolve a mesh of size $N = 100$ we need to store a matrix of size $N^4 = 10^8$, which is extremely large. Moreover, if we use the IMEX method, we have to invert this matrix, something impossible in practice. Hence, an alternative must be used.

The best way to avoid computing such matrices is working in the Fourier space [37]. All derivatives and Laplacian operators turn into multiplications, so there is no need to store any matrix nor to solve any linear system. Moreover, the Fast Fourier Transform (FFT) is a method which allows us to change from real space to Fourier space efficiently (it has complexity $O(NlogN)$). The only problem comes from the fact that Fourier space only allows to treat periodic boundary conditions, in contrast to Neumann boundary conditions considered in the previous section. However, since the concentration takes a constant value of 1 near the edge in all cases, no important differences should arise.

Recall in the first place that the Fourier transform of a function $f(x,y)$ in two dimensions is defined as:

$$\mathcal{F}(f)(k_x,k_y) = \int_{-\infty}^{+\infty}\int_{-\infty}^{+\infty} f(x,y)e^{-2\pi i(k_x x + k_y y)}dxdy \tag{61}$$

where k_x and k_y are the spatial frequencies and i is the imaginary unit. One of the main properties of the Fourier transform is that derivatives turn into multiplications: $\mathcal{F}(\frac{\partial f}{\partial x}) = -2\pi i k_x \mathcal{F}(f)$. The Laplacian operator satisfies: $\mathcal{F}(\Delta f) = -4\pi^2 k^2 \mathcal{F}(f)$, where $k^2 = k_x^2 + k_y^2$. For simplicity, from now on we will write: $\hat{f} = \mathcal{F}(f)$, $\hat{k_x} = 2\pi k_x$, $\hat{k_y} = 2\pi k_y$ and $\hat{k} = 2\pi k$.

The Cahn-Hilliard equation in the Fourier space is then:

$$\frac{\partial \hat{\phi}}{\partial t} = -\hat{k}^2\left(W^2\hat{k}^2\hat{\phi} + \hat{\mu}_0\right) \tag{62}$$

where $\hat{\mu}_0 = \mathcal{F}(A(\phi^3 - \phi))$ is the Fourier transform of the chemical potential. If we use an IMEX method we can solve this equation in an equivalent way as in the previous section, but instead of inverting matrices we divide by a constant term:

$$\hat{\phi}^{n+1} = \frac{\hat{\phi}^n - h\hat{\mu}_0^n}{1 + hW^2\hat{k}^2} \tag{63}$$

The general algorithm will be the following:

1. The chemical potential, μ^n, is computed in the real space.
2. The chemical potential is transformed to the Fourier space via the FFT, $\hat{\mu}^n$. The order parameter is computed in the Fourier space as well, $\hat{\phi}^n$.
3. The time evolution is performed following Eq. 63 to obtain $\hat{\phi}^{n+1}$.

4. The value of the vector solution is computed in real space via the Inverse Fast Fourier Transform (IFFT), to obtain ϕ^{n+1}.

5. Every n_s iterations, the string is reparametrized.

Observe that we have to convert the string back and forth because the chemical potential has to be computed in the real space from the real value of the string. Moreover, the string method has to reparametrize the string in real space.

Since the total number of nodes is N^2 we still have some computational limitations when choosing the value of N, so we may not be able to take the same values for N as in the polar case. As for the rest, the relation between model parameters and physical constants is the same in both cases.

Finally, the initial string considered in simulations corresponds again to the formation and growth of the nucleus. The initial state is a constant concentration profile, while the final state corresponds to a droplet at the center of the domain ($\phi = -1$ inside the droplet and $\phi = 1$ outside). The intermediate images along the string are circular droplets with increasing radii, where $\phi = -1$ inside the droplet, and the value of ϕ outside is determined imposing that the mean concentration is conserved. All interfaces are initialized as sharp, and the string method smooths them.

4.4.2 Simulations and results

Since our goal is to compare if we obtain the same results in the polar case and in the cartesian case, we considered the same values for the interface energy and interface width as in the previous case. We are especially interested in checking if the simplified polar coordinates give the same results as the cartesian ones for large values of the mean concentration, since in these cases we know that simulations reproduce correctly classical nucleation theory.

Another important issue is to check if the droplet formed has circular symmetry. We do not only demand the final droplet to have circular symmetry, but all the intermediate images along the string as well. In particular we are interested in checking that the critical state has circular symmetry. Observe that in the way that we implement the method, since our domain is rectangular, the intermediate droplets along the string needn't be circular. The only thing we can say a priori is that they will be invariant under rotations of 90° (there are four directions in the domain which are equivalent, so all intermediate states should show this symmetry of rotation).

Table 6 shows the results of simulating the nucleation of a circular droplet in our square domain. The spatial coordinates were discretized using $N = 150$ nodes (minimum number to resolve interface widths of the order of $\delta = 0.02$, as in the polar case). The rest of the parameters were: $m = 50$, $\gamma = \delta/3$, $h = 10^{-5}$ and a tolerance of $tol = 10^{-8}$.

Fig. 17 shows the concentration for the initial, critical and final state for a mean concentration of $\bar{\phi} = 0.93$. We observe that the critical state has circular shape, an assumption that we did in the polar case. A more thorough examination shows that all intermediate states are circular as well, as expected.

Observe that the values are quite close to the ones in the polar case, especially for the energy barriers. A possible cause of the discrepancies is due to the Neumann boundary conditions and the effect they have in the computation of the energy barrier. Moreover, in the cartesian case we considered periodic boundary conditions, so this effect is different in the cartesian and the polar case.

Another source of error is the fact that m is possibly not large enough to resolve the critical radii with precision. In fact, if we compute the radius of the droplet for the previous and following images of the critical

Mean concentration	Critical image	Energy barrier	Critical radius	Energy barrier polar	Critical radius polar
0.920	6	$4.13 \cdot 10^{-4}$	$2.64 \cdot 10^{-2}$	$4.16 \cdot 10^{-4}$	$2.25 \cdot 10^{-2}$
0.925	7	$4.45 \cdot 10^{-4}$	$2.77 \cdot 10^{-2}$	$4.47 \cdot 10^{-4}$	$2.51 \cdot 10^{-2}$
0.930	9	$4.84 \cdot 10^{-4}$	$3.11 \cdot 10^{-2}$	$4.82 \cdot 10^{-4}$	$2.42 \cdot 10^{-2}$
0.935	11	$5.28 \cdot 10^{-4}$	$3.33 \cdot 10^{-2}$	$5.22 \cdot 10^{-4}$	$2.64 \cdot 10^{-2}$
0.940	14	$5.83 \cdot 10^{-4}$	$3.62 \cdot 10^{-2}$	$5.70 \cdot 10^{-4}$	$2.83 \cdot 10^{-2}$
0.945	19	$6.51 \cdot 10^{-4}$	$4.04 \cdot 10^{-2}$	$6.25 \cdot 10^{-4}$	$3.29 \cdot 10^{-2}$

Table 6: Energy barrier and critical nucleus radius for different values of the mean concentration, compared to the values obtained in the polar case.

state we see that the value of the radius changes considerably. For example, for $\bar{\phi} = 0.92$, the droplet radius at image 5 is $r = 2.34 \cdot 10^{-2}$ and the radius at image 7 is $r = 2.91 \cdot 10^{-2}$. Hence, the real critical radius lies within the interval $r \in (2.34 \cdot 10^{-2}, 2.91 \cdot 10^{-2})$. If the same test is done in polar coordinates we get that the droplet lies within the interval $r \in (1.9 \cdot 10^{-2}, 2.63 \cdot 10^{-2})$. Observe that both intervals are quite large and they superpose, which means that the value of the critical radius does not have a lot of precision, and that perhaps with more accuracy the values would actually match. One way to solve this issue would be to increase the value of m, but this is quite complicated in the cartesian case, since the program is already quite slow. Another way to determine the critical radius would be to interpolate its value (for instance using splines). Fig. 18 shows the radial profiles both in cartesian coordinates and in polar coordinates. We see that the profiles are very close to each other, although the cartesian case has a slightly larger radius.

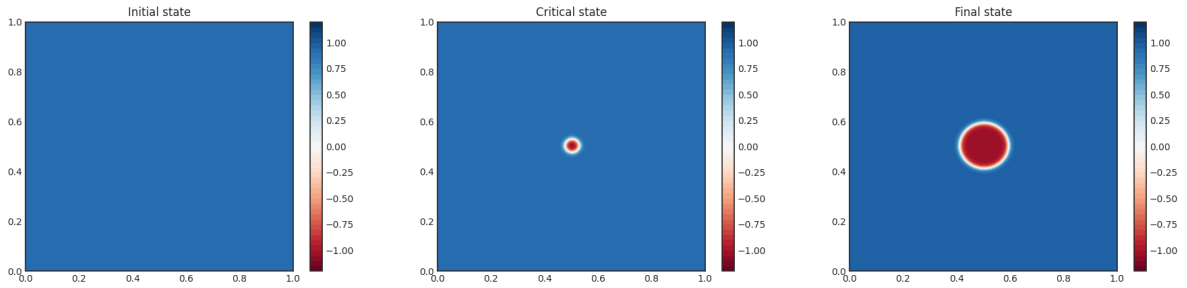

Figure 17: Concentration profiles for a droplet in 2d cartesian coordinates. Left: Initial state. Center: Critical state. Right: Final state.

In the cartesian case we could only increase the mean concentration up to a value of $\bar{\phi} = 0.945$, in contrast to the polar case, where we could consider mean concentrations of $\bar{\phi} = 0.96$ for the same value of the interface width. This happens because for larger concentrations the final droplet size is smaller than the critical nucleus, so the final state at the begging of the string method tends to dilute again, returning to the mixed state, instead of converging to the separated state. This can be analyzed in the following way: for a given value of the mean concentration, the radius of the final droplet is fixed and has the following expression: $r = \sqrt{\frac{1-\bar{\phi}}{2\pi}}$. For a value of the mean concentration of $\bar{\phi} = 0.95$ we already have $r = 8.92 \cdot 10^{-2}$, which is quite close to the critical radius. For a value of $\bar{\phi} = 0.96$, $r = 7.98 \cdot 10^{-2}$, and the theoretical critical radius is $r^* = 4.04 \cdot 10^{-2}$. However, as we can see in Table 6, the critical radius end up being larger in simulations, so most likely the final droplet has a smaller radius than the critical one.

Observe that the domain is different in polar coordinates than in cartesian coordinates. In polar co-

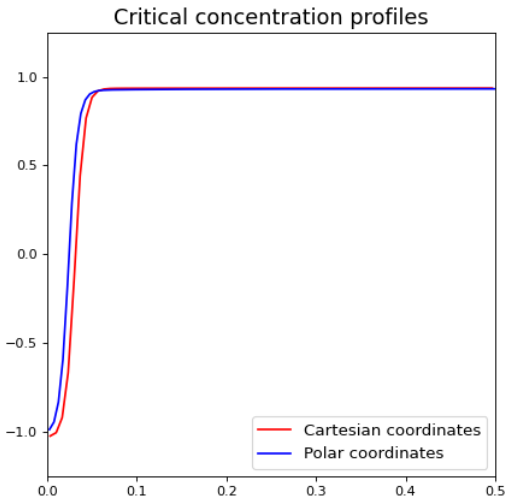

Figure 18: Critical profiles for cartesian and polar coordinates, $\bar{\phi} = 0.93$.

ordinates it is a circular domain of radius 1, while in cartesian coordinates it is a rectangular domain of size 1×1. This does not affect the value of the critical radius, which only depends on the value of the mean concentration and the interface width. The energy barrier is only slightly affected by this, since the difference in the size of the domain affects the term of the free energy coming from the bulk surrounding phase. However, as we commented before, this effect is very small when computing the energy barrier, since the initial state and the critical state have roughly the same concentration outside the droplet.

A more exhaustive analysis leads us to the relation between the free energy in polar and cartesian coordinates. For images close to the mixed state, the total energy in the cartesian case will be smaller than the one in polar coordinates by a factor of π, which is the size of the domain. However, for states close to the separated state, this factor will be of the order of $\sqrt{\pi}$, since the only term which contributes to the energy is the interface, and the length of the interface evolves linearly with the radius of the droplet (and, for a fixed mean concentration, the radius of the droplet in cartesian coordinates is smaller than the radius of the droplet in polar coordinates by a factor of $\sqrt{\pi}$).

These relations can be checked in Fig. 19. The initial state in cartesian coordinates has an energy of $4.563 \cdot 10^{-3}$, while the initial state in polar coordinates has an energy of $1.435 \cdot 10^{-2}$. The ratio between these two energies (the polar divided by the cartesian) is $3.145 \approx \pi$, as expected. For the final states, the cartesian state has an energy of $3.97 \cdot 10^{-3}$, while the polar final state has an energy of $7.341 \cdot 10^{-3}$. The ratio between these two energies is 1.849, while $\sqrt{\pi} \approx 1.772$. Hence, in both cases the results are consistent.

The final effect is that the energy curve in cartesian coordinates will look shifted form the one in polar coordinates, and hence the maximum of the curve will shift to the right as well. This is why the critical images along the string in the cartesian case are greater than the ones in the polar case.

The way to avoid having droplets with a size smaller than the critical size is to decrease the interface width. In that way the critical radii are reduced, since they scale with δ (see Eq. 4.3.2), and one can consider higher concentrations. However, in practice, this is very complicated to achieve, since the mesh cannot be discretized using much more nodes, and we are already considering the smallest possible value

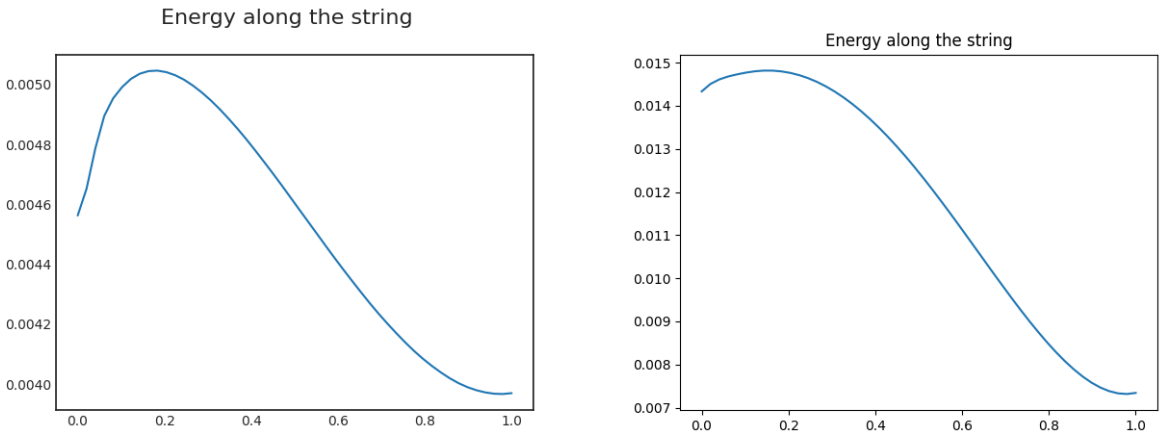

Figure 19: Energy along the string for a concentration of $\bar{\phi} = 0.93$. Left: cartesian coordinates. Right: polar coordinates.

for the interface width for a fixed value of N.

The conclusion is that the approximation of evolving simply the radial profile is correct, despite the differences in the energy barriers and critical nuclei obtained. It would also be interesting to consider more images along the string if possible, to obtain more accurate values, especially for the critical radius.

4.5 Three dimensional case: Spherical coordinates

The last case we consider for binary mixtures is the three dimensional case assuming spherical symmetry. This assumption is reasonable, since nuclei forming inside phases have roughly spherical shape. In this case, we simply consider the radial profiles to simplify the simulations. The general cartesian case can also be performed to compare results. However, due to the complexity of implementation, it is not considered in this thesis.

4.5.1 Numerical implementation

The only difference of the three dimensional spherical case with respect to the two dimensional polar case is the expression of the Laplacian. In spherical coordinates, the Laplacian of a function $\phi(r, \theta, \varphi)$ has the following expression (assuming that ϕ only depends on the radius, $\phi = \phi(r)$):

$$\Delta\phi = \frac{1}{r^2}\frac{\partial}{\partial r}\left(r^2\frac{\partial\phi}{\partial r}\right) + \frac{1}{r^2\sin\theta}\frac{\partial}{\partial\theta}\left(\sin\theta\frac{\partial\phi}{\partial\theta}\right) + \frac{1}{r^2\sin^2\theta}\frac{\partial^2\phi}{\partial\varphi^2} = \frac{1}{r^2}\frac{\partial}{\partial r}\left(r^2\frac{\partial\phi}{\partial r}\right) \tag{64}$$

Since we have the same problem for $r = 0$ as in polar coordinates, we consider our spatial nodes to range from $dr/2$ to $1 - dr/2$, where $dr = 1/N$. In this case, the discretized Laplacian at an interior node i is:

$$\Delta\phi_i = \frac{2}{r_i}\frac{\phi_{i+1} - \phi_{i-1}}{2dr} + \frac{\phi_{i+1} - 2\phi_i + \phi_{i-1}}{dr^2} \tag{65}$$

We get a very similar expression to the two dimensional case, except for a factor 2 in the first term. As for the boundary conditions, we consider Neumann boundary conditions both at $r = 0$ and $r = 1$. This translates into the creation of two fictitious nodes which satisfy: $\phi_0 = \phi_{-1}$ and $\phi_N = \phi_{N-1}$ (with these two nodes Eq. 65 can be used for all the nodes). We can write the Laplacian in matricial form:

$$L = N^2 \begin{pmatrix} -3 & 3 & 0 & 0 & \dots & 0 & 0 & 0 \\ 1/3 & -2 & 5/3 & 0 & \dots & 0 & 0 & 0 \\ 0 & 3/5 & -2 & 7/5 & \dots & 0 & 0 & 0 \\ \vdots & \vdots & \vdots & \vdots & \ddots & \vdots & \vdots & \vdots \\ 0 & 0 & 0 & 0 & \dots & \frac{3-2dr}{1-2dr} & -2 & \frac{1-2dr}{1-2dr} \\ 0 & 0 & 0 & 0 & \dots & 0 & \frac{2-3dr}{2-dr} & -\frac{2+3dr}{2-dr} \end{pmatrix} \tag{66}$$

Finally, the rest of the parameters of the model are defined in the same way as in the polar case. Moreover, the relation between model parameters and physical magnitudes is the same as in the one dimensional case and two dimensional case.

4.5.2 Simulations and results

The goal of the simulations is to check whether the phase field method reproduces correctly classical nucleation theory results or not. To do so, we have to get to the sharp interface limit and compare the relation between energy barriers and critical radii with the values given by their classical expressions. The expressions for the energy barrier and critical nucleus in spherical coordinates in classical nucleation theory are given in Section 4 (Eqs. 7 and 8). These two expressions have a term, ΔG_V, which has to be calculated from our parameters. In the same way as in the polar case, we compute it as the difference in chemical potential between the mixed state and the separated state (Eq. 58). From this expression, we can already deduce that, since the chemical potential will evolve linearly with $1/(1-\bar{\phi})$, the energy barrier will depend quadratically on this quantity and the critical radius will depend linearly on it.

As in the polar case, we have to reach very high values of the concentration and very small values of the interface width to reach the sharp interface limit. However, the values can be a bit smaller than in the polar case. More precisely, we considered mean concentrations ranging from $\bar{\phi} = 0.98$ to $\bar{\phi} = 0.99$. We performed the simulations using the IMEX method and reparametrizing the string every $n_s = 10$ steps. Table 7 shows the results for the energy barriers and the critical radii for the following parameters: $N = 1000$, $m = 50$, $\delta = 4 \cdot 10^{-3}$, $\gamma = 0.01$, $h = 10^{-5}$ and $tol = 2 \cdot 10^{-8}$.

Mean concentration	Critical image	Energy barrier	Critical radius	Theoretical energy barrier	Theoretical critical radius
0.980	8	$4.54 \cdot 10^{-5}$	$3.44 \cdot 10^{-2}$	$1.98 \cdot 10^{-4}$	$6.87 \cdot 10^{-2}$
0.981	8	$5.27 \cdot 10^{-5}$	$3.38 \cdot 10^{-2}$	$2.18 \cdot 10^{-4}$	$7.22 \cdot 10^{-2}$
0.982	9	$5.63 \cdot 10^{-5}$	$3.73 \cdot 10^{-2}$	$2.43 \cdot 10^{-4}$	$7.61 \cdot 10^{-2}$
0.983	9	$6.32 \cdot 10^{-5}$	$3.68 \cdot 10^{-2}$	$2.71 \cdot 10^{-4}$	$8.05 \cdot 10^{-2}$
0.984	10	$6.94 \cdot 10^{-5}$	$4.00 \cdot 10^{-2}$	$3.05 \cdot 10^{-4}$	$8.54 \cdot 10^{-2}$
0.985	11	$7.86 \cdot 10^{-5}$	$4.29 \cdot 10^{-2}$	$3.46 \cdot 10^{-4}$	$9.09 \cdot 10^{-2}$
0.986	13	$9.17 \cdot 10^{-5}$	$4.97 \cdot 10^{-2}$	$3.96 \cdot 10^{-4}$	$9.73 \cdot 10^{-2}$
0.987	14	$1.05 \cdot 10^{-4}$	$5.21 \cdot 10^{-2}$	$4.58 \cdot 10^{-4}$	$1.05 \cdot 10^{-1}$
0.988	16	$1.25 \cdot 10^{-4}$	$5.81 \cdot 10^{-2}$	$5.36 \cdot 10^{-4}$	$1.13 \cdot 10^{-1}$
0.989	17	$1.53 \cdot 10^{-4}$	$5.97 \cdot 10^{-2}$	$6.36 \cdot 10^{-4}$	$1.23 \cdot 10^{-1}$

Table 7: Energy barrier and critical nucleus radius for different values of the mean concentration.

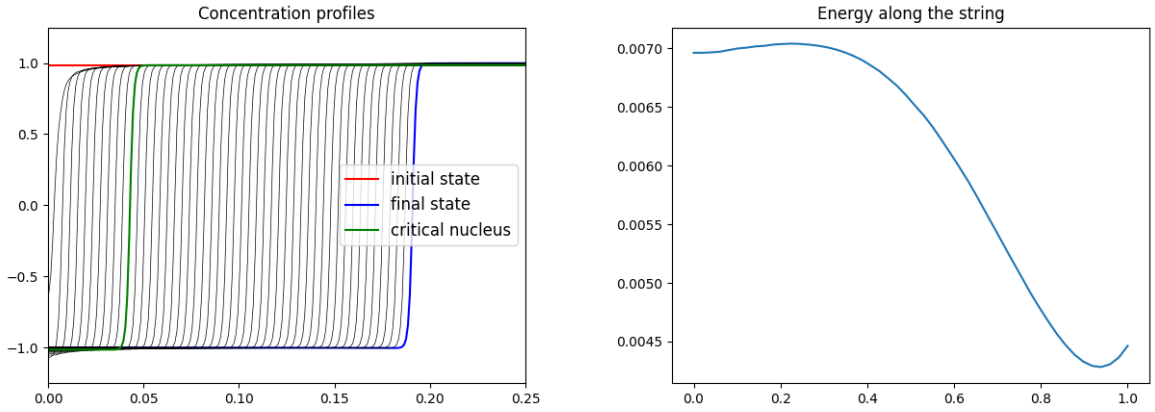

Figure 20: Concentration profiles and energy along the string

Fig. 20 shows the concentration profiles and energy along the string for a value of the mean concentration of $\bar{\phi} = 0.985$. Observe that the final state of the string has not converged to the correct solution, since that state should be the one with the lowest energy (the metastable state). This happens because convergence is very slow, and smaller tolerances should be considered for the final state to converge. Another option is to take as the final state the image on the string with the minimum energy, instead of the last image of the string. However, we do not care about the final state, since we only need to know the initial state and the critical one. The results we obtained for the energy barrier are already good enough to be compared to classical nucleation theory.

With respect to the comparison between numerical values, observe in the first place that both the energy barriers and critical radii increase when we get closer to the binodal, as we expected. However, in that case the numerical results do not directly match the theoretical ones. In particular, numerical energy barriers are roughly 4 times smaller than theoretical ones, and numerical critical radii are roughly 2 times smaller than the theoretical ones. The same reasons as in the two dimensional polar case can explain these mismatches (see Section 4.4.2).

On the one hand, is that the formula we derived for the interface energy in relation to the model parameters assumes that we have flat interfaces separating two phases. However, in that case we have curved surfaces, so the actual value of the interface width is different. Another possible explanation are the Neumann boundary conditions, which differ from the assumptions of classical nucleation theory, and the contribution in the computation of the energy of the surrounding phase. Finally, differences can be caused by numerical errors, or by considering too few images on the string.

Although all the previous comments can be responsible for the difference between theoretical values and numerical ones, none of them seem to explain the large factors that relate numerical values to theoretical ones. What is more surprising is that results in two dimensions match very well, but in three dimensions they don't. None of the previous arguments is restricted to the three dimensional case, all of them apply both to two dimensions and three dimensions. Some of them may have a larger impact in three dimensions than in two dimensions, but it is unlikely that they are responsible for this large deviation between theory and simulations. A more exhaustive analysis should be performed to determine what is the source of these errors.

To compare numerical results to theoretical results, in the same way that we did in the polar case, we

assume that the relation both for the energy barrier and the critical radius is of the form: $\Delta G^* = K_1(1-\bar{\phi})^{a_1}$ and $r^* = K_2(1-\bar{\phi})^{a_2}$, where K_1, K_2, a_1 and a_2 are constants to be determined . The way to determine these constants is via a log-log plot.

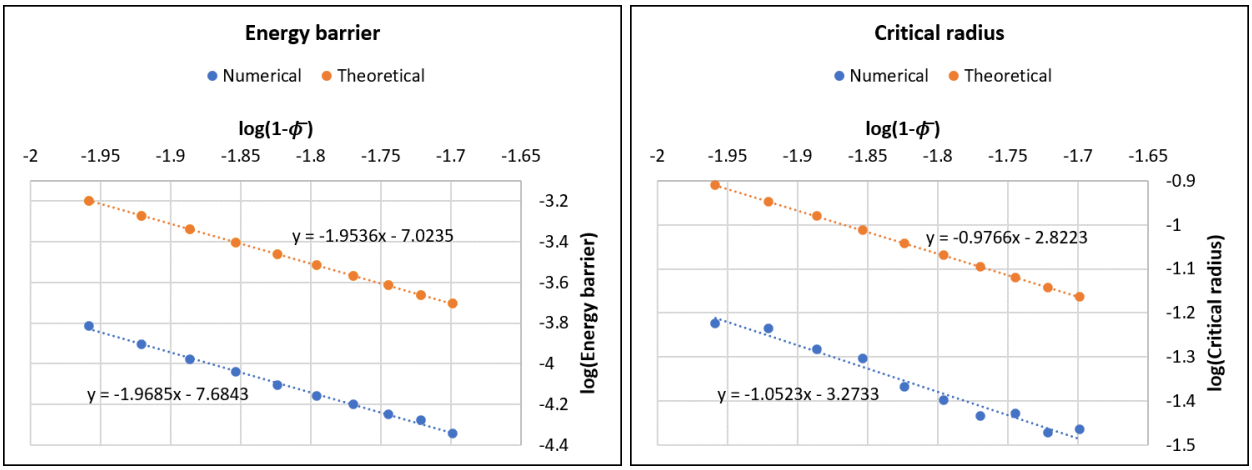

Figure 21: Energy barrier and critical radius comparison between numerical results and theoretical results for several values of the mean concentration.

Fig. 21 shows the log-log plots for the energy barrier and critical radius. From these plots we can calculate the slope of the trend line, obtained from the data using least squares approximation. We get the following values for our parameters: $a_1 = -1.9685 \approx -2$ and $a_2 = -1.0523 \approx -1$, which are in agreement with the theoretical values. Especially for the critical radius we see that there are some oscillations with respect to the ideal linear behaviour. However, this happens for the lowest values of mean concentrations, which may mean that the critical radius size is still comparable to the interface width, or that more images on the string should be considered to determine the value of the critical radius with more precision.

In a similar way as in the polar case, we are able to reproduce the correct dependence even if we are not in the sharp interface limit. We can consider smaller values of the mean concentration and still get the linear dependence in the critical radius and quadratic dependence in the energy barrier. The following table shows some the values obtained for these magnitudes when we consider mean concentrations ranging from $\bar{\phi} = 0.85$ to $\bar{\phi} = 0.93$. The rest of the parameters are: $N = 100$, $m = 50$, $\delta = 0.05$, $\gamma = \delta/3$, $h = 10^{-5}$ and different values for the tolerance (we found that we had to decrease the value of the tolerance for higher values of $\bar{\phi}$ to achieve convergence).

Mean concentration	Critical image	Energy barrier	Critical radius	Theoretical energy barrier	Theoretical critical radius
0.85	8	$2.09 \cdot 10^{-4}$	$6.56 \cdot 10^{-2}$	$1.39 \cdot 10^{-3}$	$1.41 \cdot 10^{-1}$
0.86	8	$2.47 \cdot 10^{-4}$	$6.34 \cdot 10^{-2}$	$1.55 \cdot 10^{-3}$	$1.49 \cdot 10^{-1}$
0.87	9	$2.94 \cdot 10^{-4}$	$6.90 \cdot 10^{-2}$	$1.73 \cdot 10^{-3}$	$1.58 \cdot 10^{-1}$
0.88	10	$3.51 \cdot 10^{-4}$	$7.38 \cdot 10^{-2}$	$1.97 \cdot 10^{-3}$	$1.68 \cdot 10^{-1}$
0.89	12	$4.25 \cdot 10^{-4}$	$8.54 \cdot 10^{-2}$	$2.27 \cdot 10^{-3}$	$1.80 \cdot 10^{-1}$
0.90	13	$5.20 \cdot 10^{-4}$	$8.83 \cdot 10^{-2}$	$2.65 \cdot 10^{-3}$	$1.95 \cdot 10^{-1}$
0.91	16	$6.53 \cdot 10^{-4}$	$1.03 \cdot 10^{-1}$	$3.17 \cdot 10^{-3}$	$2.13 \cdot 10^{-1}$
0.92	19	$8.39 \cdot 10^{-4}$	$1.15 \cdot 10^{-1}$	$3.88 \cdot 10^{-3}$	$2.36 \cdot 10^{-1}$
0.93	25	$1.13 \cdot 10^{-3}$	$1.38 \cdot 10^{-1}$	$4.91 \cdot 10^{-3}$	$2.65 \cdot 10^{-1}$

Table 8: Energy barrier and critical nucleus radius for different values of the mean concentration.

Fig. 22 shows the values of the energy barriers and critical radii with respect to $1-\bar{\phi}$ in a log-log plot. We observe that the energy barrier evolves roughly as $(1-\bar{\phi})^{-2}$ and the critical radius as $(1-\bar{\phi})^{-1}$, as expected. The values of the critical radii are quite disperse, especially for low concentrations. Besides not being in the sharp interface limit, this happens because for low values of the mean concentration the critical nucleus does not reach the value -1 near $r=0$. In that case the phase field model is no longer useful to study classical nucleation results because the assumptions in classical nucleation theory are no longer valid. As in the two dimensional case, since we are not close to the binodal any more even the theoretical values deviate from the desired behaviour (slope -2 for the energy barrier and slope -1 for the critical radius).

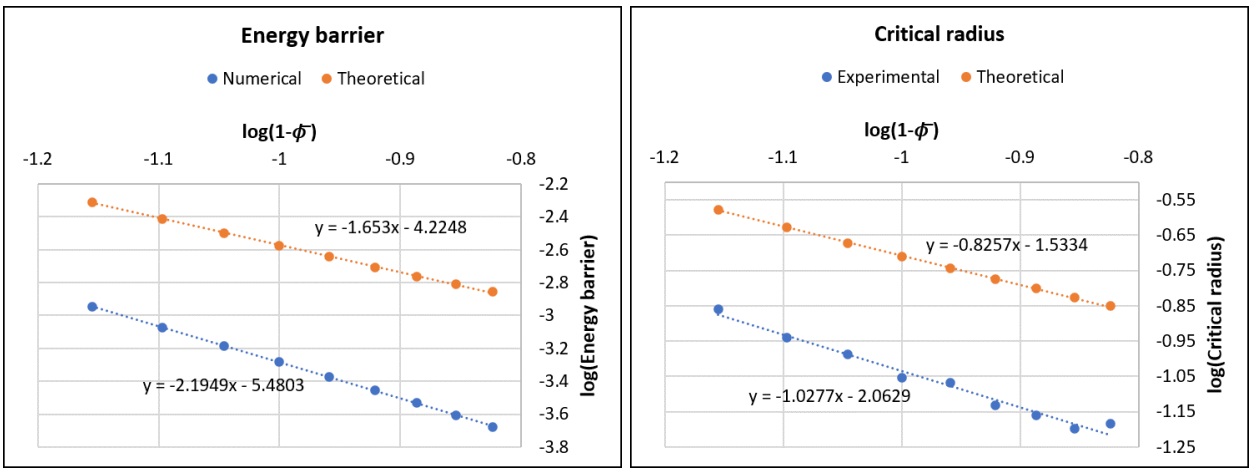

Figure 22: Energy barrier and critical radius comparison between numerical results and theoretical results for several values of the mean concentration.

The values of the critical radii have been compared directly because the interface width was the same in all simulations. However, if different interface widths are considered, the profiles of the critical nuclei changes. The value of the critical radius should scale with δ. One way to check that this is true is running the same simulation with different values of the interface width and scaling the critical profiles obtained with respect to the interface width. We call **reduced critical radius** the critical radius divided by the interface width. We should observe that the reduced critical radius does not depend on the value of the interface width.

To check this, we run some simulations under the same conditions except for the value of δ. Table 9 shows the results obtained for the following parameters: $N=100$, $m=50$, $\gamma=10^{-2}$, $h=10^{-5}$ and $\bar{\phi}=0.85$. For these conditions, the minimum possible value for the interface width was $\delta=0.03$ (it has to be at least $3dx$, where $dx=1/N=0.01$), and the maximum possible value is determined by convergence issues. We considered $\delta\in(0.3.0.7)$.

The results agree with the predictions: the reduced critical radii have roughly a constant value. Not only that, but Fig. 23 shows the critical nucleus profiles for the reduced radial component, that is, r/δ. We only plot the values near the center of the critical nucleus (r=0). We see that all profiles match very well. The worst case happens for $\delta=0.03$, which the smallest value. This is not rare, since the value of the interface width in that case is the minimum possible value, so the program may not be able to resolve properly this case.

There is one last test that can be performed for binary mixtures. The string method does not require to reparametrize the string at each iteration, it can be reparametrized every n_s iterations. The advantage of reparametrizing at each step is that we get more precise results, and numerical noise has a less relevant

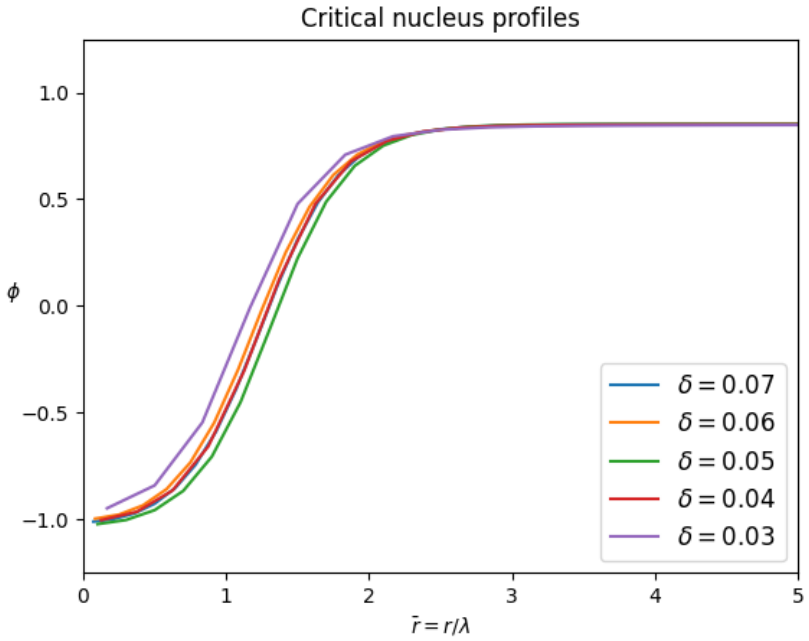

Figure 23: Critical nucleus profiles for reduced radial component, for $\bar{\phi} = 0.85$.

Interface width	Critical image	Critical radius	Reduced critical radius
0.07	11	$8.79 \cdot 10^{-2}$	1.26
0.06	9	$7.30 \cdot 10^{-2}$	1.22
0.05	8	$6.59 \cdot 10^{-2}$	1.32
0.04	6	$5.03 \cdot 10^{-2}$	1.26
0.03	4	$3.43 \cdot 10^{-2}$	1.14

Table 9: Energy barrier and critical nucleus radius for different values of the mean concentration.

effect. However, taking a large value of n_s makes the program faster, which is an issue we are concerned about, especially for cartesian coordinates, where the program is much slower. To find the most efficient value of n_s we performed 10000 iterations of the string method for several values of n_s and computed the total CPU time the program takes to run. We computed the values for the energy barrier and critical radius, as well as the error after the last iteration (the error is computed in the following way: the two last reparametrized strings before convergence are considered, and the norm of the difference is computed, divided by N, m and n_s to get results which can be directly compared). Table 10 shows the results for the following parameters: $\bar{\phi} = 0.85$, $N = 100$, $m = 50$, $\delta = 0.05$, $\gamma = 0.01$ and $h = 10^{-5}$.

If we consider the total CPU time of execution, the only conclusion we can derive is that for small values of n_s (5 or less) the time is significantly larger than in the rest of the cases. Since there a lot of fluctuations on the exact time of execution (many tests were performed for each case, since the time of execution under the same conditions can change), we see that for a value of $n_s = 10$ the fluctuations are already larger than the actual difference in time between different values of n_s, and hence there is no need to increase the value of n_s in terms of speed of the program. If we consider the values of the energy barriers and critical radii, we

n_s	Final error	Total CPU time (seconds)	Critical image	Energy barrier	Critical radius
1	$1.24 \cdot 10^{-8}$	29.87	8	$1.25 \cdot 10^{-4}$	$6.61 \cdot 10^{-2}$
2	$1.24 \cdot 10^{-8}$	21.84	8	$1.25 \cdot 10^{-4}$	$6.61 \cdot 10^{-2}$
5	$1.24 \cdot 10^{-8}$	14.44	8	$1.25 \cdot 10^{-4}$	$6.61 \cdot 10^{-2}$
10	$1.24 \cdot 10^{-8}$	12.61	8	$1.25 \cdot 10^{-4}$	$6.61 \cdot 10^{-2}$
20	$1.24 \cdot 10^{-8}$	12.24	8	$1.25 \cdot 10^{-4}$	$6.61 \cdot 10^{-2}$
50	$1.24 \cdot 10^{-8}$	11.93	8	$1.25 \cdot 10^{-4}$	$6.60 \cdot 10^{-2}$
100	$1.25 \cdot 10^{-8}$	12.00	8	$1.25 \cdot 10^{-4}$	$6.59 \cdot 10^{-2}$
200	$1.25 \cdot 10^{-8}$	10.76	8	$1.25 \cdot 10^{-4}$	$6.59 \cdot 10^{-2}$
500	$1.25 \cdot 10^{-8}$	12.55	8	$1.25 \cdot 10^{-4}$	$6.60 \cdot 10^{-2}$
1000	$1.26 \cdot 10^{-8}$	16.69	8	$1.25 \cdot 10^{-4}$	$6.63 \cdot 10^{-2}$
2000	$1.34 \cdot 10^{-8}$	14.58	7	$1.27 \cdot 10^{-4}$	$5.94 \cdot 10^{-2}$
5000	$1.04 \cdot 10^{-7}$	12.39	6	$1.27 \cdot 10^{-4}$	$6.10 \cdot 10^{-2}$
10000	$1.89 \cdot 10^{-7}$	11.45	5	$2.97 \cdot 10^{-4}$	$1.01 \cdot 10^{-1}$

Table 10: Time of execution, energy barrier and critical nucleus for different values of n_s.

see that there are no significant discrepancies until the value $n_s = 2000$ is considered. For values larger than this one the program does not converge properly and more iterations would be required. Hence in Section 5 a value of $n_s = 10$ will be considered to reach an equilibrium between time efficiency and accurate results.

5. Nucleation in ternary mixtures

Ternary mixtures are a situation of much more interest than binary mixtures. To start with, we have different possibilities of how a droplet can nucleate. We can have homogeneous nucleation (droplets forming inside one of the phases) or heterogeneous nucleation (droplets forming at the interface between two phases). Moreover, especially in the second case, the spherical symmetry is broken and the only way to reproduce these phenomena is using cartesian coordinates, which are by themselves a computational challenge.

The aim of this section is to compare numerical results with classical nucleation results related to homogeneous and heterogeneous nucleation. More precisely, we study whether heterogeneous nucleation is always more favorable than homogeneous nucleation (the energy barrier in the first case is smaller than in the other one), and under which conditions this difference is more relevant. We also check that the values of the contact angles at triple junctions satisfy the relations found in Section 3.

As in the binary case, we iterate the Cahn-Hilliard equation using an IMEX method for time integration. In this case, since practically all configurations we will consider are on a square two dimensional domain, we will work in the Fourier space to treat all spatial derivatives.

5.1 Free energy density

We focus our study on the two dimensional configuration. The three dimensional case is too computationally expensive to be simulated in the way we have been doing it until now, since we have to reproduce it in cartesian coordinates, and our vector of solutions would become extremely large. However, the two dimensional case already allows us to verify most of the relations we discussed in Section 3.

To start with, we have to define a new free energy density, since now we have three components instead of two. From now on, consider we have three components a, b and c, and their respective order parameters ϕ_a, ϕ_b and ϕ_c. In this case, we consider that the order parameters take a range of values on $\phi \in (0, 1)$, instead of $\phi \in (-1, 1)$ (this is because when we define the free energy density we will use some derivations from Ryan's Davis thesis [10]). We will study nucleation of phase c in several conditions. There is a restriction on the values of ϕ_a, ϕ_b and ϕ_c, which is:

$$\sum_{i=a,b,c} \phi_i = 1 \tag{67}$$

This expression allows us to work with only two order parameters and compute the third one from these two. Hence, when evolving each phase, we just need to consider the evolution of two of the phases, and then calculate the third one using Eq. 67. However, the free energy is defined in terms of the three order parameters for simplicity.

As in the binary case, we consider a free energy density which has two components: the bulk free energy density and the interface free energy density. The expression for the interface free energy density is easy to generalise from the binary case:

$$f_I(\phi_a, \phi_b, \phi_c) = \frac{W_a}{2}|\nabla\phi_a|^2 + \frac{W_b}{2}|\nabla\phi_b|^2 + \frac{W_c}{2}|\nabla\phi_c|^2$$

The values of W_a,W_b and W_c have to be determined from the definition of the interface width and interface energies.

The expression of the bulk free energy is not so direct to generalize from the binary case. A first attempt would be to consider three double well potentials, one for each order parameter. In that way, we would have the following bulk free energy:

$$f_0(\phi_a, \phi_b, \phi_c) = A_a\phi_a^2(\phi_a - 1)^2 + A_b\phi_b^2(\phi_b - 1)^2 + A_c\phi_c^2(\phi_c - 1)^2$$

However, the previous expression has a problem, and it is that it presents five additional minima which we are not interested in (corresponding to $\phi_a = \phi_b = \phi_c = 1$, $\phi_a = \phi_b = \phi_c = 0$ and one of the order parameters equal to 0 and the other two equal to 1). These minima do not have physical meaning, since the order parameters have to satisfy Eq. 67 everywhere in space, and if we impose that the third order parameter is computed from the other two, we should not have problems with this issue. However, numerical errors may arise, so we have to make some modifications to this expression.

To solve this issue we base on Ryan Davis' derivation [10], where he considers a bulk free energy which has the following expression:

$$\begin{aligned} f_0(\phi_a, \phi_b, \phi_c) = A_a\phi_a^2(\phi_a - 1)^2 + A_b\phi_b^2(\phi_b - 1)^2 + A_c\phi_c^2(\phi_c - 1)^2 + \\ C(\phi_a^2\phi_b^2(1 - \phi_c)^2 + \phi_a^2\phi_c^2(1 - \phi_b)^2 + \phi_c^2\phi_b^2(1 - \phi_a)^2 \\ + \phi_a^2\phi_b^2\phi_c^2 + (1 - \phi_a)^2(1 - \phi_b)^2(1 - \phi_c)^2) \end{aligned}$$

where C is a positive constant. The second term enforces that the only three minima are the ones corresponding to one of the order parameters equal to 1 and the rest equal to 0. A simplified form can be considered if the terms that do not contribute to the interface energy calculation are removed. For example, the $\phi_a^2\phi_b^2\phi_c^2$ term can be removed, since it is very close to 0 everywhere except near triple junctions, but its removal does not change significantly the results. The simplified expression is:

$$\begin{aligned} f_0(\phi_a, \phi_b, \phi_c) = A_a\phi_a^2(\phi_a - 1)^2 + A_b\phi_b^2(\phi_b - 1)^2 + A_c\phi_c^2(\phi_c - 1)^2 + \\ C(\phi_a^2\phi_b^2 + \phi_a^2\phi_c^2 + \phi_c^2\phi_b^2 + (1 - \phi_a)^2(1 - \phi_b)^2(1 - \phi_c)^2) \end{aligned}$$

The parameters of the free energy have to be determined, as in the binary case, using the definition of interface width and interface energy. We consider that the interface width is the same for all phases (δ) and we have three interface energies, which are γ_{ab},γ_{ac} and γ_{bc}. The definition of these parameters relies on the phase matching procedure.

We say that two order parameters are **matched** at an interface if one of them the takes values from 0 to 1 in the orthogonal direction to the surface, while the other takes values from 1 to 0. In that way, the third order parameter is equal to zero in all the region. When defining the interface energy between two phases we assume that their order parameters are matched and separated by a planar interface.

If ϕ_i and ϕ_j are matched, the definition of the interface width for these two phases is in this case (the same derivation done in Section 4.1.3 can be reproduced to obtain this relation):

$$\delta = \frac{1}{|\nabla\phi_i|_{\phi=1/2}}$$

The value of the interface width is the same for all order parameters, so this expression must be the same for whatever order parameter ϕ_i we choose. The derivative is evaluated at the center of the interface

($x = 0$), where both order parameters equal to 1/2. To evaluate this derivative we can use the Beltrami identity for this system. Given two matched order parameters, corresponding to phases i and j, the Beltrami identity reads:

$$f_0(\phi_i, \phi_j) - \left[\frac{W_i}{2}|\nabla\phi_i|^2 + \frac{W_j}{2}|\nabla\phi_j|^2\right] = 0 \tag{68}$$

$f_0(\phi_i, \phi_j)$ is defined considering $\phi_j = 1 - \phi_i$ and the third order parameter equal to 0 in the expression for the bulk free energy. Hence, if we write it in terms of ϕ_i, it has the following expression: $f_0(\phi_i, \phi_j) = (A_i + A_j + 2C)\phi_i^2(\phi_i - 1)^2$. What we end up with is the following expression for the interface width:

$$\delta = \sqrt{\frac{W_i + W_j}{2f_0(\phi_i = 1/2, \phi_j = 1/2)}} = \sqrt{8\frac{W_i + W_j}{A_i + A_j + 2C}} \tag{69}$$

The definition of the interface energy for the phases i and j is:

$$\gamma_{ij} = \int_{-\infty}^{+\infty} \left(f_0(\phi_i, \phi_j) + \frac{W_i}{2}|\nabla\phi_i|^2 + \frac{W_j}{2}|\nabla\phi_j|^2\right) dx$$

Similarly to the binary case, we can use the Beltrami identity for phases i and j and compute this expression. In the end we get:

$$\gamma_{ij} = \frac{\sqrt{2}}{6}\sqrt{(W_i + W_j)(A_i + A_j + 2C)} \tag{70}$$

So far we have four expressions with seven different parameters. We can obtain two more relations imposing that phases match at interfaces [10]. These relations are:

$$\frac{W_a}{W_b} = \frac{A_a + C}{A_b + C}$$
$$\frac{W_a}{W_c} = \frac{A_a + C}{A_c + C}$$

These relations impose a relation between the parameters W_i and A_i. In particular, the previous relations indicate that $\frac{W_a}{A_a+C} = \frac{W_b}{A_b+C} = \frac{W_c}{A_c+C}$, so we can define a new parameter, λ, in the following way: $W_i = \lambda^2(A_i + C)$. With this definition, the expressions are:

$$\delta = 2\sqrt{2}\lambda$$
$$\gamma_{ij} = \frac{\sqrt{2}}{6}\lambda(A_i + A_j + 2C)$$

The first expression shows that λ is the interface width (multiplied by the factor $2\sqrt{2} \approx 3$), as in the binary case. However, to determine the values of the parameters with respect to the interface energies and interface width we still need an extra condition. A common assumption is to assume that C satisfies the following relation [10]:

$$C = \frac{1}{6} max\{A_a + A_b, A_a + A_c, A_b + A_c\}$$

This relation is usually taken to resolve a wide range of angles. The procedure to determine the constants, then, starts by taking the largest value of the interface energies, which we will consider to be γ_{ij}. In that case, it can be shown that $C = \frac{1}{6}(A_i + A_j)$. To find the values of the rest of the parameters, the system formed by the expressions of the three interface energies has to be inverted. After doing so, we get the following relations:

$$\begin{cases} A_i = \frac{9\gamma_{ij}+12(\gamma_{ik}-\gamma_{jk})}{4\sqrt{2}\lambda} \\ A_j = \frac{9\gamma_{ij}-12(\gamma_{ik}-\gamma_{jk})}{4\sqrt{2}\lambda} \\ A_k = \frac{3\sqrt{2}}{\lambda}\gamma_{ik} - \frac{4}{3}A_i - \frac{1}{3}A_j \end{cases} \tag{71}$$

With the previous expressions we can use the physical constants as the inputs of our model. We are especially interested in comparing the different possible values of the interface energies, and considering small interface widths to be as close as possible to the sharp interface limit.

The values of the interface energies are not relevant by themselves. What we are interested in is their relation (that is, the ratios between each pair of interface energies). If we multiply all interface energies by a factor A, then all the values of A_i and C will rescale by this factor, and hence the free energy density will be multiplied by this factor. As in the binary case, this is equivalent to changing the time step, but the final configuration after convergence does not change. Hence, we will consider all values of the interface energies around a value of 10^{-2}, to follow the same procedure as in the binary case.

Finally, the contact angles are related to the interface energies via Eq. 81, derived in Section 3.2. If we compute the angles (see Fig. 4) as a function of the interface energies we get:

$$\begin{cases} \cos\theta = \frac{\gamma_{bc}^2-\gamma_{ab}^2-\gamma_{ac}^2}{2\gamma_{ab}\gamma_{ac}} \\ \cos\phi = \frac{\gamma_{ac}^2-\gamma_{ab}^2-\gamma_{bc}^2}{2\gamma_{ab}\gamma_{bc}} \end{cases} \tag{72}$$

We are also interested in checking whether our model is able to reproduce correctly this contact angles or not.

5.2 Model implementation

In a ternary system each of the order parameters evolves via the Cahn-Hilliard equation. Its general expression, assuming that the mobility coefficients M_i are all equal to 1. is:

$$\frac{\partial\phi_i}{\partial t} = \Delta\frac{\delta F}{\delta\phi_i} \tag{73}$$

The functional derivative of the free energy with respect to component i (which is the chemical potential for component i) has the following expression:

$$\frac{\delta F}{\delta\phi_i} = \mu_i = 2A_i\phi_i(1-\phi_i)(1-2\phi_i) + 2C\left[\phi_i\left(\left(\sum_{j=a,b,c}\phi_j^2\right) - \phi_i^2\right) - \frac{\prod_{j=a,b,c}(1-\phi_j)^2}{1-\phi_i}\right] - W_i\nabla^2\phi_i$$

When computing these expressions, there are two terms which do not depend on the component we are working with. Hence, we can compute them beforehand and use them for each of the components. These two terms are $S = \sum_{j=a,b,c} \phi_j^2$ and $P = \prod_{j=a,b,c}(1-\phi_j)^2$. The term $\frac{P}{1-\phi_i}$ may cause numerical errors, since normally one of the order parameters is very close to 1. and hence $P \approx 0$ and $1-\phi_i \approx 0$. The way to avoid these errors is to introduce a numerical tolerance, $\epsilon = 10^{-12}$, and compute:

$$\frac{P}{1-\phi_i} \approx \frac{(1-\phi_i)(P+\epsilon)}{(1-\phi_i)^2+\epsilon}$$

Since our simulation will be in cartesian coordinates in two dimensions, to be able to run the program in a reasonable time we cannot solve this equation in the real space. The way to do it will be the same as in binary mixtures, in the Fourier space [37]. In that case, the derivatives turn into multiplications and the program is much faster. The general algorithm will be the following:

1. The chemical potential for each phase, μ_i^n, is computed in the real space.
2. The chemical potential is transformed to the Fourier space via the FFT, $\hat{\mu_i}^n$. The order parameter is computed in the Fourier space as well, $\hat{\phi_i}^n$.
3. The time evolution is performed following an IMEX method to obtain $\hat{\phi_i}^{n+1}$.
4. The value of the vector solution is computed in real space via the Inverse Fast Fourier Transform (IFFT), to obtain ϕ_i^{n+1}.
5. Every n_s iterations, the string is reparametrized.

The general expression for $\hat{\phi}_{i,j}^{n+1}$ with respect to $\hat{\phi}_{i,j}^n$, where $\hat{\phi}_{i,j}^n$ is the value of the order parameter of component i ($i \in \{a,b,c\}$) at node j ($j = (j_x, j_y)$ and $j_x \in \{0, 2\pi/dx, ..., 2\pi\}$, $j_y \in \{0, 2\pi/dx, ..., 2\pi\}$) and iteration n, and $\hat{k} = 2\pi k$, is:

$$\hat{\phi}_{i,j}^{n+1} = \frac{\hat{\phi}_{i,j}^n + h \cdot \hat{\mu}_{i,j}^n}{1 + h\lambda^2(A_i + C)\hat{k}^4} \tag{74}$$

5.2.1 Spinodal region

As in the binary case, we have to make sure we are not in the spinodal region when phase c nucleates. Otherwise no energy barrier will be observed. In the binary case this is very simple, since the initial mean concentration has to be greater than a given limit concentration. However, for ternary mixtures the spinodal region is much more complex because it depends on two order parameters (the third one is fixed by Eq. 67), instead of one. When computing the spinodal region we will assume that $\phi_c = 1 - \phi_a - \phi_b$, and only work with two order parameters.

Given the free energy of our system, which depends on two order parameters, the system is in the spinodal region if the hessian of the free energy density is negative-definite or non-definite (the free energy curve is not convex at that point, so that there is at least one direction of descent at that point). Hence, each point of the domain must have a set of concentrations which satisfy that the hessian of the free energy is positive-definite for those values. The easiest way to check if the hessian is positive-definite or not is by examining its eigenvalues. We want that both eigenvalues are positive (if both of them are negative the hessian is negative-definite and the free energy surface is convex at that point, and if there are one positive

and one negative eigenvalues the hessian is not definite at that point and the surface is not convex nor concave).

To find the values of the eigenvalues we used a Mathematica code. We first defined the free energy density with respect to two parameters (ϕ_a and ϕ_b), result of substituting $\phi_c = 1 - \phi_a - \phi_b$ in the free energy density expression. We then compute its hessian matrix and compute its eigenvalues for certain values of the model parameters and mean concentrations.

In our simulations phases a and b are only in contact with each other at interfaces. Hence, in most of the domain one of the order parameters is 0. This allows us to determine which is the maximum value that ϕ_c can take without entering the spinodal in the bulk regions, in the special case where all the interface energies are equal. A detailed analysis shows that, in this case, the limit concentration is $\bar{\phi}_c^* = \frac{1}{2} - \frac{\sqrt{3}}{6} \approx 0.21$. That is, $\bar{\phi}_c^*$ is the maximum concentration we can consider for component c in the bulk regions without entering the spinodal.

There is one complication even when the concentration of phase c in the bulk regions, $\bar{\phi}_c$, satisfies $\bar{\phi}_c < \bar{\phi}_c^*$. Although we are not in the spinodal region inside phase a and phase b, we are in the spinodal region at the interface. Although this is not enough to provoke phase separation in general, since the interfacial energy tends to stabilize it, it provokes that phase c tends to accumulate at the interfaces, something which may cause problems when we want to study nucleation. A detailed analysis of this situation is performed in the following section.

For more complex situations (different values of the interface energies or more complex geometries) a detailed analysis has to be performed. Due to the instabilities mentioned before, caused by the presence of interfaces, the best way to determine the behaviour of the system is by evolving the Cahn-Hilliard equation of the initial and final states and determine whether they converge to the desired equilibrium states or not.

5.3 One dimensional case

Simulations in one dimension are not of special interest for studying nucleation, as we discussed for binary mixtures. However, they are interesting to study how the presence of an interface alters the initial state, when phase c is diluted over all the domain. We do not apply the string method for this case, since we are just interested in evolving the Cahn-Hilliard equation to determine whether our initial states converge to the mixed state or to the separated state (in that case phase c accumulates at the interface and phase separation takes place).

We consider phase a and b separated by an interface which divides the domain in two regions. In the first region $\phi_a = 1 - \bar{\phi}_c$ and $\phi_c = \bar{\phi}_c$, while in the second region $\phi_b = 1 - \bar{\phi}_c$ and $\phi_c = \bar{\phi}_c$. Actually, $\phi_c = \bar{\phi}_c$ in all the domain, including the interface, and phase a and b are initialized with a sharp transition at the interface.

Table 11 indicates whether the initial state converged to a mixed state or whether phase c separated from phase a and b at the interface. Different values for the mean concentration of component c were considered. The values for $\bar{\phi}_c$ were computed from the radius of a hypothetical droplet which would form if we were in two dimensions, so that we can compare these results to simulations in two dimensions (for example, if we wanted to nucleate a circular droplet in two dimensions with radius $r = 0.1$ the mean concentration of component c would be $\bar{\phi}_c = \pi r^2 = 3.14 \cdot 10^{-2}$). In all cases the interface was placed at $x = 0.5$, so the mean concentrations of components a and b are the same. The rest of the parameters used in the simulations are $N = 256$, $h = 5 \cdot 10^{-6}$, $\gamma_{ab} = \gamma_{ac} = \gamma_{bc} = 10^{-2}$, $\delta = 0.012$ and a tolerance of $tol = 5 \cdot 10^{-8}$. The concentration profiles after convergence for $\bar{\phi}_c = 3.14 \cdot 10^{-2}$ and $\bar{\phi}_c = 6.16 \cdot 10^{-2}$ are

plotted in Fig. 24.

Mean concentration of phase c	State after convergence
$3.14 \cdot 10^{-2}$	Mixed state
$4.52 \cdot 10^{-2}$	Mixed state
$6.16 \cdot 10^{-2}$	Separated state
$8.04 \cdot 10^{-2}$	Separated state
$1.02 \cdot 10^{-1}$	Separated state

Table 11: State to which the mixed state converges after running the Cahn-Hilliard evolution equation. The two possibilities are the mixed state or the separated state, in which phase c nucleates at the interface between phases a and b.

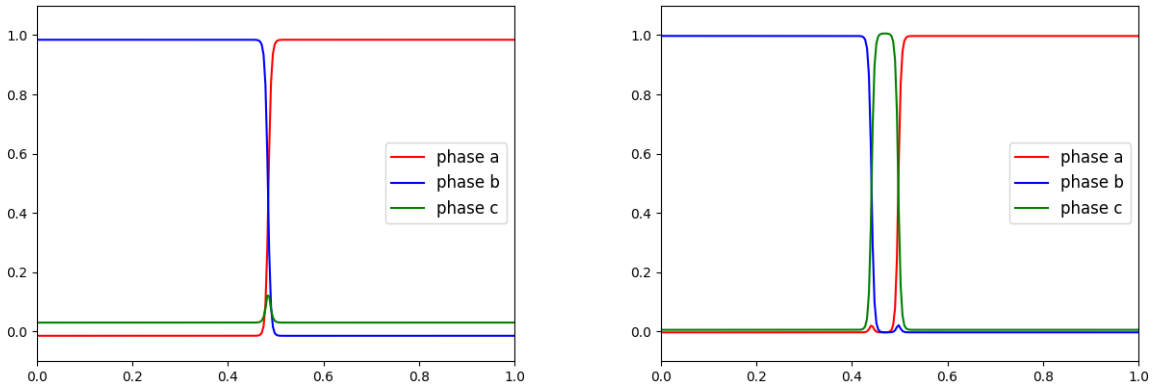

Figure 24: Final concentration profiles for initial mixed phase c. Left: $\bar{\phi}_c = 3.14 \cdot 10^{-2}$. Right: $\bar{\phi}_c = 6.16 \cdot 10^{-2}$.

If we compute the hessian of the matrix for each value of the mean concentration of component c we see that phase separation should not take place in any of the cases. However, what we observe in the table is that in some cases component c spontaneously separates and accumulates at the interface, giving rise to three distinct phases (see Fig. 24, right plot). Hence, it is not enough to check that we are outside the spinodal region to assure that the initial state will converge to the mixed state. Moreover, even when the initial state converges to the mixed state, the concentration profile is not exactly the one expected, since there is a sight increase in the value of component c at the interface. This result had already been observed in simulations when studying phase separation in ternary systems [17]. However, this effect is not really relevant, but it is interesting because it means that interfaces alter the equilibrium states in all cases, something which classical nucleation theory does not consider.

Even for the same value of the mean concentration of phase c we can have problems if we change the values of the interface energies. For example, we can consider changing γ_{ab}. The results in that case (where the rest of the parameters are the same as in the previous case, except for the time step, which had to be taken smaller ($h = 2 \cdot 10^{-6}$) for the program to converge), for a mean concentration of $\bar{\phi}_c = 3.14 \cdot 10^{-2}$, are showed in Table 12. Fig. 25 shows the final profiles obtained for the values of $\gamma_{ab} = 1.2e-2$ (left) and $\gamma_{ab} = 1.8e-2$ (right). We see that phase separation takes place in the case where $\gamma_{ab} = 1.8e-2$, which

is also the case in which we are closer to the total wetting condition (one of the interface energies is larger than the sum of the other two).

Interface energy γ_{ab}	State after convergence
$1.00 \cdot 10^{-2}$	Mixed state
$1.20 \cdot 10^{-2}$	Mixed state
$1.40 \cdot 10^{-2}$	Mixed state
$1.60 \cdot 10^{-2}$	Mixed state
$1.80 \cdot 10^{-2}$	Separated state

Table 12: State to which the mixed state converges after running the Cahn-Hilliard evolution equation. The two possibilities are the mixed state or the separated state, in which phase c nucleates at the interface between phases a and b.

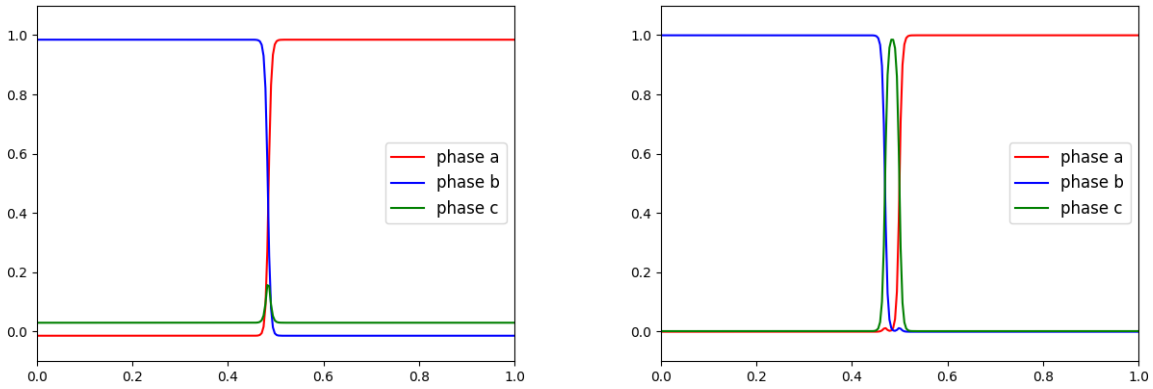

Figure 25: Final concentration profiles for initial mixed phase c. Left: $\gamma_{ab} = 1.2e-2$. Right: $\gamma_{ab} = 1.8e-2$.

One interesting observation is derived from these results. When computing the interface energy we assumed that the interface separated two phases and that the third component had a null concentration in all the region. However, in our initial states component c has a constant concentration, although not null, and we have seen that as long as we have a bit of component c it tends to accumulate at interfaces. This may be a source of error in future results, since the actual interface energy is slightly different from the theoretical one due to this fact.

The conclusion is that we have to be very careful when studying nucleation with the string method, since the initial state may spontaneously separate and then our results will not be coherent. The way to avoid that consists on checking that the initial profile after convergence has the shape it should, evolving the initial state with the Cahn-Hilliard equation before applying the string method.

5.4 Two dimensions

Our goal in this section is to compare classical nucleation theory results to numerical results. In particular we want to compare heterogeneous nucleation with homogeneous nucleation. We expect to observe that energy barriers are lower in heterogeneous nucleation, and in many cases we can predict that this relation is given by the shape factor, defined in Section 3.2.

For this reason we consider phase c nucleating inside phase a and b. Three different cases are considered: a circular droplet of phase c nucleating inside phase a, a circular droplet of phase c nucleating inside phase b and a droplet (which will not be circular due to the interface energy balance at triple junctions) of phase c nucleating at the interface between phases a and b. In all cases the initial state will be the same: we assume phase a and b are separated by two interfaces (since the domain has periodic boundary conditions), and phase c is diluted over all the domain. In the final state all three phases are separated, with phase c forming a droplet in each of the three situations.

5.4.1 Contact angles

Before studying nucleation events in two dimensions we are interested in checking whether the contact angles at triple junctions are the ones obtained from imposing force balance (see Section 3.2). To do so, we study some geometries which present triple junctions and determine the contact angles obtained from simulations. We expect to get good results when the interface energies have similar values, but discrepancies between simulations and classical results may appear for more extreme cases (very small angles or very big angles).

We consider a matrix of phase a and a circular droplet of phase b and c, with radius $r = 1/3$. The upper part of the droplet is phase c and the lower part phase b (see Fig. 26). This configuration presents two triple junctions, which are symmetric with respect to the y axis. Since we will consider symmetric cases both contact angles at triple junctions will be the same. We compute the contact angle at one of the triple junctions (the left one, for example). These angles are defined as the angle formed by the ac and the bc interface and the angles formed by the ab and bc interface (see Fig. 27). This definition gives us the suplementary anlge to the one we derived in Section 5.1, but we define it in that way for convinience.

The difficulty of measuring the angle lies in the fact that the contact angle is not very well defined in our simulations, since our interfaces are diffuse. To determine it we need two tangent directions at the triple junction, which translates in computing two tangent vectors. We compute an approximate value for the contact angle using the following algorithm (see Fig. 27):

1. The triple junction (which we call P_1) is defined as the node which maximizes the product $\phi_a \cdot \phi_b \cdot \phi_c$ (it can be shown that the values of the concentration which maximize this product satisfying Eq. 67 are all of them equal to $1/3$, condition which only happens at triple junctions).

2. Once we have P_1, we need to compute the direction of the interfaces at this node. Since the interfaces are diffuse, there is some uncertainty in the tangent direction which is proportional to the interface width. The first direction is simply the horizontal one (bc interface), so the second node, P_2 has the same x coordinate as P_1 and an arbitrary y coordinate (for example 10 nodes to the left of P_1, according to the definition of the angle we are considering).

3. There are several techniques to find the direction of the ac interface. One of them consists on finding an auxiliary node which maximizes the product $x_a \cdot x_c$ in the x direction slightly above the triple junction, which is the third node, P_3, we were looking for. This "slightly above" is chosen arbitrarily.

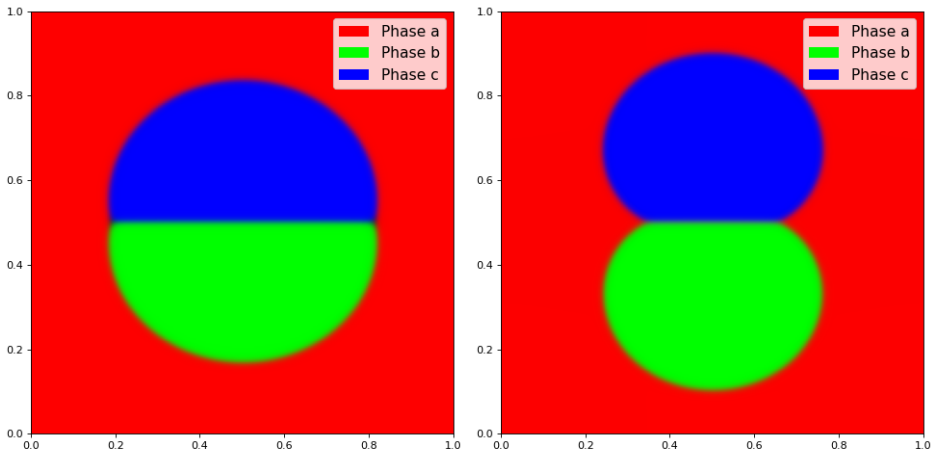

Figure 26: Final concentration profiles for three coexisting phases. The value of the contact angle at triple junctions varies with the value of γ_{bc}. Left: $\gamma_{bc} = 4 \cdot 10^{-3}$. Right: $\gamma_{bc} = 1.8 \cdot 10^{-2}$.

We call n_r the number of rows in the mesh between P_1 and P_3. If n_r is very large, since the interfaces are curved, we will measure a contact angle which is larger than the actual one. However, if we consider small values of n_r there is very few resolution to determine angles. Moreover, in that case the uncertainty in the interface width plays a very important role and the angle has a very large margin of error. Hence, an intermediate value for n_r must be chosen arbitrarily.

4. Once we have these three nodes, we can determine the angle they form using some simple geometry (angle formed by two vectors).

We consider symmetric cases in which $\gamma_{ab} = \gamma_{ac} = 10^{-2}$ (non-symmetric cases will be considered in further sections). We expect both angles to be the same, and their value should be given by Eq. 81. We chose a range of values for γ_{bc} from $4 \cdot 10^{-3}$ to $1.8 \cdot 10^{-2}$, to study angles close to 90° and close to 0°. When computing the angle a confidence interval is provided, where the limits of the interval are computed assuming P_3 is $\delta/2$ to the right or to the left of the computed value. Table 13 shows the measurements of the angles between the ac interface and the horizontal direction at the left triple junction. The following parameters were used in simulations: $N = 256$, $h = 10^{-5}$ and a tolerance of $tol = 10^{-8}$. A value of $n_r = 5$ was determined experimentally to be the most appropriate, by studying the results obtained for several values of n_r.

We observe in the first place that there is a lot of uncertainty in the measurement of the angles, since the confidence intervals are very large. For the first cases the agreement between theoretical and numerical contact angles is very good. However, for angles close to 65° results start to deviate quite a bit, since the theoretical angle is not even inside the confidence interval. This value of 65° for which results start to deviate is larger than expected, since phase field models are generally capable of resolving smaller angles.

We observe that the measured angle is always greater than the theoretical one for small angles. There are some reasons that explain this mismatch. One of them is that it is difficult to resolve small angles in a finite mesh, so we should increase the number of nodes in the domain to resolve angles with more precision, something which ends up being impossible for very small angles. Another difficulty is that for large values for γ_{bc} the interface energies are close to the total wetting condition, and Ryan's model [10] does not work in the total wetting case. Hence, the program does not converge to the correct solution in these cases.

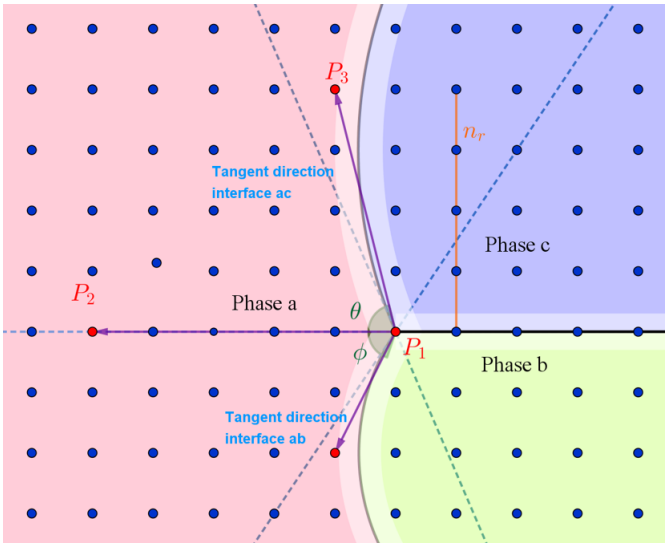

Figure 27: Contact angle calculation in a discrete mesh, in the general case where the two contact angles are different. The shaded regions around the interfaces represent diffuse interfaces. In this case the computed angles are $\theta = 75.96°$ and $\phi = 71.57°$, which are larger than the real ones due to the high value of n_r in terms of the radius of curvature of the interface.

Interface energy γ_{bc}	Theoretical contact angle	Experimental contact angle	Lower limit	Upper limit
$4.00 \cdot 10^{-3}$	78.46	76.10	70,34	79.28
$6.00 \cdot 10^{-3}$	72.54	72.31	65.28	76.29
$8.00 \cdot 10^{-3}$	66.42	70,18	62.52	74.59
$9.00 \cdot 10^{-3}$	63.26	74.76	68.53	78.23
$1.00 \cdot 10^{-2}$	60,00	69.12	61.16	73.73
$1.10 \cdot 10^{-2}$	56.63	64.47	55.42	69.93
$1.20 \cdot 10^{-2}$	53.13	68.22	60,02	73.00
$1.40 \cdot 10^{-2}$	45.57	61.97	52.46	67.82
$1.60 \cdot 10^{-2}$	36.87	51.94	41.50	59.08
$1.80 \cdot 10^{-2}$	25.84	38.82	27.41	44.38

Table 13: Contact angles comparison for different values of γ_{bc}.

Despite these discrepancies, the results follow the same tendency as the theoretical ones (the angles decrease with increasing γ_{bc}). Hence, our model does not properly reproduce angles bellow 65°, and converges to configurations where the contact angle is always a bit larger than the theoretical one, although it is complicated to determine the angles with precision.

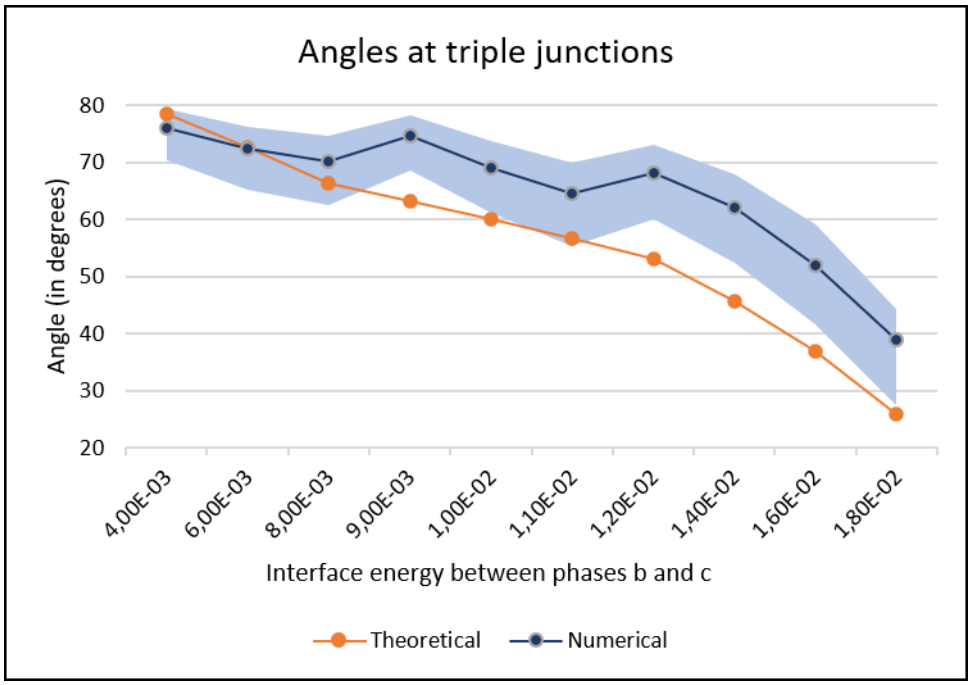

Figure 28: Numerical contact angles vs theoretical contact angles at triple junctions for several values of γ_{bc}. The orange curve are the theoretical values, the blue one are the numerical values and the blue region is the confidence interval for the numerical values.

5.4.2 Nucleation events

We now focus on comparing results from simulations to classical nucleation theory. More precisely, the procedure is the following: under the same conditions (interface energies, interface width, number of spatial nodes...) we nucleate phase c inside phase a or at the interface between phase a and b. We can compute the shape factor $S_2(\theta, \phi)$ for these conditions (see Section 3.2) and compute the energy barrier for heterogeneous nucleation with respect to homogeneous nucleation. Ideally, we expect this ratio to be $S_2(\theta, \phi)$. However, a thorough study is made to see under which conditions this agreement is satisfied.

We define our initial string as the string connecting two metastable states. The first state consists of phase a and phase b separated by two interfaces (since we consider periodic boundary conditions we always have at least two planar interfaces). Component c is initially constant in the whole region, mixed inside both phases. The mean concentration of c is computed from the final radius of the droplet of phase c (for homogeneous nucleation), since we are using a conservative method (the total concentration of each component at each time step and image on the string must be equal). In that way, if we nucleate a droplet of radius r_c inside phase a, the mean concentration of component c will be πr_c^2. This poses a limitation in the value of r_c, since if it is too large we enter the spinodal region. The intermediate images on the string are defined in such a way that first a droplet is formed and then its radius grows linearly until the final state.

As a first test we can study the range of values for which r_c is small enough so that we do not enter the spinodal region and such that the final droplet does not dilute in phases a and b (if r_c is smaller than the critical radius the droplet dilutes inside phase a and b, giving rise to the mixed state). We consider phase b to be $[0, 1]x[0, 0.5]$ and phase a to be $[0, 1]x[0.5, 1]$. Since we iterate the Cahn-Hilliard equation in the Fourier space we consider the space discretized into $N^2 = 256^2$ nodes, to optimize the FFT (the FFT

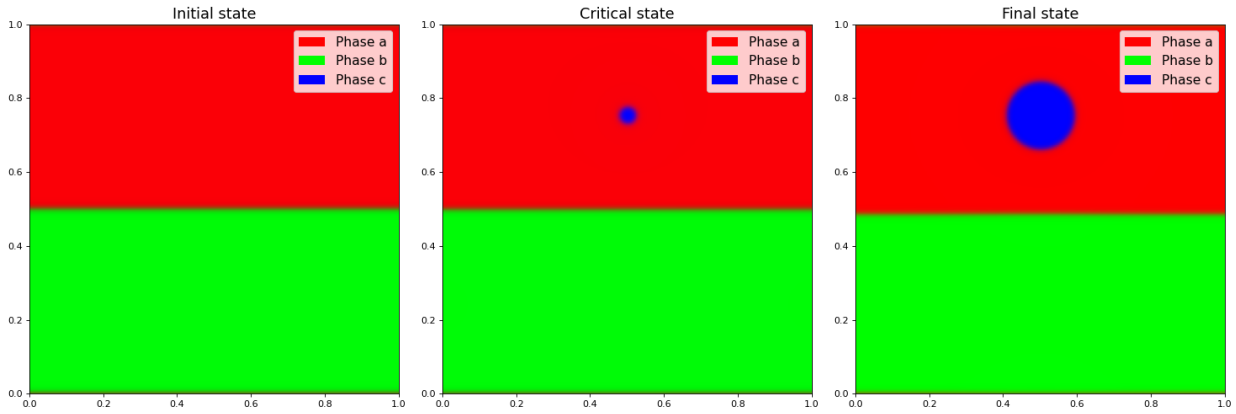

Figure 29: Final concentration profiles for homogeneous nucleation with $r_c = 0.1$. Left: Initial state. Center: Critical state. Right: Final state.

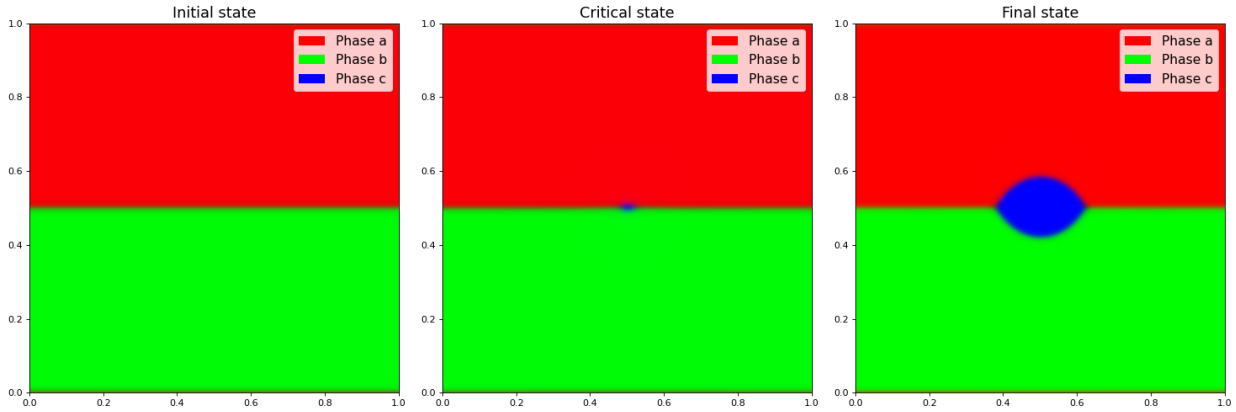

Figure 30: Final concentration profiles for heterogeneous nucleation with $r_c = 0.1$. Left: Initial state. Center: Critical state. Right: Final state.

is more efficient when we discretize the space into 2^n nodes with $n \in \mathbb{N}$, although we can also consider N not to be a power of two). Table 14 shows the energy barriers measures both for homogeneous and heterogeneous nucleation for several values of r_c, and whether the final state converged to the mixed state (two phases) or to the separated state (three phases). The rest of the parameters are $m = 50$, $h = 10^{-5}$, $\gamma_{ab} = \gamma_{ac} = \gamma_{bc} = 10^{-2}$, $\delta = 0.012$ and a tolerance of $tol = 5 \cdot 10^{-8}$ (defined in the usual way).

If we consider too small droplets the final state ends up diluting (for $r_c < 0.1$) because the final droplet size is smaller than the critical radius. We also observe that for $r_c = 0.08$ the final state in homogeneous nucleation does not converge to the final droplet, but it does in heterogeneous nucleation. This can indicate that the critical radius for heterogeneous nucleation is smaller, something which is consistent with the fact that heterogeneous nucleation is more favorable than homogeneous nucleation.

The way to solve the diluting final droplet for $r_c = 0.08$ would be considering more nodes on the mesh and thinner interface widths. However, we can consider $r_c = 0.1$ for the rest of the simulations, since the method converges both for homogeneous and heterogeneous nucleation, which is what we wanted. The final concentration profiles for $r_c = 0.1$ are shown in Figs. 29 and 30.

Radius r_c	Type of nucleation	Energy barrier	Convergence of the final state
0.12	Homogeneous	$6.41 \cdot 10^{-4}$	Separated state
	Heterogeneous	$1.68 \cdot 10^{-4}$	Separated state
0.10	Homogeneous	$8.38 \cdot 10^{-4}$	Separated state
	Heterogeneous	$3.06 \cdot 10^{-4}$	Separated state
0.08	Homogeneous	0.00	Mixed state
	Heterogeneous	$4.76 \cdot 10^{-4}$	Separated state
0.06	Homogeneous	0.00	Mixed state
	Heterogeneous	0.00	Mixed state
0.04	Homogeneous	0.00	Mixed state
	Heterogeneous	0.00	Mixed state

Table 14: Energy barrier and convergence for several final droplet radii.

For the first two cases we can even compute the shape factor $S_2(\theta, \phi)$ (see Section 3.2) as the ratio between heterogeneous and homogeneous nucleation and compare it to the theoretical one. The theoretical one has a value of $3.91 \cdot 10^{-2}$ in both cases (it only depends on the interface energies). For $r_c = 0.12$, $S_2 = 2.61 \cdot 10^{-1}$, and for $r_c = 0.1$ $S_2 = 3.65 \cdot 10^{-1}$. This is what we expected, since for a smaller value of the final droplet radius we approach the binodal and, as in the binary case, we become closer to the sharp interface limit. Only then our results can be compared to classical nucleation theory. However, there is a limit in the final size of the droplet, given by the condition that the final radius has to be larger than the critical radius. For $r_c = 0.1$ the relative error is bellow 10% (we compute the relative error as the absolute value of the difference between the theoretical and the numerical value of the shape factor divided by the theoretical value), so from now on we will consider $r_c = 0.1$ unless the opposite is said. A more thorough analysis on the shape factor for several conditions will be performed later.

An interesting observation is that, in the way we have defined our domain, divided in two identical regions, there is no difference between phase a and phase b (unless interface energies are different). This leads us to a second test: checking whether we get the same results when we study nucleation inside phase a or inside phase b. We do not expect great discrepancies to appear, only the ones due to numerical errors.

We consider a circular droplet nucleating inside phase a and the same droplet nucleating inside phase b. For the same parameters as in the previous case, we obtained, when nucleating phase c inside phase a, an energy barrier of $E = 8.38 \cdot 10^{-4}$, while, when nucleating phase c inside phase phase b, we got an energy barrier of $E = 8.34 \cdot 10^{-4}$. The relative error between these two quantities is 0.55%, which means that our implementation of the method is consistent with the symmetry of the problem. The difference is mostly due to numerical errors.

In the same line we can check what happens if we consider heterogeneous nucleation and switch the values of γ_{ac} and γ_{bc}. That is, in one case we consider $\gamma_{ac} = 8 \cdot 10^{-3}$ and $\gamma_{bc} = 10^{-2}$ and in the other $\gamma_{ac} = 10^{-2}$ and $\gamma_{bc} = 8 \cdot 10^{-3}$. The energy should be the same, since again the configuration of the system is symmetric. We nucleate a droplet of phase c at the interface between phases a and b. All the parameters are the same than in the previous case, except for γ_{ac} and γ_{bc}. If we set $\gamma_{ac} = 8 \cdot 10^{-3}$ and $\gamma_{bc} = 10^{-2}$ we get an energy barrier of $E = 2.37 \cdot 10^{-4}$, while setting $\gamma_{ac} = 10^{-2}$ and $\gamma_{bc} = 8 \cdot 10^{-3}$ gives us an energy barrier of $E = 2.34 \cdot 10^{-4}$. The relative error in that case is 1.24%, which is again very small, and caused by numerical errors. Moreover, both in the homogeneous nucleation case and heterogeneous nucleation, the program did slightly more iterations in one case than in the other. That is another reason why the results in one case are slightly different than in the other.

Now that we have checked some symmetry issues we can investigate under which circumstances the string method and classical nucleation theory are in agreement. To do so we compute the energy barriers for homogeneous nucleation and heterogeneous nucleation, and from them we compute the shape factor and compare it to the classical one.

In the first place we consider the cases where $\theta = \phi$, that is, when $\gamma_{ac} = \gamma_{bc}$. In that case the shape factor can be simplified and its expression as a function of θ is:

$$S_2(\theta) = (2\theta - \sin 2\theta)/\pi \tag{75}$$

This expression is twice the shape factor for heterogeneous nucleation on a mould wall, since in this case two circular caps are formed instead of one. We consider $\gamma_{ac} = \gamma_{bc} = 10^{-2}$ and vary γ_{ab} from $2 \cdot 10^{-3}$ to $1.8 \cdot 10^{-2}$. These are close to the extreme cases, $\gamma_{ab} = 0$ and $\gamma_{ab} = 2 \cdot 10^{-2}$, in which we would have total wetting. The phase field model is not able to reproduce total wetting, so our free energies have to satisfy the triangular inequality (each of them is smaller than the sum of the other two).

Table 15 shows the results obtained for the energy barriers in both cases (homogeneous and heterogeneous nucleation), as well as the theoretical and the numerical shape factor, which is computed as the ratio between the homogeneous and the heterogeneous energy barriers. The following parameters were considered: $m = 50$, $N = 256$, $\delta = 0.012$, $h = 10^{-5}$ and a tolerance of $tol = 5 \cdot 10^{-8}$.

Interface energy γ_{ab}	Type of nucleation	Energy barrier	Critical image	Numerical shape factor	Theoretical shape factor
$2 \cdot 10^{-3}$	Homogeneous Heterogeneous	$6.73 \cdot 10^{-4}$ $5.82 \cdot 10^{-4}$	3 3	$8.64 \cdot 10^{-1}$	$8.73 \cdot 10^{-1}$
$4 \cdot 10^{-3}$	Homogeneous Heterogeneous	$7.10 \cdot 10^{-4}$ $5.28 \cdot 10^{-4}$	3 3	$7.45 \cdot 10^{-1}$	$7.47 \cdot 10^{-1}$
$6 \cdot 10^{-3}$	Homogeneous Heterogeneous	$7.43 \cdot 10^{-4}$ $4.69 \cdot 10^{-4}$	4 3	$6.32 \cdot 10^{-1}$	$6.24 \cdot 10^{-1}$
$8 \cdot 10^{-3}$	Homogeneous Heterogeneous	$7.83 \cdot 10^{-4}$ $4.00 \cdot 10^{-4}$	6 3	$5.11 \cdot 10^{-1}$	$5.05 \cdot 10^{-1}$
10^{-2}	Homogeneous Heterogeneous	$8.38 \cdot 10^{-4}$ $3.21 \cdot 10^{-4}$	7 3	$3.83 \cdot 10^{-1}$	$3.91 \cdot 10^{-1}$
$1.2 \cdot 10^{-2}$	Homogeneous Heterogeneous	$9.10 \cdot 10^{-4}$ $2.36 \cdot 10^{-4}$	9 3	$2.59 \cdot 10^{-1}$	$2.85 \cdot 10^{-1}$
$1.4 \cdot 10^{-2}$	Homogeneous Heterogeneous	$1.01 \cdot 10^{-3}$ $1.51 \cdot 10^{-4}$	11 2	$1.50 \cdot 10^{-1}$	$1.88 \cdot 10^{-1}$
$1.6 \cdot 10^{-2}$	Homogeneous Heterogeneous	$1.16 \cdot 10^{-3}$ $6.67 \cdot 10^{-5}$	14 2	$5.76 \cdot 10^{-2}$	$1.04 \cdot 10^{-1}$
$1.8 \cdot 10^{-2}$	Homogeneous Heterogeneous	$1.95 \cdot 10^{-3}$ 0.00	49 0	0.00	$3.74 \cdot 10^{-2}$

Table 15: Energy barriers and shape factor for several values of γ_{ab}.

We see that the numerical shape factor is very close to its theoretical value in most cases, especially for low values of γ_{ab}. In fact, in the first four cases the relative error is bellow 2%, which is a very good result. Fig. 31 shows the numerical values obtained for the shape factor versus its theoretical value.

It is interesting to discuss the origin of the mismatches between theoretical values and numerical ones. In the first place, as we discussed in the previous section, the method is not able to reproduce correctly small angles (smaller than 65°). Hence, the most extreme cases fail to reproduce correctly the equilibrium concentrations. Moreover, as we increase the interface energy between phases a and b, the energy barrier for heterogeneous nucleation decreases, until it would reach a value of 0 for the total wetting case (this case

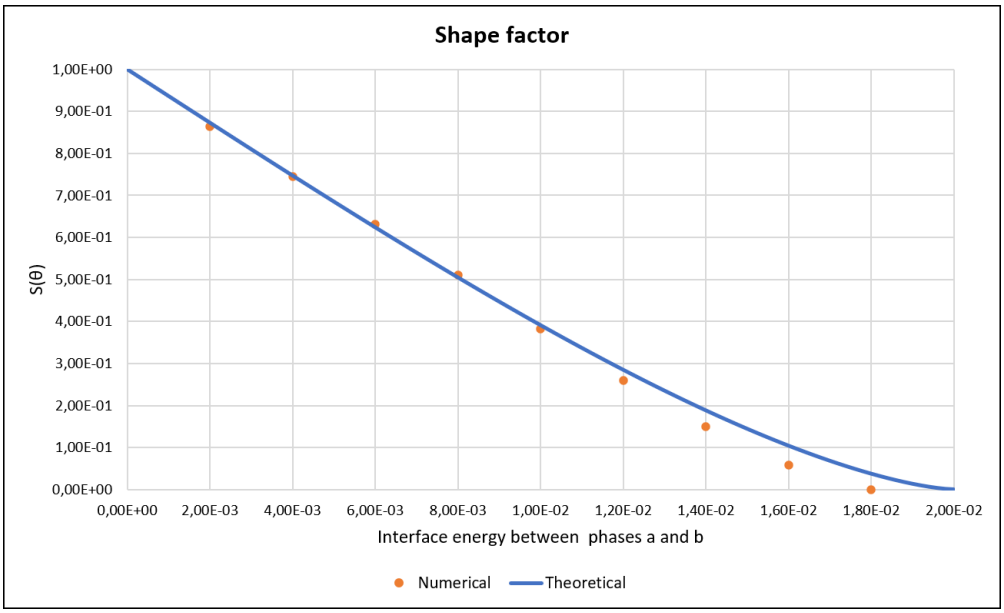

Figure 31: Shape factor comparison. The blue curve is the theoretical shape factor, and the orange samples are the values obtained from simulations.

fails also in classical nucleation theory, so it is not of much interest). This is also spotted in the value of the critical image on the string, which decreases until for $\gamma_{ab} = 1.8 \cdot 10^{-2}$ it reaches the end of the string and the energy barrier vanishes. This could be solved considering more images on the string, since our value of $m = 50$ does not allow us to determine energy barriers with a high precision if the energy barrier is very small.

There is another source of error when computing the shape factor. In most of the cases, the shape factor obtained from simulations is smaller than the theoretical one (this is especially appreciable for high values of the interface energy). This is due to the way we compute the energy barrier. Classical nucleation theory only takes into account the variation in energy due to the creation of the droplet. However, in our case there is also a contribution from the rest of the domain. In particular, there are two interfaces which also contribute to the energy we measure. In principle, especially if the critical image is close to the initial image of the string, these contributions should cancel each other and the only relevant contribution would be the one given by the droplet. However, in practice, since we are considering periodic boundary conditions, there is a small change in the interfaces and the value of the order parameters inside phase a and phase b, to keep the total concentration constant. This variation adds some error to the energy barriers computed. In particular, we expect the interfaces at the critical state to contribute more to the energy than in the initial state, so the energy barrier is always a bit bigger than we would expect.

Finally, we find that the values of the critical radii (which we did not compute explicitly, but could observe from the concentration profiles) are very small. In particular, they are comparable to the interface width. Hence, we are not in the sharp interface limit, which is the most relevant source of error.

We are now interested in checking whether the string method reproduces correctly all cases, even when both contact angles are different. In the following simulations phases a and b are not equal. Instead, phase a occupies two thirds of the domain and phase b the resting third. We compare nucleation inside phase a with nucleation at the interface between phases a and b.

Table 16 shows some results obtained for several values of the interface energies γ_{ac} and γ_{bc}. In all cases $\gamma_{ab} = 10^{-2}$. The rest of the parameters are $m = 50$, $N = 256$, $\delta = 0.012$, $h = 10^{-5}$ and a tolerance of $tol = 5 \cdot 10^{-8}$.

Interface energy γ_{ac}	Interface energy γ_{bc}	Type of nucleation	Energy barrier	Critical image	Numerical shape factor	Theoretical shape factor
$8 \cdot 10^{-3}$	$1 \cdot 10^{-2}$	Homogeneous Heterogeneous	$6.31 \cdot 10^{-4}$ $2.49 \cdot 10^{-4}$	6 3	$3.94 \cdot 10^{-1}$	$4.14 \cdot 10^{-1}$
$1 \cdot 10^{-2}$	$8 \cdot 10^{-3}$	Homogeneous Heterogeneous	$9.95 \cdot 10^{-4}$ $2.30 \cdot 10^{-4}$	10 3	$2.31 \cdot 10^{-1}$	$2.65 \cdot 10^{-1}$
$6 \cdot 10^{-3}$	$8 \cdot 10^{-3}$	Homogeneous Heterogeneous	$5.28 \cdot 10^{-4}$ $1.05 \cdot 10^{-4}$	8 2	$1.98 \cdot 10^{-1}$	$2.35 \cdot 10^{-1}$
$8 \cdot 10^{-3}$	$6 \cdot 10^{-3}$	Homogeneous Heterogeneous	$1.13 \cdot 10^{-3}$ $9.07 \cdot 10^{-5}$	49 2	$8.07 \cdot 10^{-2}$	$1.32 \cdot 10^{-1}$
$8 \cdot 10^{-3}$	$1.2 \cdot 10^{-2}$	Homogeneous Heterogeneous	$5.80 \cdot 10^{-4}$ $3.02 \cdot 10^{-4}$	3 3	$5.21 \cdot 10^{-1}$	$5.83 \cdot 10^{-1}$
$1.2 \cdot 10^{-2}$	$8 \cdot 10^{-3}$	Homogeneous Heterogeneous	$1.29 \cdot 10^{-3}$ $2.99 \cdot 10^{-4}$	12 3	$2.32 \cdot 10^{-1}$	$2.59 \cdot 10^{-1}$

Table 16: Energy barriers and shape factor for several values of γ_{ac} and γ_{bc}.

For the non symmetric cases the results are not as good as in the symmetric case. However, all the numerical shape factors are rather close to the theoretical ones (relative error smaller than 20%) except for the fourth case ($\gamma_{ac} = 8 \cdot 10^{-3}$ and $\gamma_{bc} = 6 \cdot 10^{-3}$), in which case the relative error in the shape factor is almost 40%. Moreover, for that configuration, the critical state was the ending state, something which should not happen. This may mean that the program did not converge to the right solution. Besides from that, we get some similar results as in the symmetric case. For example, the numerical shape factor is always greater than the theoretical one. As in the previous case this is partially caused by the way we compute the energy (we are computing the contribution of all interfaces, so all energy barriers are a bit greater than they should), and also because we do not resolve properly all contact angles, as discussed in Section 5.4.1. Figs. 32 and 33 show the concentration profiles obtained both for homogeneous and heterogeneous nucleation for the values $\gamma_{ac} = 1.2 \cdot 10^{-2}$ and $\gamma_{bc} = 8 \cdot 10^{-3}$.

An interesting situation is trying to reach an extreme case, corresponding to the semicircular cap. This is achieved by considering one of the interface free energies very small (for example, γ_{ac}). If we make γ_{ac} tend to zero (keeping the other two interface energies equal to maintain force balance) it can be checked that $\phi \to 0°$ and $\theta \to 90°$. Hence, we get a semicircular cap, which also corresponds to the heterogeneous nucleation on a mould wall.

We can try to consider a very extreme case, like $\gamma_{ac} = 10^{-3}$, in which case the contact angles should be 87.13° and 5.73°. The program diverges for these conditions, both for homogeneous and heterogeneous nucleation, since we are too close to the total wetting condition. Hence, we have to gradually approach the semicircular cap and study the shape factor obtained in each case.

Table 17 shows the results obtained for different values of γ_{ab}, both for homogeneous and heterogeneous nucleation. In that case we considered both phases a and b to be equal (50% of the domain each). The rest of the parameters are $m = 50$, $N = 256$, $\delta = 0.012$, $\gamma_{ac} = 10^{-2}$, $\gamma_{bc} = 10^{-2}$, $h = 10^{-5}$ and a tolerance of $tol = 5 \cdot 10^{-8}$.

We can see that the results do not match very well to classical nucleation theory, since in all cases the shape factor is quite smaller than its theoretical value (the relative error is in all cases around 20%). This is not a very surprising result, since even for $\gamma_{ac} = 6 \cdot 10^{-2}$ $\phi = 34.92°$, which is too small to be resolved properly. Moreover, in all cases the critical image on the string was the third one. Hence, the energy barrier may not be determined properly and may have some numerical error. One way to solve this would be increasing the number of images on the string. Figs. 34 and 35 show the concentration profiles with

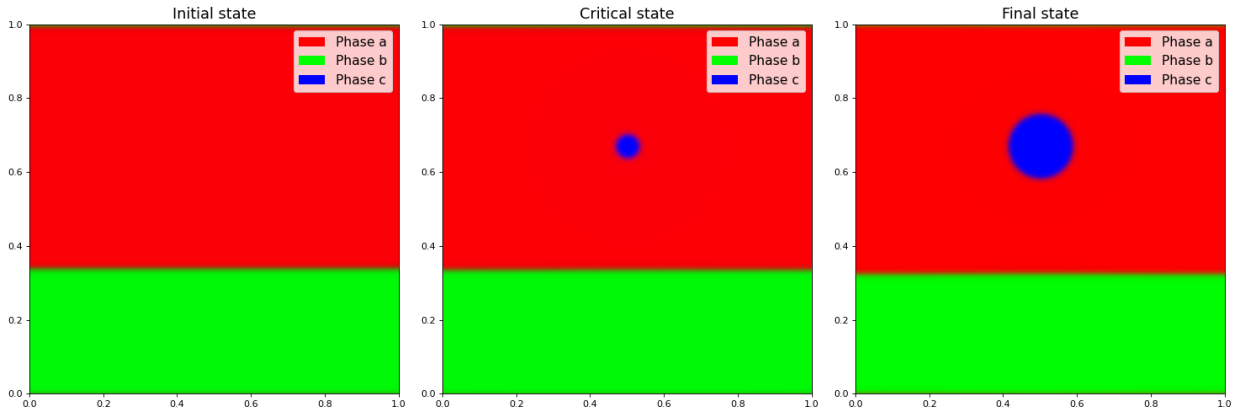

Figure 32: Final concentration profiles for homogeneous nucleation with $\gamma_{ac} = 1.2 \cdot 10^{-2}$ and $\gamma_{bc} = 8 \cdot 10^{-3}$. Left: Initial state. Center: Critical state. Right: Final state.

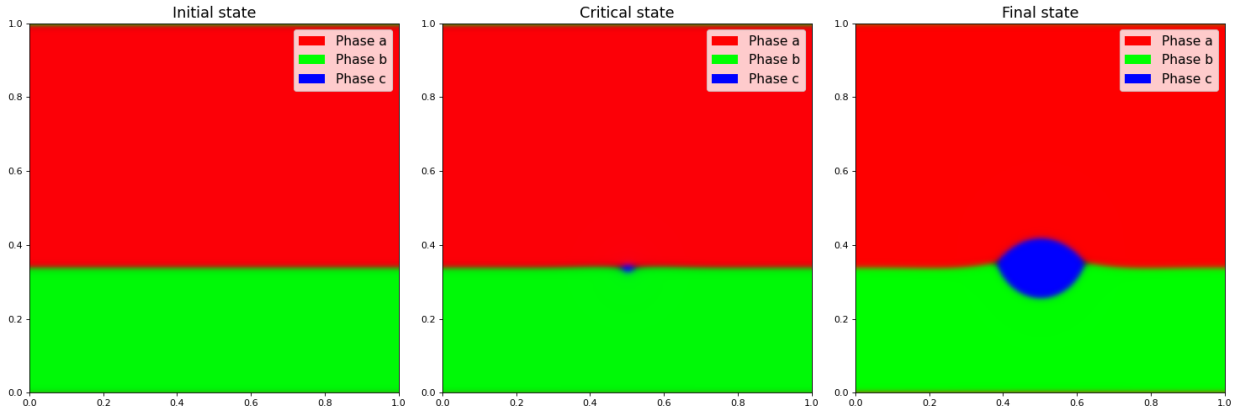

Figure 33: Final concentration profiles for heterogeneous nucleation with $\gamma_{ac} = 1.2 \cdot 10^{-2}$ and $\gamma_{bc} = 8 \cdot 10^{-3}$. Left: Initial state. Center: Critical state. Right: Final state.

Interface energy γ_{ab}	Type of nucleation	Energy barrier	Critical image	Numerical shape factor	Theoretical shape factor
$6 \cdot 10^{-3}$	Homogeneous	$4.83 \cdot 10^{-4}$	3	$3.58 \cdot 10^{-1}$	$4.36 \cdot 10^{-1}$
	Heterogeneous	$1.73 \cdot 10^{-4}$	3		
$5 \cdot 10^{-3}$	Homogeneous	$4.03 \cdot 10^{-4}$	3	$3.55 \cdot 10^{-1}$	$4.47 \cdot 10^{-1}$
	Heterogeneous	$1.43 \cdot 10^{-4}$	3		
$4 \cdot 10^{-3}$	Homogeneous	$3.22 \cdot 10^{-4}$	3	$3.55 \cdot 10^{-1}$	$4.57 \cdot 10^{-1}$
	Heterogeneous	$1.14 \cdot 10^{-4}$	3		
$3 \cdot 10^{-3}$	Homogeneous	$2.42 \cdot 10^{-4}$	3	$3.63 \cdot 10^{-1}$	$4.68 \cdot 10^{-1}$
	Heterogeneous	$8.79 \cdot 10^{-5}$	3		
$2 \cdot 10^{-3}$	Homogeneous	$1.62 \cdot 10^{-4}$	3	$3.99 \cdot 10^{-1}$	$4.79 \cdot 10^{-1}$
	Heterogeneous	$6.48 \cdot 10^{-5}$	3		

Table 17: Energy barriers and shape factor for several values of γ_{ac}.

$\gamma_{ac} = 2 \cdot 10^{-3}$ for homogeneous and heterogeneous nucleation, respectively.

By examining Fig. 35 we can see something else which we did not take into account, which are curved

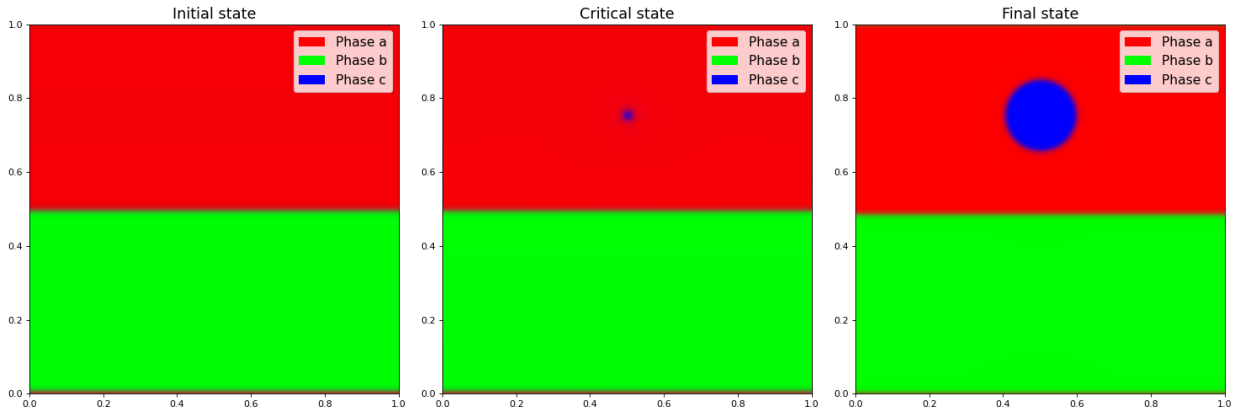

Figure 34: Final concentration profiles for homogeneous nucleation with $\gamma_{ac} = 2 \cdot 10^{-3}$. Left: Initial state. Center: Critical state. Right: Final state.

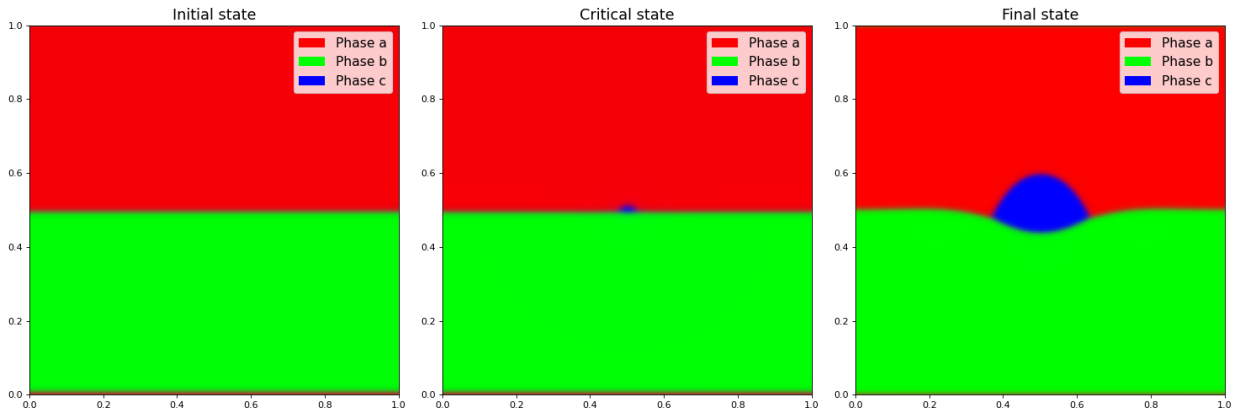

Figure 35: Final concentration profiles for heterogeneous nucleation with $\gamma_{ac} = 2 \cdot 10^{-3}$. Left: Initial state. Center: Critical state. Right: Final state.

interfaces between phases a and b. When considering heterogeneous nucleation at an interface we assumed that the interface was flat and a droplet formed keeping the interface flat in the process. However, this figure shows that the final ab interface is curved near the triple junctions. In fact, it can be shown that in equilibrium all interfaces have constant curvature (they are flat or circular caps), something which does not happen in this simulation. This means that the program would need to run for a longer period of time (consider a much smaller tolerance) until the ab interface was completely curved, something which is very difficult to obtain in practice due to the speed of the program. Moreover, the energy barrier for heterogeneous nucleation should be recalculated assuming curved interfaces, and the expression for the shape factor would change as well.

The curvature of the interfaces can be determined imposing an additional restriction to the computation of the shape factor. There is a concept we did not take into account when nucleating a phase at an interface, which is the Laplace pressure. The Laplace pressure is the difference in the pressure across a curved interface [40]. Since we have three interfaces, we have to impose that all Laplace pressures between different phases are balanced. This condition can only be achieved if the interfaces have a specific curvature.

These terms should be taken into account when computing the contact angles at triple junctions and shape factors. However, this discussion is out of the scope of this thesis.

One last observation is that the problem of curved interfaces only happens for non symmetric cases. That is, if $\gamma_{ac} = \gamma_{bc}$, then the ab interface is flat and all the theoretical results are correct. However, for the non symmetric case theoretical results should be adjustedto take into consideration the curvature of the ab interface.

5.4.3 Improvements

There is an important issue which has appeared in many simulations. In most cases the critical state along the string was very close to the initial state, and the energy barrier was very small. This was especially relevant for heterogeneous nucleation, where the energy barriers are always smaller than in homogeneous nucleation. This has two main implications. The first one is that the energy barrier presents some error due to the coarse discretization along the string. The second one is that the critical radius is usually very small, and hence comparable to the interface width. This problems are mostly caused by numerical limitations: in many cases our programs take some hours to run, or even days, so pushing them forward by considering more images on the string or considering finer meshes are very complicated solutions. However, two solutions are proposed in that line.

The first one is simply considering increasing the value of $N = 512$ in some selected cases where the critical nucleus already is slightly resolved (although it does not reach the sharp interface limit). This is the maximum value we can consider to have a program which can run in a reasonable time (some days).

The second solution is a bit more complex, and it consists on changing the number of images on the string on the fly [11]. The procedure consists on choosing an initially low number of images on the string. When a certain tolerance is reached, the number of images on the string is duplicated. The new images on the string are computed by linearly interpolating the new string with the old one. This process can be repeated as many times as desired (in our case we do it twice, so the final number of images on the string is four times the initial one).

To try both solution some of the cases where the critical nucleus was resolved better are considered. The most resolved critical nuclei were the symmetric cases with $\gamma_{ac} = \gamma_{bc} = 10^{-2}$ and varying γ_{ab}. In the first place we perform the same test but initializing the string with $m = 30$ images, so that in the end it has 120 images. The rest of the parameters are the same as in the original test, except for the tolerance on the error. In that case three tolerances must be considered, each of them determining at which point we duplicate the number of images on the string. Experimentally we found that a good choice of the tolerances is $tol_1 = 10^{-7}$, $tol_2 = 10^{-8}$ and $tol_3 = 10^{-9}$. Table 18 shows the results obtained in these tests.

Interface energy γ_{ab}	Type of nucleation	Energy barrier	Critical image	Numerical shape factor	Theoretical shape factor
$8 \cdot 10^{-3}$	Homogeneous	$7.81 \cdot 10^{-4}$	17	$4.82 \cdot 10^{-1}$	$5.05 \cdot 10^{-1}$
	Heterogeneous	$3.77 \cdot 10^{-4}$	9		
10^{-2}	Homogeneous	$8.41 \cdot 10^{-4}$	21	$3.57 \cdot 10^{-1}$	$3.91 \cdot 10^{-1}$
	Heterogeneous	$3.00 \cdot 10^{-4}$	8		
$1.2 \cdot 10^{-2}$	Homogeneous	$9.17 \cdot 10^{-4}$	26	$2.39 \cdot 10^{-1}$	$2.85 \cdot 10^{-1}$
	Heterogeneous	$2.19 \cdot 10^{-4}$	8		

Table 18: Energy barriers and shape factor for several values of γ_{ab}.

Surprisingly we get worse results than in the original case, when less images on the string were considered. However, Fig. 36 shows that this second case was more accurate than the original one for reproducing the

critical state, especially for the heterogeneous case, since the curves are smoother near the maximum. In any case, we get a shape factor which is close enough to the theoretical value, so we can still argue that the method behaves correctly when reproducing classical nucleation results.

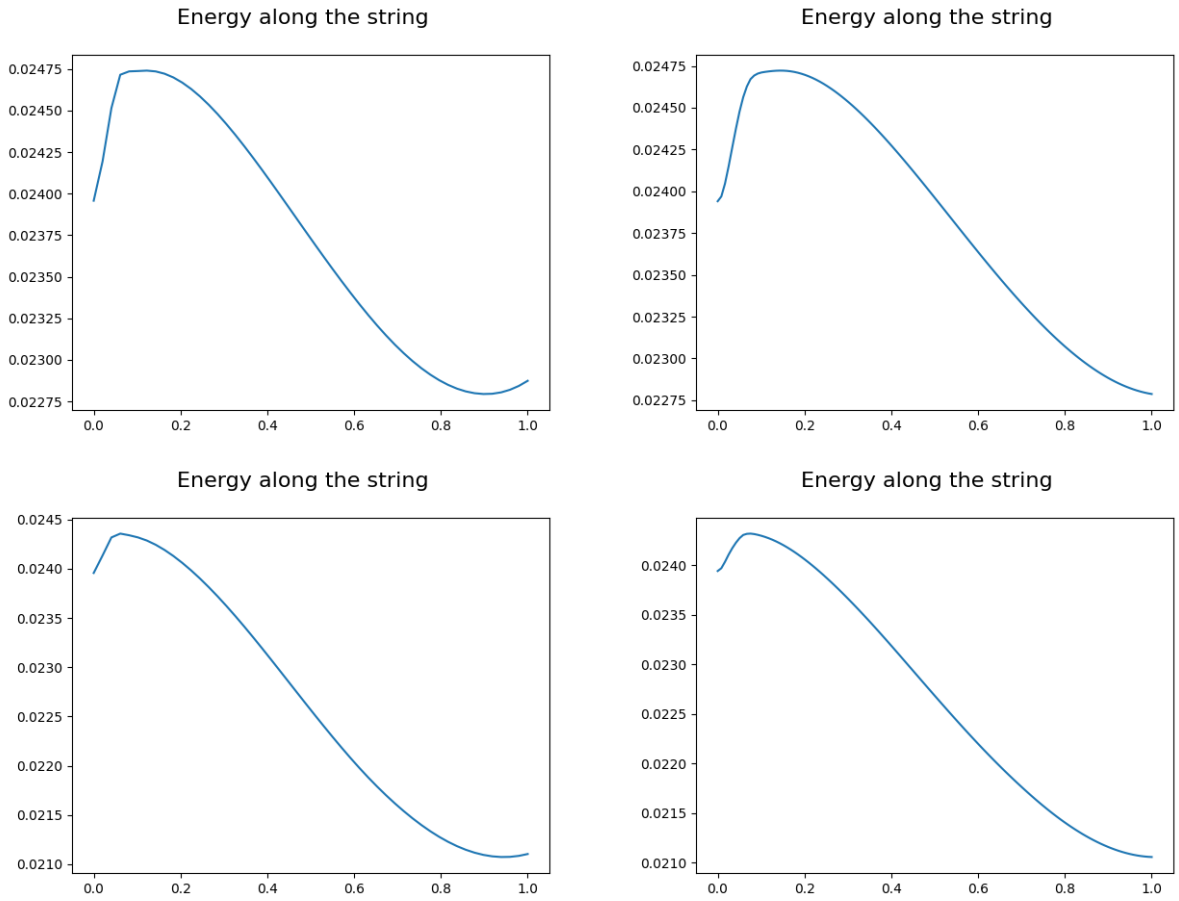

Figure 36: Energy along the string for homogeneous nucleation (upper row) and heterogeneous nucleation (lower row), with $\gamma_{ab} = 8 \cdot 10^{-3}$. Left: fixed $m = 50$. Right: variable m.

The second test is a combination of the two proposals. We consider the same cases, with $N = 512$ and $\delta = 0.006$. The initial number of images on the string is $m = 15$, so that in the end we have 60 images on the string. The goal in this case is not to resolve with more precision the critical state, but to reach (if possible) the sharp interface limit. Table 19 shows the results obtained for γ_{ab} ranging from $8 \cdot 10^{-3}$ to $1.4 \cdot 10^{-2}$ (the rest of the parameters are the same as in the previous case).

We observe that the results are not very good, due to the fact that the energy barriers are very small in all cases (the critical state is in all cases the second image on the string). The critical radii are not well resolved, so there is a lot of error in the measurement of the energy barriers. Something similar happened in the binary case: when reducing the interface width the critical image becomes closer to the initial state. The way to solve it was to go closer to the binodal (in the binary case increasing the mean concentration). We can try something similar here by decreasing the radius of the droplet.

We consider now a value of $r_c = 0.08$. Since we are closer to the binodal we expect the energy barriers and critical radii to increase. Table 20 shows the values for the energy barriers and shape factors obtained

Interface energy γ_{ab}	Type of nucleation	Energy barrier	Critical image	Numerical shape factor	Theoretical shape factor
$8 \cdot 10^{-3}$	Homogeneous Heterogeneous	$4.93 \cdot 10^{-4}$ $2.01 \cdot 10^{-4}$	1 1	$4.08 \cdot 10^{-1}$	$5.05 \cdot 10^{-1}$
10^{-2}	Homogeneous Heterogeneous	$4.89 \cdot 10^{-4}$ $1.56 \cdot 10^{-4}$	1 1	$3.20 \cdot 10^{-1}$	$3.91 \cdot 10^{-1}$
$1.2 \cdot 10^{-2}$	Homogeneous Heterogeneous	$4.70 \cdot 10^{-4}$ $1.11 \cdot 10^{-4}$	1 1	$2.35 \cdot 10^{-1}$	$2.85 \cdot 10^{-1}$
$1.4 \cdot 10^{-2}$	Homogeneous Heterogeneous	$4.96 \cdot 10^{-4}$ $6.32 \cdot 10^{-5}$	2 1	$1.27 \cdot 10^{-1}$	$1.88 \cdot 10^{-1}$

Table 19: Energy barriers and shape factor for several values of γ_{ab}.

by repeating the previous simulations (same parameters) but with $r_c = 0.08$.

Interface energy γ_{ab}	Type of nucleation	Energy barrier	Critical image	Numerical shape factor	Theoretical shape factor
$8 \cdot 10^{-3}$	Homogeneous Heterogeneous	$5.98 \cdot 10^{-4}$ $2.86 \cdot 10^{-4}$	5 2	$4.78 \cdot 10^{-1}$	$5.05 \cdot 10^{-1}$
10^{-2}	Homogeneous Heterogeneous	$6.27 \cdot 10^{-4}$ $2.34 \cdot 10^{-4}$	6 2	$3.74 \cdot 10^{-1}$	$3.91 \cdot 10^{-1}$
$1.2 \cdot 10^{-2}$	Homogeneous Heterogeneous	$6.71 \cdot 10^{-4}$ $1.80 \cdot 10^{-4}$	8 2	$2.68 \cdot 10^{-1}$	$2.85 \cdot 10^{-1}$
$1.4 \cdot 10^{-2}$	Homogeneous Heterogeneous	$7.34 \cdot 10^{-4}$ $1.23 \cdot 10^{-4}$	10 2	$1.68 \cdot 10^{-1}$	$1.88 \cdot 10^{-1}$

Table 20: Energy barriers and shape factor for several values of γ_{ab}.

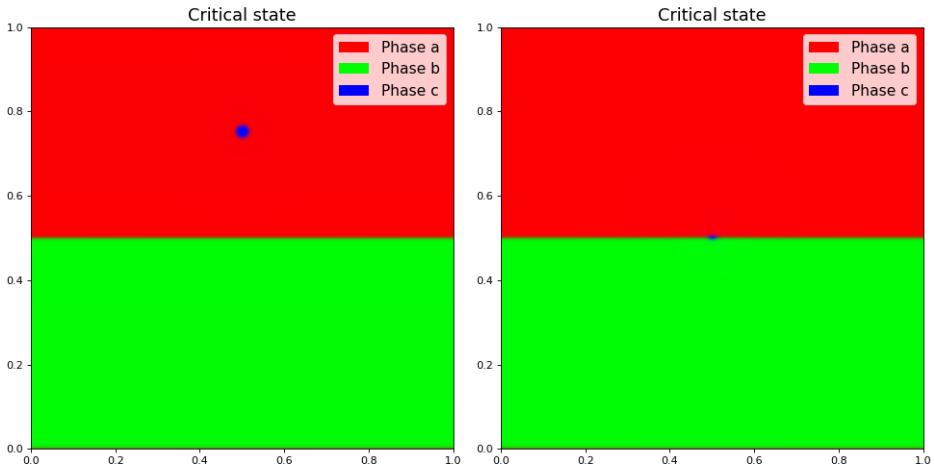

Figure 37: Critical states for $r_c = 0.08$ and $\gamma_{ab} = 10^{-2}$. Left: Homogeneous nucleation. Right: Heterogeneous nucleation.

In that case the shape factor adjusts better to the theoretical value than for $r_c = 0.1$. In the first three cases the relative error is close to 5%, and in the last one it is close to 10%, which is still is a reasonable result. The problem with this configuration is that some of the simulations already lasted several to run, so it is quite difficult to improve them beyond this limit. Moreover, for heterogeneous nucleation the critical image is still very close to the initial one (second image in all cases). Hence, and because the energy barriers

are quite small, they are not determined with very high precision. Fig. 37 shows the critical nuclei with $r_c = 0.08$ and $\gamma_{ab} = 10^{-2}$ for homogeneous and heterogeneous nucleation.

On the other hand, we did not achieve our goal with these simulations, which was reaching the sharp interface limit. In the homogeneous case we did get a critical state which was well resolved (we should check whether we are actually in the sharp interface limit). However, for the heterogeneous case we are quite far from this situation, since the critical state is very poorly resolved, and the only thing that can be observed is a small fluctuation at the center of the droplet.

All in all, the conclusion is that there is a strong limitation in the resolution we can reach due to numerical issues and efficiency of the programs. We cannot both increase very much the number of images on the string and the number of spatial nodes, so we have to reach a compromise. However, even without reaching the sharp interface limit, as in the binary case, results are comparable to theoretical ones, which proves that the string method is an efficient way to study nucleation events for ternary mixtures.

6. Conclusions

The string method has proven to be very efficient to study nucleation events in binary and ternary systems. It reproduced correctly classical nucleation results, although some limitations were found, especially for ternary systems.

The algorithm performed very well for binary mixtures. On the first place, from a qualitative point of view, droplets were observed to form via a quick increase in concentration followed by the growth of the droplet. We were able to obtain results in agreement with classical nucleation theory both for systems in two and three dimensions. Moreover, classical nucleation results were obtained even when the sharp interface limit was not obtained. However, the string method is especially appropriate to study nucleation when we are close to the binodal region. In the three dimensional case energy barriers and critical radii evolved following the same relation as theoretical results, but there was a factor of proportionality between numerical and theoretical results. We ere not able to fully determine the origin of this mismatch, and a more exhaustive investigation should be performed to determine the cause of these errors.

Limitations appear when we approach the spinodal region. In these cases the critical state in phase separation does not present the shape given by classical nucleation theory. Instead, the critical state corresponds to a state where the droplet has not reached its maximum concentration yet. In these cases the results cannot be compared to classical nucleation theory. However, nucleation theory does some approximations which are not realistic, like that the nucleus forms instantaneously with the maximum concentration, growing until it reaches the critical radius. Numerical results indicate that for configurations close to the spinodal this is not the case. Instead, the droplet formation consists of a process of **enrichment**, in which the concentration inside the droplet increases keeping a fixed size until it reaches the maximum concentration, followed by a process of **growth**, in which the size of the nucleus increases, keeping the concentration constant inside the nucleus. We also observed that the critical nucleus presented a value of the concentration at the center of the droplet slightly smaller than expected. This is due to the Gibbs-Thomson effect, which introduces a change in chemical potential across interfaces which translates into a deviation from the theoretical profiles.

Another important achievement was checking that in the two dimensional case the simplified radial dynamics in polar coordinates correctly reproduced the same results as in the cartesian case, where both space components are considered. This allows us to consider the simplified dynamics in any symmetric case, which is always the case for homogeneous nucleation, if restricted to a neighbourhood of the droplet. We could also observe from these cases that we can resolve with high accuracy the energy barriers and critical radii from the string method, but only when we are close to the binodal.

For ternary mixtures results were also quite good, although some more issues appeared. The number of possibilities increases exponentially, and some cases fail to reproduce classical nucleation results.

For the symmetric cases very good results were obtained. The shape factor was found to agree with the classical one for intermediate values of the interface energies. For more extreme cases, close to the total wetting condition, results started to separate from classical ones. However, in most cases it was mostly due to numerical issues, since energy barriers become very small, especially for heterogeneous nucleation. Moreover, the phase field method fails to reproduce very large or very small contact angles, so the method is especially efficient for intermediate values of the interface energies.

The non-symmetric cases did not perform as well as the symmetric one. The shape factors did not adjust with a very high precision the classical ones. However, they follow the correct trends in terms of dependency with the values of the interface energies, and they are still close enough to the theoretical values to claim that the results are satisfactory. However, a deeper look at the results makes us consider that classical

results should be reviewed, since curved interfaces appeared for high values of the interface energies, and the classical nucleation results we proposed did not exhibit that behaviour. The balance between Laplace pressures should be considered and new theoretical shape factors for the non-symmetric cases should be computed.

The part where results deviated more to the classical ones was the contact angles at triple junctions. We were only able to get coherent results for a very limited interval of contact angles, smaller than the expected one, according to [10], and in all cases there was a lot of uncertainty. The method was already expected to fail for small angles, but it also failed for intermediate angles. However, this did not affect the calculation of the energy barriers and shape factors, which matched quite well with classical results.

From a numerical point of view, we were able to take a lot of advantage of the string method. It is a very simple method which allows to make some efficient enhancements, like changing the number of images along the string on the fly. We found that for such complex systems it is very sensitive to initial conditions, so a first approximation of the final string had to be known beforehand.

In terms of computational efficiency the programs turned out to be computationally quite expensive. In cartesian coordinates for two dimensions this poses a very strong limitation on the accuracy that can be achieved, since there is a maximum number of spatial nodes that can be considered. This in turn limited the resolution of the critical state and made it impossible to reach the sharp interface limit for ternary mixtures. Moreover, since the only efficient way to iterate the method was in the Fourier space, this also imposed periodic boundary conditions, something which can be quite limiting in some situations as well. With this formalism it would be impossible to perform simulations in three dimensions using cartesian coordinates, and alternative ways to make the program faster should be considered.

6.1 Future work

Many interesting results were found during the research which can lead to future investigation. We comment some of them.

To start with, the string method can be used to study nucleation events in multicomponent liquid mixtures for more than three components. In that way some interesting situations can be studied, since the possible phase morphologies for systems with more than three phases are very diverse. In that line, heterogeneous nucleation plays a much more interesting role in those systems. Nucleation can take place inside bulk regions (homogeneous nucleation), at interfaces or even at triple junctions. Depending on the value of the interface energies some processes may be more favorable than others.

Some other cases which can be studied are nucleation of more than one droplet at the same time. When nucleation takes place on a material system, several nuclei form at the same time. Some of these end up reaching the critical state and growing until complete phase separation is achieved, while others do not grow enough and end up collapsing. Nucleating several droplets at the same time can be numerically very complex due to the limitations of the program, so another option would be to study how to make the program accurate enough to be able to resolve several nuclei at the same time.

We could also consider some situations which are relevant in their applications. For example, considering a spherical system with three components where one of them acts as a catalyst (situation which can model protein diffusion in cells). In particular, there are two phases: one of them contains one of the components, which acts as the catalyst, while the other two are mixed in the surrounding phase. It would be interesting to study phase separation in this situation in different conditions, where the catalyst has different interaction parameters with the other two components.

Another important issue which can be handled are curved interfaces in non-symmetric heterogeneous nucleation. A new derivation of the shape factors should be performed, taking into consideration the Laplace pressure, and it could be compared to numerical results.

We can also consider improving the method by considering irregular meshes. Since our main limitation was the computational efficiency, it is desirable to reduce the complexity of the program. One way to do it consists on changing the mesh we used, which was regular in all cases, for a non-regular one which has more resolution near the interfaces. This would imply changing the finite difference scheme we have used for a finite element method, which can support irregular meshes. This would make the mathematical treatment of the problem much more complicated, but probably much more efficient from a numerical point of view. This approximation would be especially useful if we considered a droplet forming near an interface, for ternary systems, since most of the domain in that configuration consists of a bulk region where we do not need a great resolution.

Finally, due to the high computational cost of the string method for systems modeled using the phase field dynamics, some ways to improve the string method could be studied. In particular the improvement of changing the number of images along the string on the fly was particularly useful, since it allows to resolve quite well energy barriers in a reasonable time. Another option would be to parametrize the string using an energy-weighted arc length parametrization, since in that way we could resolve better the energy barriers with the same number of images on the string. This would be especially useful for the cases where the critical image was very close to the initial one. The same method could be optimized from a computational point of view, perhaps taking advantage of preexisting libraries or using other programming languages which are more efficient for these kind of problems.

A. The shape factor in heterogeneous nucleation

As discussed in section 3.2, heterogeneous nucleation can take place in contact with a mould wall or at interfaces between two phases, for ternary systems. The expression for the free energy density has the same aspect for homogeneous nucleation and for heterogeneous nucleation except for a factor which only depends on the geometry of the configuration. This factor is usually referred to as the **shape factor**, and it can be computed using some simple geometry in each of the configurations. In this appendix we present the derivation for the expression of the shape factor in each of these configurations.

Let us consider in the first place the two dimensional case. Assume that we have a nucleus forming in contact with the mould wall (see Fig. 38). In this configuration, assuming γ_{SL} is isotropic, for a fixed volume, the shape that minimizes the interface energy of the nucleus is a circular cap. This cap forms an angle θ with the mould wall that satisfies the balance relation between the interface energies at triple junctions [41]. That is:

$$\gamma_{SM} + \gamma_{SL} cos(\theta) = \gamma_{ML} \tag{76}$$

where γ_{SM}, γ_{SL} and γ_{ML} are the solid/mould wall, solid/liquid and liquid/mould wall interface free energies, respectively. This equation comes from imposing that the interface tensions are balanced in the x direction at the triple junction (we do not impose balance in the y direction in that case, since we assume that the mould wall is fixed and cannot deform). We can thus derive the expression for the contact angle if we are given the interface free energies, something which will be useful when comparing our results from simulations with classical nucleation theory.

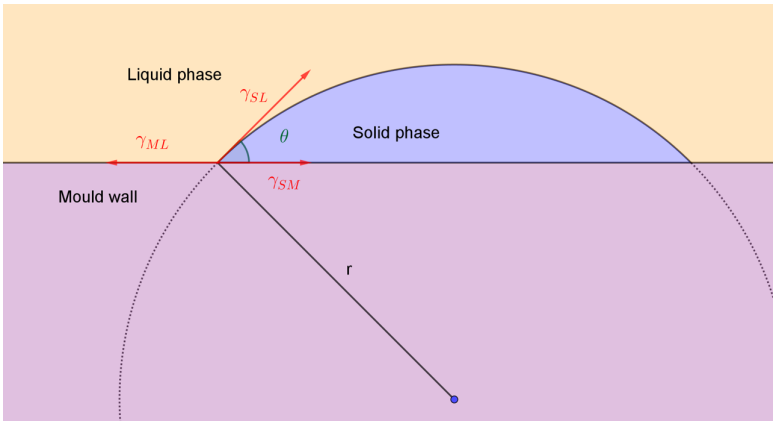

Figure 38: Nucleus forming in contact with a mould wall.

As in homogeneous nucleation, the formation of the embryo is associated with an increase in free energy, given by the expression:

$$\Delta G_{het} = -A_V \Delta G_V + l_{SL}\gamma_{SL} + l_{SM}\gamma_{SM} - l_{SM}\gamma_{ML} \tag{77}$$

where A_V is the area of the circular cap and l_{SL} and l_{SM} are the solid/liquid and solid/mould wall interface lengths. Using some simple geometry and combining it with Eq. 76, we can write all these terms as a function of the contact angle. If we call r the radius of the circular cap (see Fig. 38), then we have the following expressions for the areas and lengths:

$$A_V = \theta r^2 - \sin\theta\cos\theta r^2$$

$$l_{SL} = 2\theta r$$

$$l_{SM} = 2\sin\theta r$$

Hence, the expression for the increase of free energy is given by:

$$\Delta G_{het} = -(\theta r^2 - \sin\theta\cos\theta r^2)\Delta G_V + 2\theta r\gamma_{SL} + 2\sin\theta r\gamma_{SM} - 2\sin\theta r\gamma_{ML}$$

Using Eq. 76 we can rewrite this as:

$$\Delta G_{het} = -(\theta r^2 - \sin\theta\cos\theta r^2)\Delta G_V + 2\theta r\gamma_{SL} - 2\sin\theta r\cos\theta\gamma_{SL} = (\theta - \sin\theta\cos\theta)\cdot(-r^2\Delta G_V + 2r\gamma_{SL})$$

Finally, this expression can be written in the following way:

$$\Delta G_{het} = (-\pi r^2\Delta G_V + 2\pi r\gamma_{SL})S_1(\theta) \tag{78}$$

where:

$$S_1(\theta) = (\theta - \sin\theta\cos\theta)/\pi \tag{79}$$

Observe that we get an expression which is almost identical to the homogeneous nucleation case (see Eq. 9 in Section 3.1), except for the factor $S_1(\theta)$, which only depends on the contact angle. This factor is called the **shape factor** [31].

The second case we can consider is the formation of a droplet at an interface between two other phases. This case can take place when two phases are present and a third phase is formed (a situation studied in ternary mixtures). In that case, the nucleus will have a shape consisting on two circular caps, so that the nucleus will have kind of almond shape (see Fig. 39). Consider that we have phase c nucleating at the interface between phases a and b. In that case, the increase in free energy is computed as:

$$\Delta G_{het} = -A_V\Delta G_V + l_{ac}\gamma_{ac} + l_{bc}\gamma_{bc} - l_{ab}\gamma_{ab} \tag{80}$$

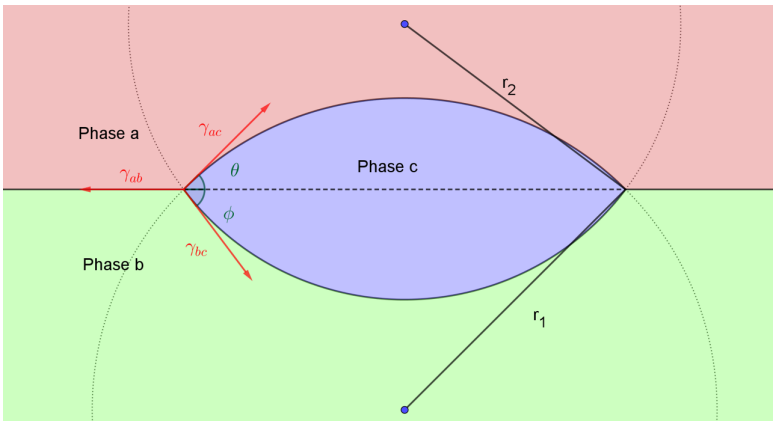

Figure 39: Nucleus forming at an interface between two phases.

We can define two contact angles, θ and ϕ, defined as the angles formed by the ac and bc interfaces with the ab interface, respectively (see Fig. 39). The interface tensions balance at the triple junctions, in that case both in the x and the y direction, since all interfaces are deformable [41]. We have the following relations:

$$\begin{cases} \gamma_{ab} = \gamma_{ac}\cos\theta + \gamma_{bc}\cos\phi \\ \gamma_{ac}\sin\theta = \gamma_{bc}\sin\phi \end{cases} \tag{81}$$

The previous equations allow us to express γ_{ab} and γ_{bc} as a function of γ_{ac} and the two contact angles (we use γ_{ac} as our independent variable to keep a similar formalism as in the mould wall case). After some algebra the expressions we get are:

$$\begin{cases} \gamma_{bc} = \frac{\sin\theta}{\sin\phi}\gamma_{ac} \\ \gamma_{ab} = \frac{\sin(\theta+\phi)}{\sin\phi}\gamma_{ac} \end{cases} \tag{82}$$

If we name r_1 and r_2 the two radii of the circular caps, we can relate all areas and lengths with r_1, r_2, θ and ϕ. In particular, there is a relation between the values of r_1 and r_2, which is derived by imposing that both circular caps match exactly at the interface (l_{ab} has the same value if computed via the upper circular cap or the lower one). This relation is the following:

$$\frac{r_1}{r_2} = \frac{\sin\phi}{\sin\theta} \tag{83}$$

Hence, we can write all the expressions as a function of just one of the radii (for example r_1) and the two contact angles. The expressions for these magnitudes in that case are (naming A_I and A_{II} the areas of the upper and lower circular caps, respectively):

$$A_V = A_I + A_{II} = (\theta - \sin\theta\cos\theta)\, r_1^2 + \left(\phi\frac{\sin^2\theta}{\sin^2\phi} - \frac{\sin^2\theta}{\tan\phi}\right) r_1^2$$

$$l_{ac} = 2\theta r_1$$

$$l_{bc} = 2_2 = 2\phi\frac{\sin\theta}{\sin\phi}r_1$$

$$l_{ab} = 2\sin\theta r_1$$

With these relations we can rewrite Eq. 80 as:

$$\Delta G_{het} = -\left(\theta + \phi\frac{\sin^2\theta}{\sin^2\phi} - \frac{\sin\theta}{\sin\phi}\sin(\theta+\phi)\right) r_1^2\Delta G_V + 2\theta r_1\gamma_{ac} + 2\phi\frac{\sin\theta}{\sin\phi}r_1\gamma_{bc} - 2\sin\theta r\gamma_{ab}$$

From Eq. 82 we can rewrite this expression as:

$$\Delta G_{het} = -\left(\theta + \phi\frac{\sin^2\theta}{\sin^2\phi} - \frac{\sin\theta}{\sin\phi}\sin(\theta+\phi)\right) r_1^2\Delta G_V + 2\left(\theta + \phi\frac{\sin^2\theta}{\sin^2\phi} - \frac{\sin\theta}{\sin\phi}\sin(\theta+\phi)\right) r_1\gamma_{ac}$$

Finally, we can write this expression in the following way:

$$\Delta G_{het} = (-\pi r_1^2 \Delta G_V + 2\pi r_1 \gamma_{ac}) S_2(\theta, \phi) \tag{84}$$

where:

$$S_2(\theta, \phi) = \left(\theta + \phi \frac{\sin^2 \theta}{\sin^2 \phi} - \frac{\sin \theta}{\sin \phi} \sin(\theta + \phi) \right) / \pi \tag{85}$$

Hence, the expression of the shape factor for nucleation at an interface in two dimensions is given by $S_2(\theta, \phi)$. Observe that, in this case, it depends on two contact angles instead of one.

Consider now nucleation in the three dimensional case. First of all we consider nucleation at a mould wall. It can be checked that the forming nucleus will have the shape of a spherical cap. We call θ the contact angle between the wall and the spherical cap (we can use Fig. 38 again, where now we think of the droplet as being spherical), and r the radius of the sphere. In that case, the variation in free energy after the formation of this nucleus is:

$$\Delta G_{het} = -V_S \Delta G_V + A_{SL} \gamma_{SL} + A_{SM} \gamma_{SM} - A_{SM} \gamma_{ML} \tag{86}$$

Similarly to the two dimensional case, the interface energies satisfy a balance equation at triple junctions in the x direction, which is:

$$\gamma_{SM} + \gamma_{SL} cos(\theta) = \gamma_{ML} \tag{87}$$

We can express all volumes and areas in Eq. 86 in terms of r and θ in the following way:

$$V_S = \frac{2\pi}{3}(1 - \cos\theta) r^3 - \frac{\pi}{3} \sin^2\theta \cos\theta r^3$$

$$A_{SL} = 2\pi(1 - \cos\theta) r^2$$

$$A_{SM} = \pi \sin^2\theta r^2$$

For computing the volume of the spherical cap first of all we integrated a surface differential for a constant value of the radius equal to r, and where the azimutal angle varies from $\pi/2$ to $\pi/2 - \theta$. Then we subtracted the volume of the cone formed by the surface A_{SM} and the center of the sphere.

If we put these expressions together in Eq. 86 we get:

$$\Delta G_{het} = -(\frac{2\pi}{3}(1 - \cos\theta) - \frac{\pi}{3} \sin^2\theta \cos\theta) r^3 \Delta G_V + 2\pi(1 - \cos\theta) r^2 \gamma_{SL} + \pi \sin^2\theta r^2 \gamma_{SM} - \pi \sin^2\theta r^2 \gamma_{ML}$$

$$\Delta G_{het} = -\frac{\pi}{3}((2 + \cos\theta)(1 - \cos\theta)^2) r^3 \Delta G_V + 2\pi(1 - \cos\theta) r^2 \gamma_{SL} + \pi \sin^2\theta r^2 (\gamma_{SM} - \gamma_{ML})$$

If we use the interface energy balance (Eq. 87) we can express all interface energies in term of γ_{SL}, and we finally get:

$$\Delta G_{het} = -\frac{\pi}{3}((2 + \cos\theta)(1 - \cos\theta)^2) r^3 \Delta G_V + \pi r^2 \gamma_{SL} (2(1 - \cos\theta) - \sin^2\theta \cos\theta)$$

$$\Delta G_{het} = -\frac{\pi}{3}((2+\cos\theta)(1-\cos\theta)^2)r^3\Delta G_V + \pi r^2\gamma_{SL}((2+\cos\theta)(1-\cos\theta)^2)$$

Hence, we obtain the expression for the shape factor, $S_1(\theta)$, for heterogeneous nucleation on a mould wall in three dimensions:

$$\Delta G_{het} = \left(-\frac{4\pi}{3}r^3\Delta G_V + 4\pi r^2\gamma_{SL}\right) S_1(\theta)$$

$$S_1(\theta) = \frac{(2+\cos\theta)(1-\cos\theta)^2}{4} \tag{88}$$

The same procedure can be made for heterogeneous nucleation at an interface, where three phases are present. We consider we have a nucleus of phase c forming at the interface between phases a and b. In this case, we have two spherical caps matched at the interface, with radii r_1 and r_2, and contact angles θ and ϕ (again, we can use Fig. 39 thinking that the droplet is three dimensional, and it consists of two spherical caps forming at a planar interface). These four quantities cannot take arbitrary values, since the matching of the two spherical caps at the interface poses a restriction in the values these quantities can take. As in the two dimensional case, this restriction has the expression:

$$\frac{r_1}{r_2} = \frac{\sin\phi}{\sin\theta} \tag{89}$$

Hence, we can write all expressions in term of only one radius, for instance r_1. Similarly to the mould wall case, the free energy increase has the following expression:

$$\Delta G_{het} = -V_S\Delta G_V + A_{ac}\gamma_{ac} + A_{bc}\gamma_{bc} - A_{ab}\gamma_{ab} \tag{90}$$

The interface energies satisfy the same balance equations at triple junctions as in the two dimensional case:

$$\begin{cases} \gamma_{ab} = \gamma_{ac}\cos\theta + \gamma_{bc}\cos\phi \\ \gamma_{ac}\sin\theta = \gamma_{bc}\sin\phi \end{cases} \tag{91}$$

This allows us to determine all interface energies in terms of one of them, for example γ_{ab}. Then:

$$\begin{cases} \gamma_{bc} = \frac{\sin\theta}{\sin\phi}\gamma_{ac} \\ \gamma_{ab} = \frac{\sin(\theta+\phi)}{\sin\phi}\gamma_{ac} \end{cases} \tag{92}$$

As for the volumes and areas in Eq. 90, we can compute them in the exact same way as in the mould wall case, taking into consideration that $r_2 = r_1\frac{\sin\theta}{\sin\phi}$:

$$V_S = V_{S,I} + V_{S,II} = \left(\frac{2\pi}{3}(1-\cos\theta)r_1^3 - \frac{\pi}{3}\sin^2\theta\cos\theta r_1^3\right) + \left(\frac{2\pi}{3}(1-\cos\phi)r_1^3 - \frac{\pi}{3}\sin^2\phi\cos\phi r_1^3\right)\frac{\sin^3\theta}{\sin^3\phi}$$

$$A_{ab} = \pi\sin^2\theta r_1^2$$

$$A_{ac} = 2\pi(1-\cos\theta)r_1^2$$

$$A_{bc} = 2\pi(1-\cos\phi)r_1^2\frac{\sin^2\theta}{\sin^2\phi}$$

The volume of the droplet has two contributions, $V_{S,I} + V_{S,II}$, which are the two semispherical caps, the upper one and the lower one, respectively. The total free energy increase is hence computed as:

$$\Delta G_{het} = -\left(\frac{2\pi}{3}(1-\cos\theta)r_1^3 - \frac{\pi}{3}\sin^2\theta\cos\theta r_1^3 + \left(\frac{2\pi}{3}(1-\cos\phi)\frac{\sin^3\theta}{\sin^3\phi}r_1^3 - \frac{\pi}{3}\frac{\cos\phi}{\sin\phi}\sin^3\theta r_1^3\right)\right)\Delta G_V$$
$$+2\pi(1-\cos\theta)r_1^2\gamma_{ac} + 2\pi(1-\cos\phi)r_1^2\frac{\sin^2\theta}{\sin^2\phi}\gamma_{bc} - \pi\sin^2\theta r_1^2\gamma_{ab}$$

With the same procedure as in the mould wall case we can write this expression only in terms of one interface energy, γ_{ab}, and, after grouping terms, in the end we get the final expression for the shape factor, $S_2(\theta,\phi)$:

$$\Delta G_{het} = \left(-\frac{4\pi}{3}r_1^3\Delta G_V + 4\pi r_1^2\gamma_{ab}\right)S_2(\theta,\phi)$$

$$S_2(\theta,\phi) = \frac{(2+\cos\theta)(1-\cos\theta)^2}{4} + \frac{(2+\cos\phi)(1-\cos\phi)\sin^3\theta}{4(1+\cos\phi)\sin\phi} \tag{93}$$

B. Analytical solution to the Cahn-Hilliard equation

The Cahn-Hilliard equation is PDE which has been widely studied from a mathematical point of view, since it is a very important equation in physics. Its study is interesting by itself from a mathematical point of view, and many results have been found regarding the existence and regularity of its solutions [42]. As most PDEs, it has no analytical solution in the general case. However, in the one dimensional case for binary mixtures, there is an analytical solution in some cases. In particular, the solution of the equation when Neumann boundary conditions are considered at both ends has an analytical expression [43]. However, the derivation of this solution is quite complex, and out of the scope of this thesis. However, we can compute the solution of the Cahn-Hilliard equation in an infinite domain, which is much easier, and use it as an approximation of the solution in the finite domain. The validity of this approximation depends on the value of some parameters.

When considered the spatial coordinate to range from $-\infty$ to $+\infty$, the boundary conditions we must impose are:

$$\lim_{x\to-\infty}\phi(x)=-1 \qquad \lim_{x\to+\infty}\phi(x)=1 \qquad \lim_{x\to\pm\infty}\frac{\partial\phi}{\partial x}=0$$

To obtain the analytical solution, we have to go back to the Beltrami identity (Eq. 31), which states:

$$\frac{A}{4}(1-\phi^2)^2-\frac{\lambda^2 A}{2}\left|\frac{\partial\phi}{\partial x}\right|^2=0 \tag{94}$$

This is actually an ODE (ϕ only depends on the spatial coordinate, we are considering stationary solutions) which can be solved analytically. Since we already expect the solution to increase from -1 to 1, the derivative will always be positive, so the absolute value can be omitted. Also, since $\phi\in(-1,1)$, $\phi^2<1$ and therefore $\sqrt{(1-\phi^2)^2}=1-\phi^2$. If we name $\alpha=\frac{\sqrt{2}}{\lambda}$, the ODE is:

$$\frac{d\phi}{dx}=\frac{\alpha}{2}(1-\phi^2)$$

$$\frac{d\phi}{1-\phi^2}=\frac{\alpha}{2}dx$$

$$\int\frac{d\phi}{1-\phi^2}=-\frac{1}{2}\int\frac{d\phi}{1-\phi}+\frac{1}{2}\int\frac{d\phi}{1+\phi}=-\frac{1}{2}\ln|\phi-1|+\frac{1}{2}\ln|\phi+1|=\frac{\alpha}{2}x+K$$

$$\ln\frac{1+\phi}{1-\phi}=\alpha x+C$$

$$\frac{1+\phi}{1-\phi}=e^{2(\frac{\alpha}{2}x+C)}=Me^{\alpha x}$$

$$\phi(x)=\frac{Me^{\alpha x}-1}{Me^{\alpha x}+1}$$

Using Beltrami's identity, the derivative of the order parameter is:

$$\frac{d\phi}{dx} = \alpha\left(1 - \left(\frac{Me^{\alpha x} - 1}{Me^{\alpha x} + 1}\right)^2\right) = \alpha\frac{(1 + Me^{\alpha x})^2 - (1 - Me^{\alpha x})^2}{(Me^{\alpha x} + 1)^2}$$

$$\frac{d\phi}{dx}(x) = \frac{2\alpha Me^{\alpha x}}{1 + 2Me^{\alpha x} + M^2e^{2\alpha x}}$$

Observe that we get a family of solutions which satisfy the differential equation. What's more, all of them satisfy all the boundary conditions. They only differ in the value of M, which has an effect of shifting the solution to the right or to the left. That means that the value of M allows us to determine at which point we want the transition to take place (see Fig. 40). Hence, we can impose an additional condition to determine the value of M.

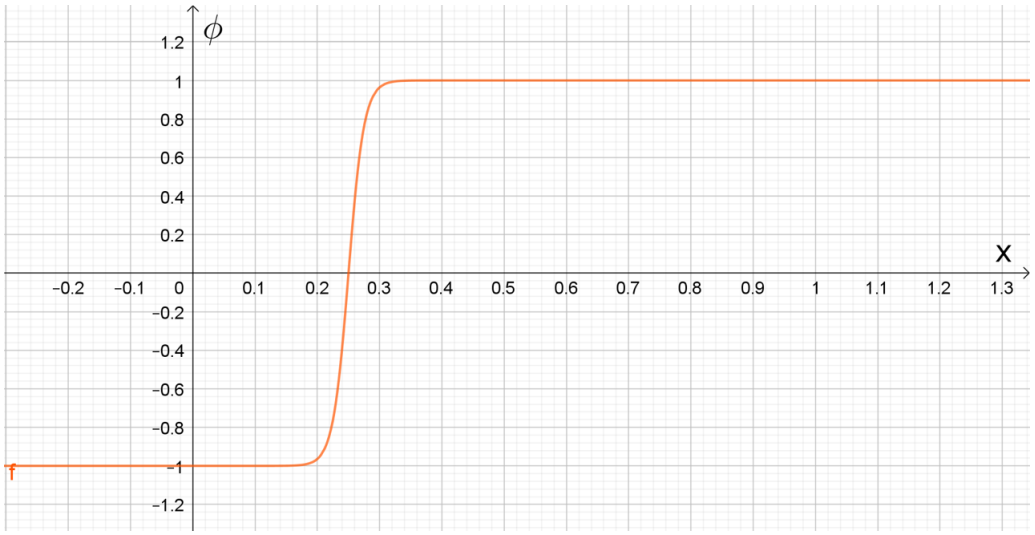

Figure 40: Theoretical solution to the Cahn-Hilliard equation on an infinite domain for $\delta = 0.03$ and $\bar{\phi} = 0.7$.

A remark must be made at this point. We solved the original equation on an infinite domain, imposing conditions on the function at infinity. Since the differential equation does not have any term in x, given a solution of the equation, $\phi(x)$, $\phi(x + x_0)$ is also a solution for any $x_0 \in \mathbb{R}$. That's why we get a family of solutions which depend on a parameter, and it can be checked that changing the value of M is equivalent to a translation along the x axis.

With this said, we are actually not interested in the solution on all $\mathbb{R}$, but only in a finite domain (in our case it's $(0, 1)$). Hence, the solution we found is not the one we were looking for. However, for the values of δ we use in simulations (bellow 0.05) the solution in the infinite domain satisfies that the value of the function at both ends of the interval is approximately constant and equal to -1 at $x = 0$ and 1 at $x = 1$. In fact, errors are exponentially small when the interface width is much smaller than the domain length and the interface is far away from the boundaries. Hence, it is a good approximation of the solution of the Cahn-Hilliard solution with Neumann boundary conditions.

One of the parameters we fix in simulation is the mean concentration of the component, which is defined as the integral of ϕ in $x \in (0, 1)$. Hence, if the mean concentration of ϕ is $\bar{\phi}$, the condition to determine where the transition takes place, which is equivalent to determining M, is:

$$\int_0^1 \phi(x)dx = \left[\frac{2\ln\left(Me^{\alpha x}+1\right)}{\alpha} - x\right]_0^1 = \frac{2\ln\left(Me^{\alpha}+1\right)}{\alpha} - 1 - \frac{2\ln\left(M+1\right)}{\alpha} = \bar{\phi}$$

$$\frac{1+\bar{\phi}}{2}\alpha = \ln\left(\frac{Me^{\alpha}+1}{M+1}\right)$$

$$M = \frac{e^{\frac{1+\bar{\phi}}{2}\alpha} - 1}{e^{\alpha} - e^{\frac{1+\bar{\phi}}{2}\alpha}}$$

In that way we get the expression of the analytical solution to the Cahn-Hilliard equation in one dimension in an infinite region, which can be used to compare the validity of the results we get.

References

[1] A. Molliex, J. Temirov, J. Lee, M. Coughlin, A. P. Kanagaraj, H. J. Kim, T. Mittag, J. P. Taylor, Phase separation by low complexity domains promotes stress granule assembly and drives pathological fibrillization, Cell 163 (1) (2015) 123–133.

[2] A. A. Hyman, C. A. Weber, F. Jülicher, Liquid-liquid phase separation in biology, Annual review of cell and developmental biology 30 (2014) 39–58.

[3] J. Berry, C. P. Brangwynne, M. Haataja, Physical principles of intracellular organization via active and passive phase transitions, Reports on Progress in Physics 81 (4) (2018) 046601.

[4] D. Bracha, M. T. Walls, C. P. Brangwynne, Probing and engineering liquid-phase organelles, Nature biotechnology 37 (12) (2019) 1435–1445.

[5] J.-M. Choi, A. S. Holehouse, R. V. Pappu, Physical principles underlying the complex biology of intracellular phase transitions, Annual Review of Biophysics 49 (2020) 107–133.

[6] J. W. Gibbs, Scientific Papers: Thermodynamics, Vol. 1, Dover Publications, 1961.

[7] S. Mao, D. Kuldinow, M. P. Haataja, A. Košmrlj, Phase behavior and morphology of multicomponent liquid mixtures, Soft Matter 15 (6) (2019) 1297–1311.

[8] S. Mao, M. S. Chakraverti-Wuerthwein, H. Gaudio, A. Košmrlj, Designing the morphology of separated phases in multicomponent liquid mixtures, Physical Review Letters 125 (21) (2020) 218003.

[9] L. Ratke, P. W. Voorhees, Growth and coarsening: Ostwald ripening in material processing, Springer Science & Business Media, 2013.

[10] R. S. Davis, Multi-phase field models and microstructural evolution with applications in fuel cell technology, Ph. D. Thesis (2018).

[11] L. Zhang, W. Ren, A. Samanta, Q. Du, Recent developments in computational modelling of nucleation in phase transformations, NPJ Computational Materials 2 (1) (2016) 1–9.

[12] R. Backofen, A. Voigt, A phase field crystal study of heterogeneous nucleation–application of the string method, The European Physical Journal Special Topics 223 (3) (2014) 497–509.

[13] T. Li, P. Zhang, W. Zhang, Numerical study for the nucleation of one-dimensional stochastic cahn-hilliard dynamics, Communications in Mathematical Sciences 10 (4) (2012) 1105–1132.

[14] T. Philippe, D. Blavette, Minimum free-energy pathway of nucleation, The Journal of chemical physics 135 (13) (2011) 134508.

[15] W. Wu, D. Montiel, J. Guyer, P. Voorhees, J. Warren, D. Wheeler, L. Gránásy, T. Pusztai, O. Heinonen, Phase field benchmark problems for nucleation, Computational Materials Science 193 (2021) 110371.

[16] T. Li, P. Zhang, W. Zhang, Nucleation rate calculation for the phase transition of diblock copolymers under stochastic cahn–hilliard dynamics, Multiscale Modeling & Simulation 11 (1) (2013) 385–409.

[17] T. Philippe, Nucleation and interfacial adsorption in ternary systems, The Journal of chemical physics 142 (9) (2015) 094501.

[18] N. Moelans, B. Blanpain, P. Wollants, Quantitative analysis of grain boundary properties in a generalized phase field model for grain growth in anisotropic systems, Physical Review B 78 (2) (2008) 024113.

[19] S. O. Poulsen, P. Voorhees, E. M. Lauridsen, Three-dimensional simulations of microstructural evolution in polycrystalline dual-phase materials with constant volume fractions, Acta materialia 61 (4) (2013) 1220–1228.

[20] J. R. Wilson, W. Kobsiriphat, R. Mendoza, H.-Y. Chen, J. M. Hiller, D. J. Miller, K. Thornton, P. W. Voorhees, S. B. Adler, S. A. Barnett, Three-dimensional reconstruction of a solid-oxide fuel-cell anode, Nature materials 5 (7) (2006) 541–544.

[21] G. Henkelman, H. Jónsson, A dimer method for finding saddle points on high dimensional potential surfaces using only first derivatives, The Journal of chemical physics 111 (15) (1999) 7010–7022.

[22] R. Olsen, G. Kroes, G. Henkelman, A. Arnaldsson, H. Jónsson, Comparison of methods for finding saddle points without knowledge of the final states, The Journal of chemical physics 121 (20) (2004) 9776–9792.

[23] G. Crippen, H. Scheraga, Minimization of polypeptide energy: Xi. the method of gentlest ascent, Archives of biochemistry and biophysics 144 (2) (1971) 462–466.

[24] W. Gao, J. Leng, X. Zhou, An iterative minimization formulation for saddle point search, SIAM Journal on Numerical Analysis 53 (4) (2015) 1786–1805.

[25] G. Henkelman, H. Jónsson, Improved tangent estimate in the nudged elastic band method for finding minimum energy paths and saddle points, The Journal of chemical physics 113 (22) (2000) 9978–9985.

[26] G. Henkelman, B. P. Uberuaga, H. Jónsson, A climbing image nudged elastic band method for finding saddle points and minimum energy paths, The Journal of chemical physics 113 (22) (2000) 9901–9904.

[27] E. Weinan, W. Ren, E. Vanden-Eijnden, String method for the study of rare events, Physical Review B 66 (5) (2002) 052301.

[28] E. Weinan, W. Ren, E. Vanden-Eijnden, et al., Finite temperature string method for the study of rare events, J. Phys. Chem. B 109 (14) (2005) 6688–6693.

[29] E. Weinan, W. Ren, E. Vanden-Eijnden, Simplified and improved string method for computing the minimum energy paths in barrier-crossing events, Journal of Chemical Physics 126 (16) (2007) 164103.

[30] S. Bonfanti, W. Kob, Methods to locate saddle points in complex landscapes, The Journal of chemical physics 147 (20) (2017) 204104.

[31] D. A. Porter, K. E. Easterling, Phase transformations in metals and alloys (revised reprint), CRC press, 2009.

[32] Rubinšteĭ, The stefan problem.

[33] G. Tryggvason, R. Scardovelli, S. Zaleski, Direct numerical simulations of gas–liquid multiphase flows, Cambridge University Press, 2011.

[34] G. Tryggvason, B. Bunner, O. Ebrat, W. Tauber, Computations of multiphase flows by a finite difference/front tracking method. i. multi-fluid flows, Lecture Series-von Karman Institute For Fluid Dynamics (1998) 7–7.

[35] N. Provatas, K. Elder, Phase-field methods in materials science and engineering, John Wiley & Sons, 2011.

[36] R. Courant, D. Hilbert, Methods of Mathematical Physics: Partial Differential Equations, John Wiley & Sons, 2008.

[37] D. A. Cogswell, A phase-field study of ternary multiphase microstructures, Ph.D. thesis, Massachusetts Institute of Technology (2010).

[38] G. Job, F. Herrmann, Chemical potential—a quantity in search of recognition, European journal of physics 27 (2) (2006) 353.

[39] J. B. W. Webber, Studies of nano-structured liquids in confined geometry and at surfaces., Progress in Nuclear Magnetic Resonance Spectroscopy 56 (1) (2010) 78–93.

[40] H.-J. Butt, K. Graf, M. Kappl, Physics and chemistry of interfaces, John Wiley & Sons, 2013.

[41] D. Wang, X.-P. Wang, Y.-G. Wang, The dynamics of three-phase triple junction and contact points, SIAM Journal on Applied Mathematics 77 (5) (2017) 1805–1826.

[42] J. Wei, M. Winter, Stationary solutions for the cahn-hilliard equation, in: Annales de l'Institut Henri Poincare (C) Non Linear Analysis, Vol. 15, Elsevier, 1998, pp. 459–492.

[43] M. Grinfeld, A. Novick-Cohen, Counting stationary solutions of the cahn–hilliard equation by transversality arguments, Proceedings of the Royal Society of Edinburgh Section A: Mathematics 125 (2) (1995) 351–370.